Topotactic Phase Transformations
in Manganite Thin Films and Cobaltite Bilayers

By

RYAN ANTHONY FILLHOUER
THESIS

Submitted in partial satisfaction of the requirements for the degree of

MASTER OF SCIENCE
in
MATERIALS SCIENCE AND ENGINEERING
in the
OFFICE OF GRADUATE STUDIES
of the
UNIVERSITY OF CALIFORNIA
DAVIS

Approved:

Yayoi Takamura, Chair

Roopali Kukreja

Seung Sae Hong

Committee in Charge

2023

Abstract

Global computational power demands are sharply increasing and existing computing architectures are reaching the limits imposed by fundamental physics. Neuromorphic computing is a philosophy of computer design based on the human brain, which is much more energy-efficient than manufactured computers. However, current materials are not optimized for emerging neuromorphic devices that require the ability to manipulate multiple electronic or magnetic states. Complex oxide materials exhibit a rich variety of interesting phenomena such as high temperature superconductivity, metal-to-insulator phase transitions, and colossal magnetoresistance. Perovskites are one of the members of the complex oxide family that have been studied for nearly a century and have shown promise in solving materials science problems in applications including data storage and computing, photovoltaic cells, solid oxide fuel cells, and light emitting diodes. Modern fabrication techniques enable synthesis of a wide variety of nanomaterials such as thin films, heterostructures namely bilayers or multilayers, and nanostructures such as quantum dots. Furthermore, there are many elements that can stably form the perovskite structure. Nanostructuring and the presence of interfaces in these systems allows for the functional properties to be tailored for a specific need and sometimes give rise to emergent phenomena, thus opening the door to many possible avenues of research.

Past studies have shown that perovskite oxide thin films readily undergo topotactic phase transformations where either anion or cation vacancies form and rearrange into an ordered sublattice forming a new structure with distinct properties. Moreover, alternating the stacking order of heterostructures is a technique that has been proven to elicit differing outcomes in systems containing the same constituent layers. This thesis explores annealing-induced topotactic phase transformations of perovskite thin films and bilayers which cause structural and magnetic changes in the materials. There is limited research on the topotactic phase transformations in $La_{0.7}Sr_{0.3}MnO_3$ thin films, and to date, no study has looked specifically at the effect of stacking order of $LaCoO_3$-$La_{0.7}Sr_{0.3}CoO_3$ bilayers regarding the phases produced by topotaxy. In this thesis, manganite thin films and cobaltite bilayers with alternating stacking order were synthesized and annealed under different conditions. The annealing process initiated topotactic phase transformations which were studied using X-ray diffraction, X-ray photoelectron spectroscopy and soft X-ray magnetic spectroscopy. Beginning from the perovskite phase, manganite thin films and cobaltite bilayers underwent structural and magnetic changes into perovskite-related phases including oxygen-deficient perovskite, Grenier, brownmillerite, and Ruddlesden-Popper phases. In the bilayer systems, the stacking order of the constituent layers influenced which phases were formed under different annealing conditions. The bilayers also behaved differently from their corresponding single layer thin films that were annealed under the same conditions, giving rise to phases that were not present in the single layer configurations. Along with the structural phase transformation, the magnetic properties of the material were also modified. Control of magnetic properties is important for application in spintronics—a growing field of study that makes use of the modulation and detection of spin states in a material for data storage and processing. Furthermore, access and control of numerous unique phases in the same material can pave the path for the next-generation computing devices.

Contents

List of Figures

List of Tables

Chapter 1

Introduction

1.1 Motivation and Background

Modern computing has defined the last 50 years of civilization and has given rise to some of the world's most remarkable innovations, such as the transistor, the integrated circuit, and the internet. However these accomplishments come not without their costs. Energy demand for computing tasks has been sharply rising for the past several decades [1] and is projected to increase tenfold by 2030 [2]. With the advent of modern computer-dependent technologies such as artificial intelligence (AI), machine learning (ML), and the internet of things (IoT), a need arises for computers to be able to solve tasks of increasing complexity, and the ability to do so faster and more efficiently. Current architectures are becoming limited by the so-called "von-Neumann Bottleneck", which manifests as high latency times and high energy consumption in computational tasks [3]. Bio-inspired neuromorphic computing architectures are a somewhat nascent solution to this problem but have been gaining attention over recent years [4]. Inside the mammalian brain is a complex network of tens of billions of neurons,

each branching off to many other neurons and creating more than 10^{15} synaptic junctions [5]. This density of neural connections gives the brain the potential for complex problem-solving while consuming a mere 20 Watts of power. Researchers are searching for materials that could be used in devices that could mimic neural architecture [5]. Functional materials can be tailored to be able to quickly transition from one or more states to another and this property can be used to advance neuromorphic computing-based architecture [6, 7].

Complex oxides are a family of ceramic compounds with oxygen anions bound to two or more different cations. These materials can exist as crystal structures which consist of repeating arrangements of unit cells of atoms. As discussed later in Section 1.2, the structure, symmetry, elements present, and external stimuli all influence the functionalities observed in the material.

1.1.1 Topotaxy

Some crystal structures are able to rearrange in a way that the new phase retains a crystallographic orientation relationship with its parent phase and this type of reaction is termed a "topotactic phase transformation" or "topotaxy" coined in 1959 by Lotgering [8]. Topotactic phase transformations can be initiated by isotropic influence such as thermal annealing in a controlled oxygen pressure atmosphere [6] or by hydrogenation [9], as well as by the application of directional fields such as electrical and strain fields, and these transformations are often reversible [10]. Additionally, it has been observed that juxtaposing specific materials of different composition can also induce a topotactic phase transformation [11–14]. This process occurs by the spontaneous redox reaction of the capping "getter" layer of a material such as gadolinium which can leech oxygen from the material it is deposited on. Oxygen anions are transferred from the material to the getter layer and in some cases, the oxygen vacancies can order into an oxygen vacancy sublattice and a new structural phase is formed

[15]. In topotactic phase transformations, the product phase is structurally similar to the parent phase, but there are measurable changes in the crystal structure such as the d-spacing or lattice parameters. There are also observable changes to the material's functional properties such as its magnetic response and electrical conductivity. Candidate oxide materials that undergo topotaxy have low oxygen vacancy formation energy and high oxygen vacancy diffusivity, which are properties that are observed in manganites [16], cobaltites [17], and ferrites [10], suggesting that these materials could be used not only to develop neuromorphic devices, but also to more deeply study the kinetics of topotactic phase transformations. Topotaxy is one route of synthesizing materials that may otherwise be difficult or impossible by other existing methods and this concept is the foundation for this thesis.

1.2 Perovskite & Perovskite-Related Oxide Structures

1.2.1 Perovskite Phase, ABO_3

Perovskite oxide is one of the most extensively studied crystal structures, often represented by its formula, ABO_3. Earth's most common naturally occurring solid phase is a mineral having the perovskite structure called bridgemanite which consists of magnesium and iron silicate [18]. Many elements can be naturally formed or artificially synthesized into the perovskite phase because of its relatively simple structure. Figure 1.1 shows the ideal, generalized ABX_3 perovskite unit cell with A-site ions at the corners of the cube, B-site ion in octahedral coordination at the body-center of the cube, and six X-site ions at each face-center of the cube (this location is also the corner of the BX_6 octahedron), which are oxygen anions in perovskite oxides. The periodic table in Figure 1.1 shows the elements that are compatible in the respective A-, B-, or X-sites of the perovskite structure with the limiting factor being a ratio of the ionic radii of its constituents.

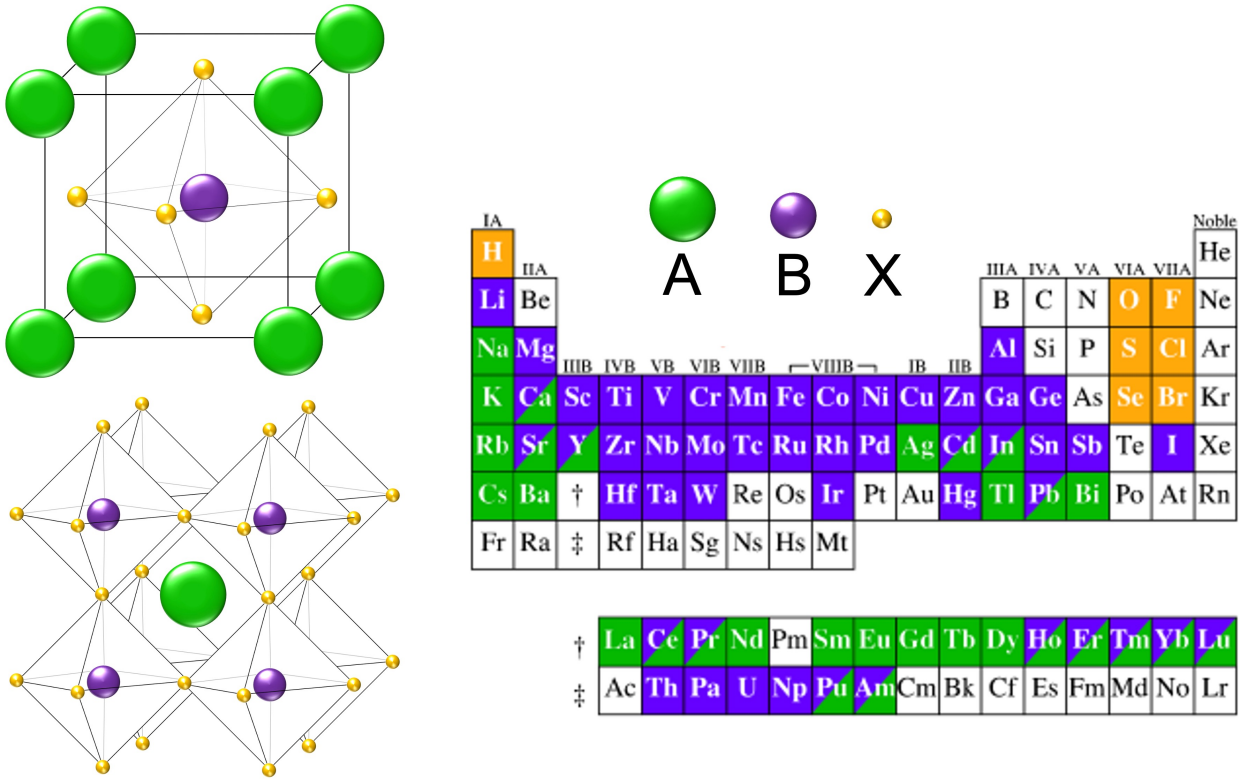

Figure 1.1: Two depictions of the ABX_3 perovskite unit cell and periodic table showing the possible perovskite compositions (adapted from [19]).

A powerful tool in predicting stable perovskite structures is the Goldschmidt tolerance factor [20]. By taking ratios of the radii of the A, B, and X ions in the ABX_3 perovskite unit cell, a factor is calculated that can lend insight into the likelihood of the chosen ions to form perovskite structures, as well as the crystal symmetry of the resulting perovskite. The formula for the Goldschmidt tolerance factor is as follows.

$$t = \frac{R_A + R_X}{\sqrt{2}(R_B + R_X)} \tag{1.1}$$

where t is the Goldschmidt tolerance factor, R_A is the ionic radius of the A-site cation, R_B is the ionic radius of the B-site cation, and R_X is the ionic radius of the X-site anion.

For the remainder of this thesis, only oxides will be considered ($X = O$), however much of the discussion can extend to the generic ABX_3 perovskite. As ions of different radii are assembled into the ideal cubic perovskite oxide structure, the BO_6 octahedra tilt to accommodate their different sizes, while maintaining the B-O-B bonding scheme throughout the crystal. Furthermore, the octahedra undergo Jahn-Teller distortions where one or more axes of the octahedra stretch or compress as discussed further in Section 1.3.1, and both of these mechanisms can force the perovskite into symmetries other than cubic.

For tolerance values of t close to 1, the perovskite structure will take on an ideal cubic symmetry. If cations of smaller radii are substituted into the A-site, the BO_6 octahedra must tilt to fill the space which forces the structure into a crystal system with lower symmetry such as the tetragonal or orthorhombic systems and further into trigonal systems where the crystal takes on a non-perovskite structure. If t >1, from either a large A cation, a small B cation, or both, then the octahedra tilt to such an extent that perovskite form hexagonal symmetry structure where the BO_6 octahedra share faces rather than vertices [21]. These values and symmetries are listed in Table 1.1.

The Goldschmidt tolerance factor is not a strict condition for forming the perovskite crystal structure. However, it is a proven framework that can predict the crystal symmetry for the approximately 2,000 known stable perovskites and it is also proposed to hold true for the estimated 90,000 new perovskites that have not yet been studied [22, 23].

1.2.2 Oxygen Deficient Perovskite Phase, $ABO_{3-\delta}$

Under certain conditions, some of the oxygen anions are able to break the bonds holding them inside the perovskite structure. The stoichiometry for oxygen deficient perovskite (ODP) is denoted as $ABO_{3-\delta}$ where, δ is the average number of oxygen vacancies present per unit

Table 1.1: Goldschmidt tolerance factors for perovskites and corresponding expected crystal symmetries [21].

Goldschmidt Tolerance Factor	**Perovskite Symmetry**
t >1	hexagonal
0.9 <t <1	cubic
0.71 <t <0.9	orthorhombic, rhombohedral
t <0.71	non-perovskite phases, e.g. bixbyite, corundum

cell. When an oxygen vacancy forms, the BO_6 octahedron reduces its coordination and the average B-site cation valence decreases. These oxygen vacancies play a significant role in the functional properties of the material because of the strong correlation between the oxygen $2p$ electrons and the d-shell electrons of the transition metals which manifests as properties such as metal-insulator transitions [24], and magnetic phase transitions [25]. The capability of oxygen content modulation in perovskite oxides gives rise to materials that can be used in applications such as sensors, memristive devices for neuromorphic computing, and solid oxide fuel cells (SOFC) [26–29].

1.2.3 Grenier Phase, $ABO_{2.67}$

Oxygen vacancies in a crystalline material can order into layers and produce a new phase. In the perovskite family, there are a wide variety of perovskite oxides with ordered oxygen vacancies [29], but of the distinct phases considered in this thesis is the Grenier (GR) phase, with $ABO_{2.67}$ stoichiometry [30]. The GR phase arises when oxygen vacancies combine in rows where every third row of BO_6 octahedra (O) in the perovskite structure is replaced by BO_4 tetrahedra (T) to form the scheme (OOTOOT...) along the c-direction throughout the crystal structure. This phase transformation results in the unit cell of the crystal being

defined to encompass two tetrahedral layers thus causing a sixfold increase in the out-of-plane lattice parameter compared to that of the perovskite (P) ($c_{GR} = 6c_P$). A diagram of the unit cell and oxygen vacancy ordering is shown in Figure 1.2.

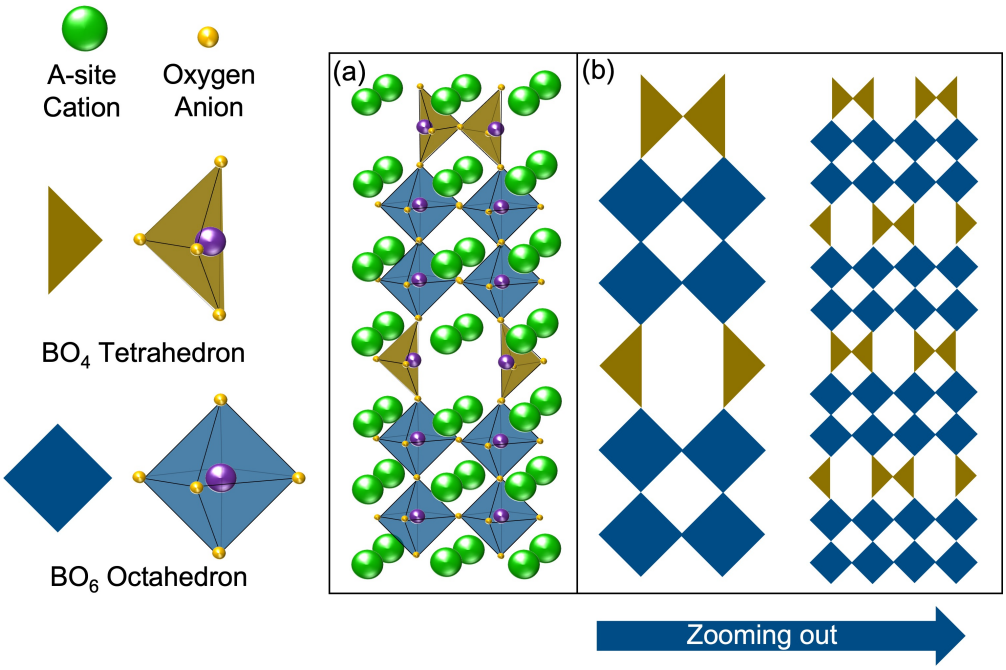

Figure 1.2: $ABO_{2.67}$ Grenier phase (a) unit cell, and (b) polyhedral representations of the repeating octahedral and tetrahedral layers. As the perovskite loses $\frac{1}{9}$ of its oxygen anions and the oxygen vacancies order, the structure can form alternating layers of two octahedral planes, followed by a tetrahedral plane and this repeats throughout the crystal, thus forming the Grenier phase.

1.2.4 Brownmillerite Phase, $ABO_{2.5}$

When the perovskite loses $\frac{1}{6}$ of its oxygen from the crystal structure and the oxygen vacancies order in a way where there are alternating layers of BO_6 octahedra, and BO_4 tetrahedra, the brownmillerite (BM) structure with $ABO_{2.5}$ is formed [31]. The layer pattern in BM structures is (OTOTOT...) [32]. This phase transformation results in a unit cell that repeats every four layers, which causes a fourfold increase in the out-of-plane lattice parameter

($c_{BM} = 4c_P$) and the BM structure with oxygen vacancy ordering is shown in Figure 1.3.

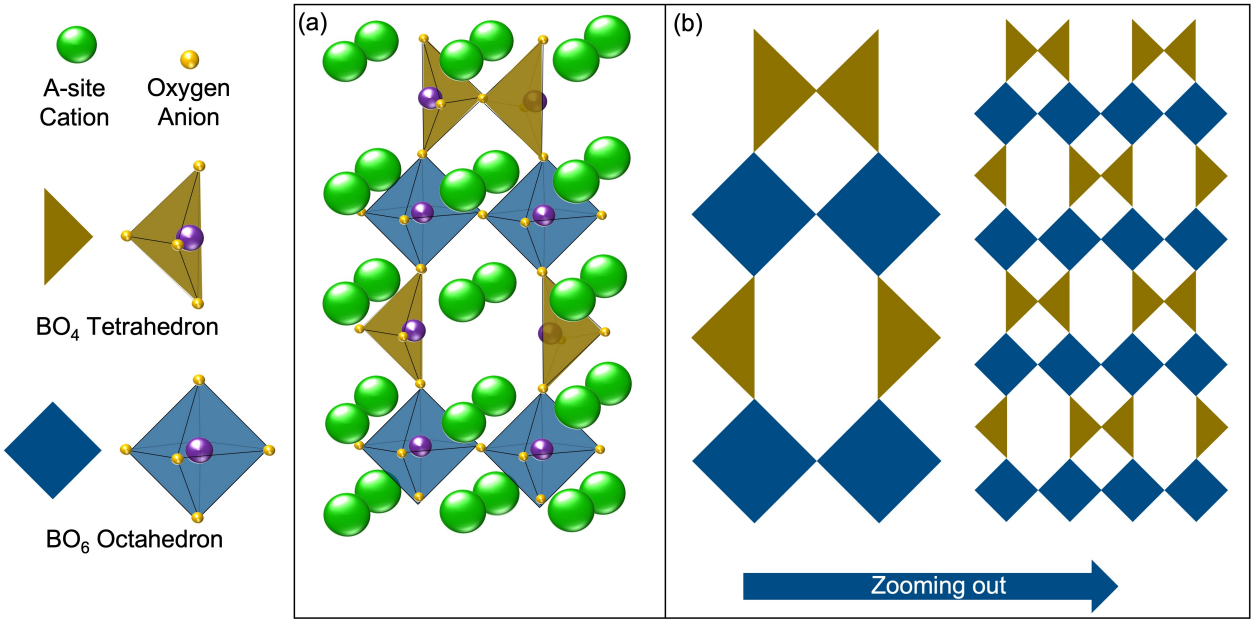

Figure 1.3: $ABO_{2.5}$ Brownmillerite phase (a) unit cell, and (b) polyhedral representations of the octahedral and tetrahedral ordering. As the perovskite loses more of its oxygen anions, the oxygen vacancies can order to make layers of alternating octahedral and tetrahedral layers that are characteristic of the BM phase.

1.2.5 Infinite Layer Phase, ABO_2

Recent oxide studies have turned towards a perovskite-related structure referred to as the "infinite layer" phase or "square planar" (SP) phase with stoichiometry ABO_2. The nomenclature comes from the square planar BO_4 coordination of the B-site cation in the structure as shown in Figure 1.2.5. Somewhat elusive, the SP structure has most commonly been synthesized as nickelates [33], cuprates [34], and ferrites [35]. The SP phase is of particular interest because this structure often exhibits high critical temperature (T_c) superconductivity in nickelates and cuprates. SP ferrites on the other hand, have not yet shown superconductivity, remaining insulating down to temperatures of 100mK, and the mechanism by which high-T_c superconductivity occurs in SP oxides is still under investigation [36, 37].

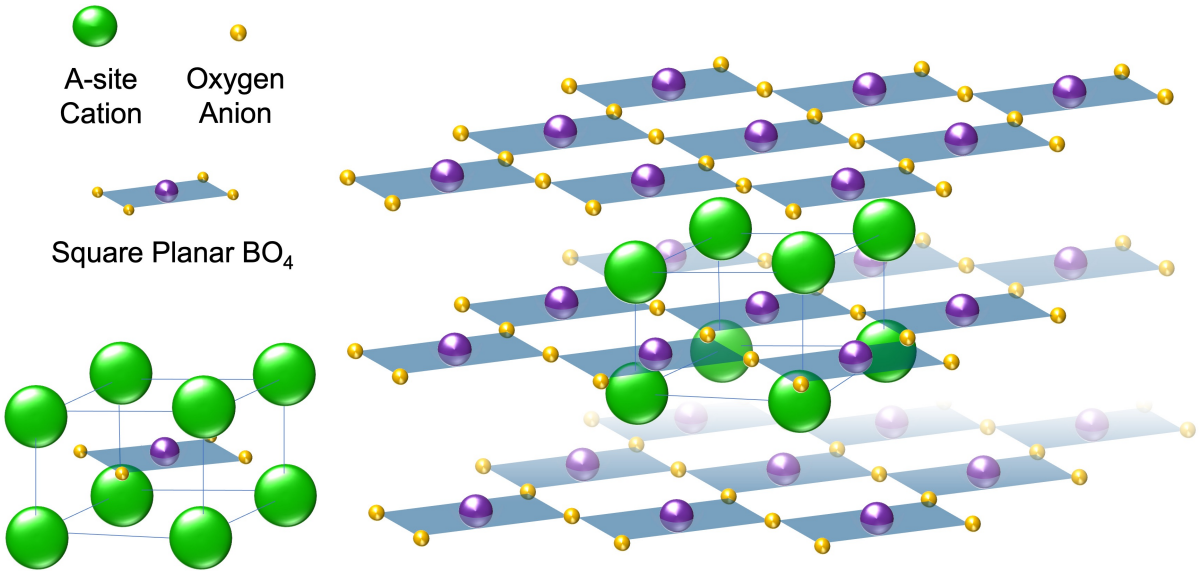

Figure 1.4: ABO_2 Infinite layer phase (SP). The square planar coordinated B-site cations form 2-dimensional sheets that layer in the c-direction.

1.2.6 Ruddlesden-Popper Phase, $A_{n+1}B_nO_{3n-1}$, n = (1, 2, 3, ...)

Further reduction of the perovskites can force the structure to develop not only a higher amount of oxygen vacancies, but cation vacancies as well. Topotactic reduction is one route of synthesizing the Ruddlesden-Popper (RP) phase with stoichiometry $A_{n+1}B_nO_{3n-1}$ or $(AO)(ABO_3)_n$, where n is an integer [38, 39]. The integer n is equal to the number of layers of perovskite unit cells separated by an AO rock salt-like layer as shown in Figure 1.5. For $n = 1$, the stoichiometry becomes A_2BO_4 or equivalently, $(AO)ABO_3$. It should also be noted that as the cation vacancy forms and the cation diffuses through the material, it has been shown to accumulate as nanoparticles within the material [6]. Studies performed on La_2CoO_4 showed that this material can absorb large amounts of oxygen and still remain stable, supporting its application for SOFC cathode materials [40]. Despite the growing list of superconducting systems with the RP phase including ruthenates and high entropy alloy (HEA) cuprates, numerous recent studies are still ongoing as to the exact mechanisms behind this phenomenon [41, 42]. A phase transformation from perovskite to A_2BO_4 RP phase

results in defining the unit cell as approximately three layers of perovskite, so a threefold increase in the out-of-plane lattice parameter ($c_{RP} = 3c_P$).

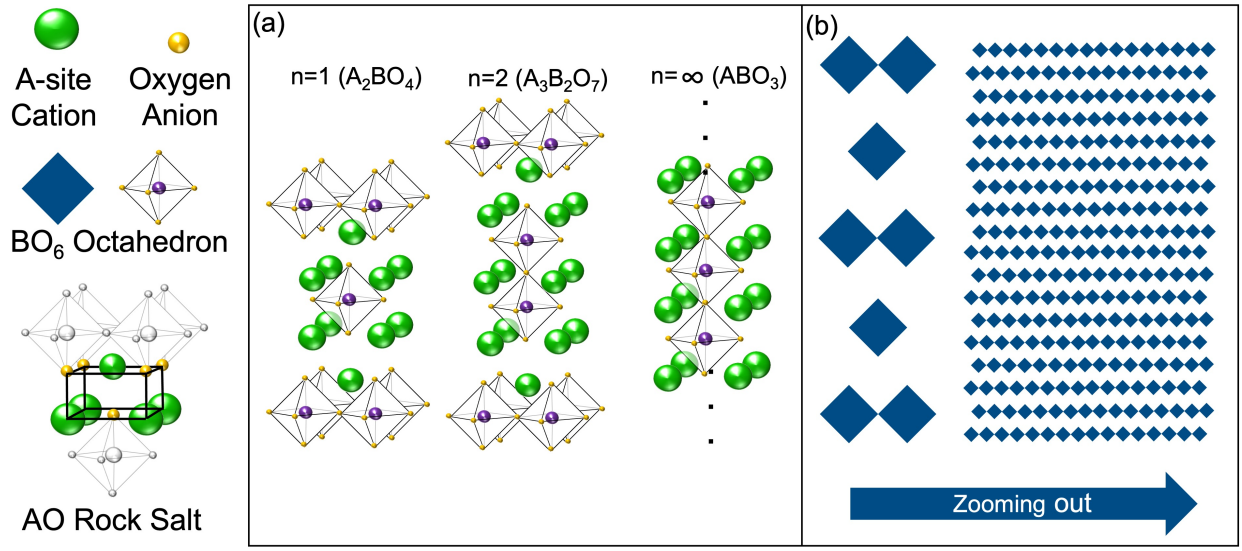

Figure 1.5: $A_{n+1}B_nO_{3n-1}$ Ruddlesden-Popper phase (a) unit cell and (b) polyhedral representation of the layers of octahedral planes of A_2BO_4 ($n = 1$). The RP phase is created when a certain amount of A cations and oxygen anions are removed from the perovskite crystal. The result is a layered structure with n layers of perovskite sandwiched between AO layers.

1.3 Thin Film Epitaxy

Perovskites can be synthesized in many different nanomaterial states such as nanostructures [43], quantum dots [44], free-standing membranes [45], and heterostructures [46]. Single crystal thin films are a way to study materials of high structural and chemical purity and they allow for multiple experimental variables to be tested such as film thickness, strain state, and heterostructure modification. There are several popular thin film synthesis routes that are discussed in Chapter 2. Film deposition-based techniques involve the accumulation of layers of a target material onto a crystalline substrate material so that a film "grows" epitaxially on top of a substrate surface. Epitaxy arises when the unit cells of a film material

stack onto a crystalline substrate and adopts the orientation of the substrate. Epitaxial thin films can be further classified as (a) matched, where the in-plane lattice parameters of the bulk material is equal to those of the substrate; (b) coherently strained to the substrate, where the in-plane lattice parameters of the film and substrate are equal; (c) fully relaxed, where the lattice parameters of the film are equal to their bulk value; or (d) semi-coherently strained in which the film is partially relaxed and its lattice parameters are in between the bulk value and the value of the substrate. This is shown schematically in Figure 1.6.

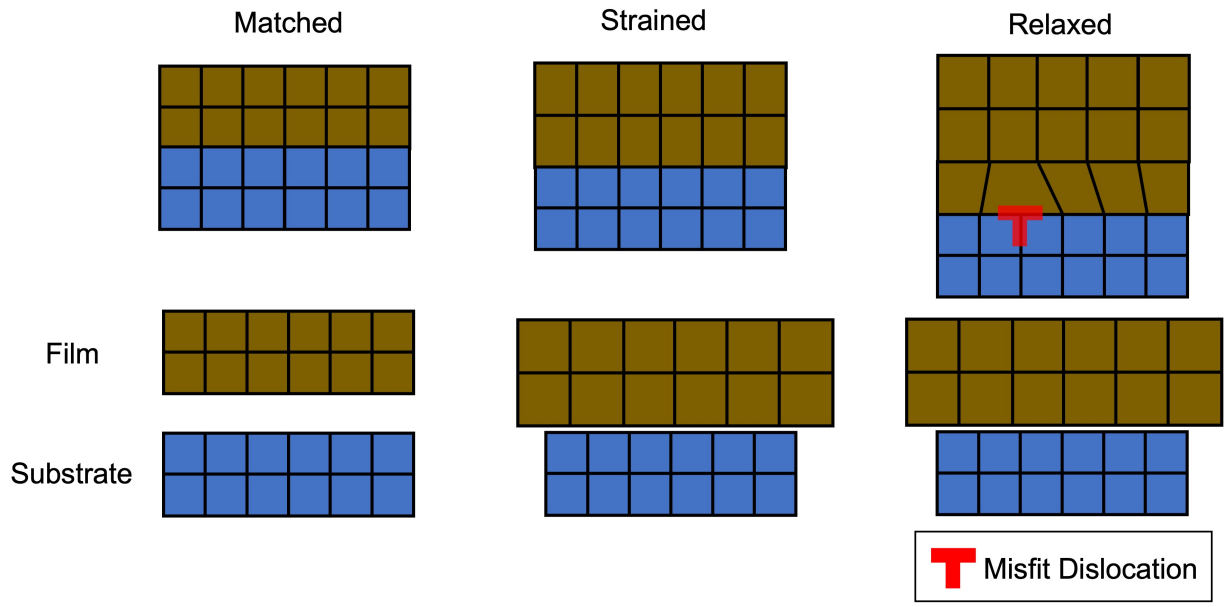

Figure 1.6: Various classifications of epitaxial films. In the matched film, the lattice parameter of the bulk material is equal to that of the substrate so the film does not need to strain to align with the substrate's lattice. As a result, the film is coherently strained to the substrate. In the strained film example, the in-plane lattice parameter of the bulk material is larger than that of the substrate, so the film must be strained under compression in the in-plane direction to become coherently strained to the substrate. In the final example, the film is relaxed from the substrate with the strain being accommodated by the misfit dislocation shown as a red "T" (adapted from [47]).

If the bulk lattice parameter of the film material differs from the lattice parameter of the

substrate, lattice mismatch exists and epitaxial strain is induced in the film. Lattice mismatch is an important concept in thin films and the degree of epitaxial strain in the film has been observed to affect the functional properties of the films due to changes in the lattice, bond lengths, and bond angles in the crystal. This response has been observed, for example, in strain-induced magnetic phase changes and metal-to-insulator transitions [45, 48] and ferroelastic behavior in cobaltites [49]. Mismatch is represented quantitatively as:

$$f = \frac{a_{film} - a_{sub}}{a_{film}} \tag{1.2}$$

where values of a_{film} and a_{sub} are the in-plane lattice parameters of the film and substrate in an unstrained condition, respectively. In epitaxially strained films there are two competing energies: elastic strain energy, E_{el}, and the dislocation line energy of a single dislocation, E_{dis}. These energies are given in Ref. [50] by the following:

$$E_{el} = \frac{2G(1-\nu)}{1-\nu} f^2 h \tag{1.3}$$

and,

$$E_{dis} = \frac{Gb^2}{4\pi} \frac{1 - \nu\cos^2\theta}{1-\nu} \ln\frac{\alpha h}{b} \tag{1.4}$$

where, G is the bulk modulus, ν is Poisson's ratio, h is the film thickness, b is the Burger's vector, θ is the angle between the Burger's vector and the dislocation line, and α is a constant.

When the dislocation energy is larger than the strain energy, a dislocation is introduced. Thus, the critical thickness h_c, can be obtained by setting Equations 1.3 and 1.4 equal and solved for h to produce the following:

$$\frac{h_c/b}{\ln(\alpha h_c/b)} = \frac{1-\nu\cos^2\theta}{8\pi f(1+\nu)\cos\phi} \tag{1.5}$$

where, ϕ is the angle between the slip plane and the film surface. This ratio is shows an approximately inverse proportionality of h_c and f, meaning, the lower the misfit between film and substrate, the larger the critical thickness of film.

Epitaxial strain in thin films offers a rich parameter space for experimentation because large amounts of biaxial strain can be induced in the thin film that would likely fracture the bulk material, giving rise to material properties and phase transitions not accessible in the bulk form of the material [45].

Some perovskites are more readily manufactured as thin films than as a bulk material. For instance, $LuScO_3$ is a transition metal oxide that occurs only as a solid solution of two constituent oxides, Lu_2O_3 and Sc_2O_3 which assemble in the bixbyite structure with the formula (Mg, Fe)O_3. Numerous attempts to force this material into a metastable bulk perovskite structure failed until Heeg *et al.* demonstrated (in 2007) that epitaxially grown $LuScO_3$ thin films in the perovskite phase could be synthesized by pulsed laser deposition using $NdGaO_3$ (110) and $DyScO_3$ (110) substrates. The researchers found that films grown over a certain thickness (200nm) would preferentially form the bixbyite structure as opposed to the perovskite structure suggesting the system's critical thickness. These findings show that epitaxial stabilization could open the door for an even greater number of possible

perovskite oxides [51].

1.3.1 Crystal Field Splitting

Coordinated transition metals found in complex oxides give rise to an electronic structure that can lead to high or low spin states, and Jahn-Teller distortions (Section 1.3.2), offering additional degrees of freedom for tailoring materials. Consider a single metal cation with a spherical distribution of electron charge. The d-orbital electrons in this configuration are in a degenerate state, i.e., all having equal energy. In octahedrally coordinated transition metal oxide crystal structures, the d-orbital electrons overlap with the $2p$ electron fields of the oxygen anion ligand as shown in Figure 1.7. This overlap causes Coulombic repulsion between the two like-charges, which in turn, causes the degeneracy to split into orbitals of higher and lower energy while keeping the overall energy the same [52].

In octahedrally coordinated transition metals, the $d_{x^2-y^2}$ and d_{z^2} orbitals directly overlap with the neighboring ligands, thus raising the system's repulsive electrostatic energy and creating a splitting of d-orbitals denoted as e_g. Conversely, the d_{xy}, d_{xz}, and d_{yz} orbitals do not directly overlap the negatively charged oxygen ligands, thus lowering the electrostatic energy of these electron orbitals and creating a state denoted as t_{2g}. This phenomenon is known as crystal field splitting and the energy difference between the split orbitals is known as the crystal field stabilization energy (CFSE). This energy is denoted in octahedral systems as Δ_o, in tetrahedral systems as Δ_t, and in square planar systems as Δ_{sp}.

When a transition metal cation is tetrahedrally coordinated, there is no complete overlap between the transition metal d-orbitals and the negatively charged oxygen anion. As shown in Figure 1.7, the d_{xy}, d_{xz}, and d_{yz} orbitals have higher overlap between the d-orbital and the anion, producing a higher electrostatic potential and higher energy state denoted as

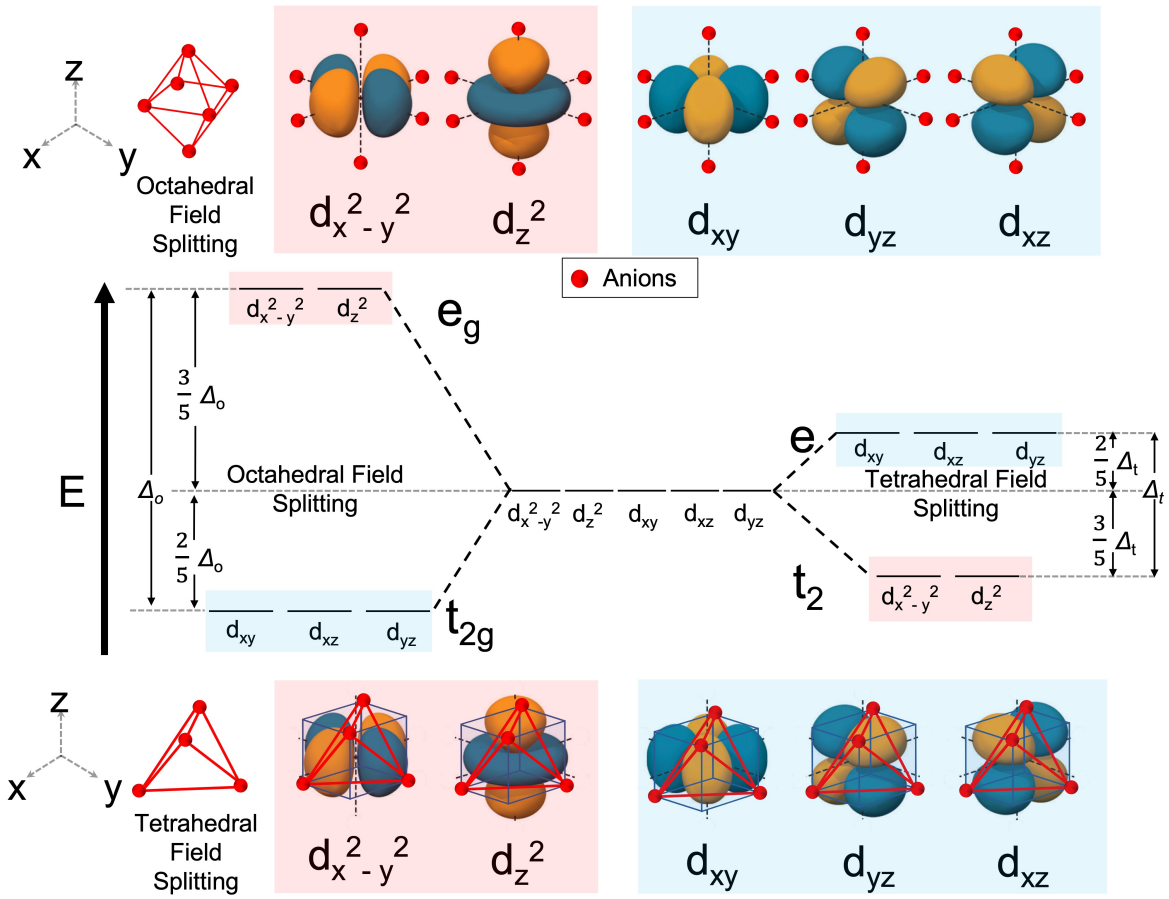

Figure 1.7: Schematic of crystal field splitting of transition metal oxides in octahedral and tetrahedral coordination (adapted from [52]).

e. In comparison, in the $d_{x^2-y^2}$ and d_{z^2} orbitals, there is less overlap, producing a lower electrostatic potential and a lower energy state denoted as t_2.

As electrons fill the orbitals, there are multiple possible states because of the competing CFSE and electron spin pairing energy (SPE) which is the repulsive Coulombic force between two electrons (of opposite spin) sharing an orbital. Depending on the CFSE and SPE, the electrons can fill orbitals in a manner that creates more or fewer unpaired electrons, creating states of high spin or low spin, respectively [52]. When the CFSE is less than the SPE, the electrons will populate the shell in a manner that maximizes the number of occupied

orbitals, creating a "high spin" complex. In contrast, "low spin" complexes arise when the SPE is lower than the CFSE, and the electrons populate the shell in a way that maximizes the number of paired electrons, thus minimizing the number of partially occupied orbitals. In octahedral complexes, high/low spin states are only possible for d^4 through d^7 electron configurations because in d^1 to d^3, the t_{2g} orbital is still being populated (d^1 though d^3 corresponds to $t_{2g}^1 e_g^0$ through $t_{2g}^3 e_g^0$). In d^8 through d^{10}, the t_{2g} orbital can only be fully occupied (d^8 and d^9 correspond to $t_{2g}^6 e_g^2$ and $t_{2g}^6 e_g^3$, respectively and d^{10} corresponds to $t_{2g}^6 e_g^4$).

For tetrahedrally coordinated transition metals, $\Delta_t = 0.44\Delta_o$ and this value is often lower than the SPE so tetrahedral complexes are almost always high spin [52]; however, low spin tetrahedral complexes have been confirmed in rare cases [53].

Finally, the square planar complex can be thought of as an octahedral complex with its apical anions (the ligands along the z-axis) removed. A schematic of the field splitting in square planar complexes is shown in Figure 1.8. For square planar coordinated transition metals, $\Delta_{sp} = 1.74\Delta_o$ which is higher than the SPE, making electrons preferentially pair, so usually only low spin states are observed in square planar complexes, specifically with a d^8 electron configuration, but exceptions to this observation have also been observed [54].

1.3.2 Jahn-Teller Distortions

The Jahn-Teller theorem states that "...stability and degeneracy are not possible simultaneously unless the molecule is a linear one..." and the authors show that in energetically degenerate (and thus unstable) configurations, the degeneracy breaks so that the system is stabilized [55]. This degeneracy breaking leads to a reduction in the symmetry of the system by the shortening or elongating of bond lengths between a central ion and the surrounding ligands and is shown in Figure 1.8.

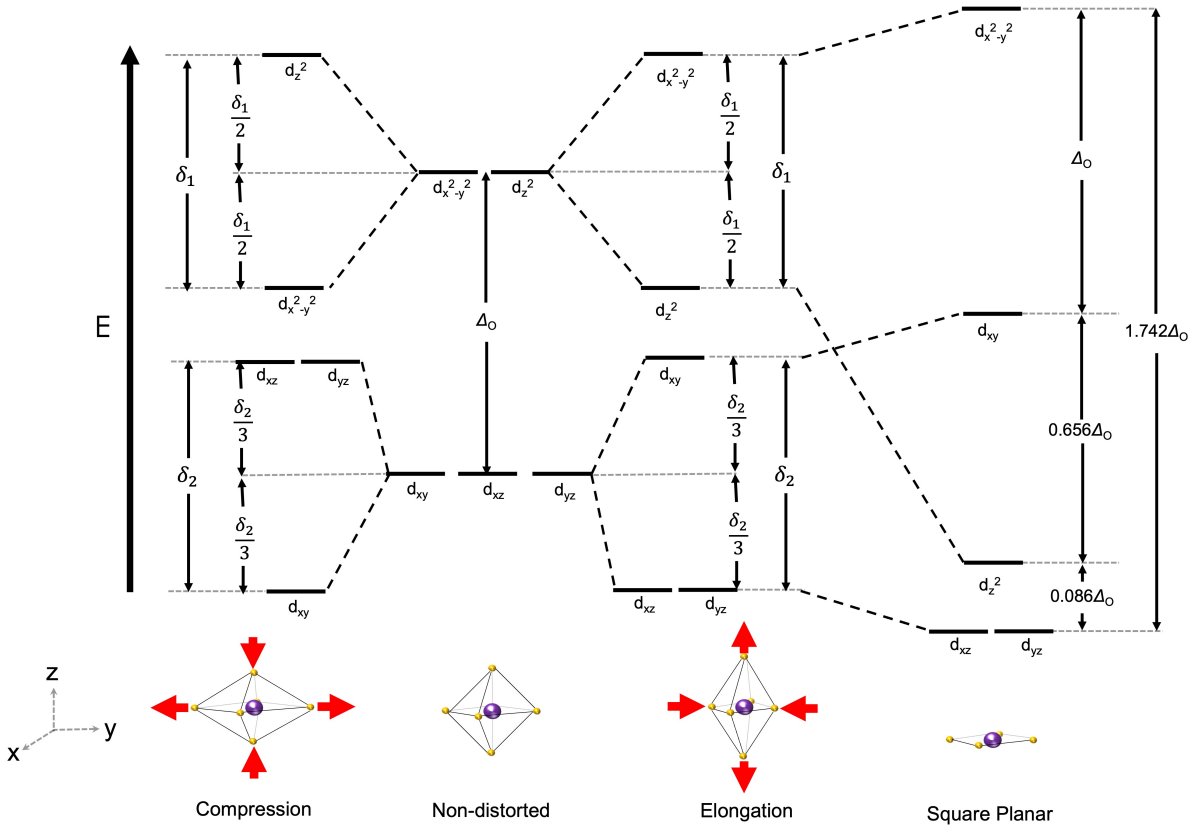

Figure 1.8: Jahn-Teller distortions in octahedral complexes and the square planar crystal field splitting (not shown to scale). The degeneracy of the e_g and t_{2g} orbitals cannot coexist with stability, so the complex stabilizes by changing the metal-ligand bond length thus breaking symmetry by compressing or elongating the octahedron. The square planar complex can be thought of as an extreme case of Jahn-Teller elongation in an octahedral complex (adapted from [52]).

However, not all electron configurations are Jahn-Teller "active" and the requirements for Jahn-Teller distortions to occur are explained as follows. Jahn-Teller active electron configurations are those with asymmetrically filled orbitals and occur most often in octahedral complexes but minor Jahn-Teller distortions are also observed in tetrahedral systems. Symmetrical filling of the e_g and t_{2g} orbitals occurs whenever these orbitals are empty, half full, or completely full as shown in Figure 1.9, and all other scenarios are considered asymmetrical.

For example, octahedral systems with t_{2g}^3 configurations have electrons that fill the t_{2g} orbital in a way that the electrons are balanced and therefore $t_{2g}^3 e_g^0$ systems are not Jahn-Teller active. Other Jahn-Teller inactive configurations include d^8 ($t_{2g}^6 e_g^2$), d^{10} ($t_{2g}^6 e_g^4$), high-spin d_H^5 ($t_{2g}^3 e_g^2$), and low-spin d_L^6 ($t_{2g}^6 e_g^0$) and all have evenly occupied t_{2g} or both t_{2g} and e_g orbitals. All other d-orbital electron configurations in octahedral complexes are Jahn-Teller active and can further be classified as "strong" and "weak" depending on if the imbalance in degenerate orbital population is in the e_g or t_{2g} orbital, respectively.

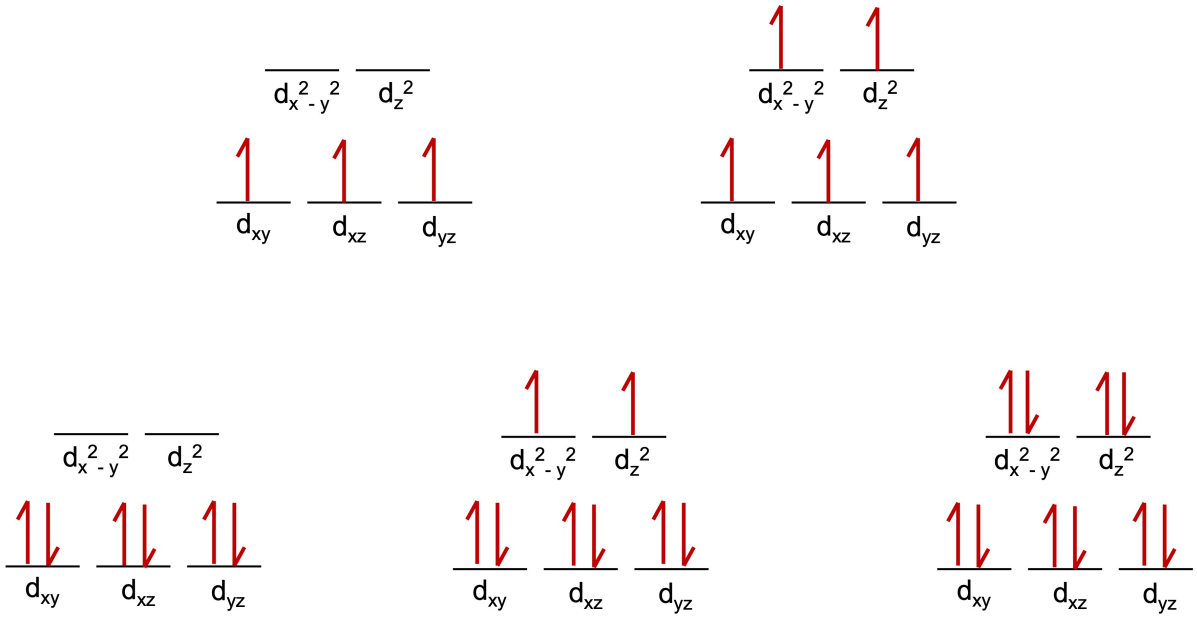

Figure 1.9: Possible symmetrical d-orbital filling. These electronic configurations in octahedral coordination are Jahn-Teller inactive and all other states of the d-orbital electron filling will cause strong or weak Jahn-Teller distortions depending on whether the imbalanced electron exists in either the e_g or t_{2g} orbital, respectively.

1.4 Magnetic Phenomena in Perovskites

In complex oxides, magnetic states arise from indirect exchange mechanisms, where the electron spin from one B-site cation couples to that of the next through an intermediate step.

The double exchange mechanism arises between cations of different valence separated by an oxygen anion that allow an extra electron from one cation from the d-orbital to travel back and forth between the two cations [56], as shown in Figure 1.10. The electron is quantum mechanically forbidden from changing its spin while hopping from cation to anion to cation, so the probability of transition between cations is highest between cations with the same spin polarization which promotes ferromagnetic (FM) ordering below the Curie temperature T_C, and the hopping probability is lowest for cations with randomly aligned spins, observed as paramagnetism in magnetic materials above T_C or their Néel temperature (T_N) in antiferromagnetic (AFM) materials. In other words, the itinerant electron promotes FM ordering between the two metal cations where their magnetic dipole moments created by their electron spins align in the same direction. The electron mobility also leads to metallic, electrically conducting behavior in these materials and conversely, the lack of electron mobility causes electrically insulating behavior. The electronic and magnetic response of complex oxides can therefore be altered by the same stimuli that change the valence of the B-site cation in the crystal such as aliovalent doping.

Mixed-valence B-site cations can be synthetically forced by adding an A-site dopant that has a different valence from the primary A-site cation. Such is the case with $La_{1-x}Sr_xMnO_3$ where $LaMnO_3$ is doped with divalent Sr, where a certain number "x" of La^{3+} cations are replaced with an equal number of Sr^{2+} cations. Because the two A-site cations are different valence state, the valence of the B-site cation increases. In $LaMnO_3$, the B-site cation is Mn^{3+} and in $La_{1-x}Sr_xMnO_3$ the B-site cation valence increases to $Mn^{(3+x)+}$, implying the Mn exists in mixed-valence states of Mn^{3+} and Mn^{4+} which leads to FM ordering as seen in the Sr concentration dependent phase diagram shown in Figure 1.11.

The superexchange mechanism is attributed to AFM ordering in complex oxides in accor-

dance with the Goodenough-Kanamori-Anderson Rules [57] as shown in Figure 1.10. This phenomenon—like the double exchange mechanism—involves magnetism arising from indirect electron interactions between two cations with a non-magnetic species that serves as an intermediary. Consider the $LaMnO_3$ case, with Mn^{3+} valence states having the electron configuration $t_{2g}^3 e_g^1$ and with the electron spins of each cation in the same direction. The $3e_g^1$ electron can occupy either the d_{z^2} or the $d_{x^2-y^2}$ orbitals (as a side note, this will cause Jahn-Teller distortions to eliminate the degeneracy). In the Mn–O–Mn bond with both Mn cations having their e_g electron in the d_{z^2} orbitals and the oxygen anion orbital sharing via the p_z orbital, an electron is shared between the anion and each cation. This electron can only be shared in the bond if it can partially occupy the orbitals of both the anion and the cations and this is only possible if the spins of the Mn cations are of opposite direction, which leads to AFM ordering. If instead, the electron is shared on one side of the Mn–O–Mn bond via the already partially occupied d_{z^2} orbital (i.e., the electron pairs in the d_{z^2} orbital), then this can only occur if the spins on both cations are parallel leading to FM ordering.

1.5 Past Studies

As mentioned in Section 1.1, cobaltite perovskites are of high interest in topotaxy because of their low oxygen vacancy formation energy, high oxygen vacancy diffusivity, and well defined metal-to-insulator transitions (MIT) where the material changes from electrically conducting to an insulating state, or vice versa. The previous work of Dr. I-Ting Chiu included studies of the topotactic phase transformations that can be induced in perovskite systems [6, 59]. In her cobaltite experiments, she synthesized thin films of $LaCoO_3$ (LCO) and $La_{0.7}Sr_{0.3}CoO_3$ (LSCO) epitaxially grown on (001)-oriented $(LaAlO_3)_{0.3}(Sr_2TaAlO_6)_{0.7}$ (LSAT) substrates which were then annealed at several temperatures and pressures of P_{O2}. The phase diagram for LSCO is shown in Figure 1.12. Topotaxy was confirmed by structural and magnetic

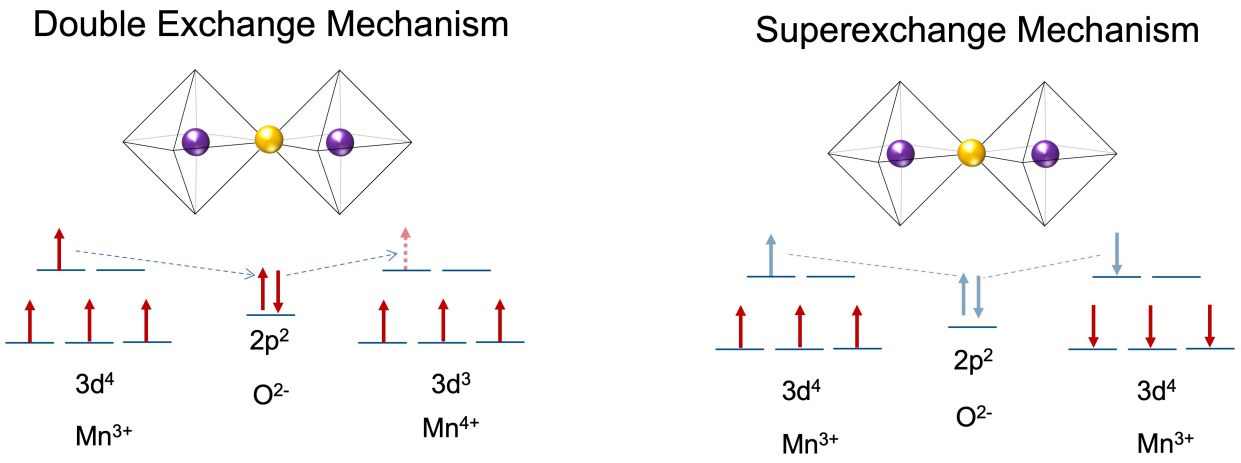

Figure 1.10: Indirect exchange mechanisms in complex oxides. The double exchange mechanism is responsible for FM ordering and involves the hopping of an electron which can only occur if the two transition metal cations have spins oriented in a manner that can accept an electron of the same spin. The superexchange mechanism involves "virtual" electrons being shared between the anion and transition metal cation where the electron which promotes both AFM and FM ordering as discussed in the text. The AFM ordering case is shown here for the superexchange mechanism.

characterization techniques (described in Section 2.2) and the results are shown in Figures 1.13 and 1.14.

Beginning in the perovskite phase, the thin films underwent topotactic phase transformations that were dependent on the degree of the reducing conditions. At the 400°C, 10^{-12} atm P_{O2} annealing condition, the LCO thin film transformed into a mixed phase of BM and GR, and the LSCO thin film became a single phase of BM. Under the 600°C condition and the same pressure of oxygen, both samples, no distinct diffraction peaks are observed and these implications are explained in detail in Section 2.2. Further analysis of the LSCO sample confirmed that a polycrystalline RP phase was present as well as cobalt nanoparticles (NP).

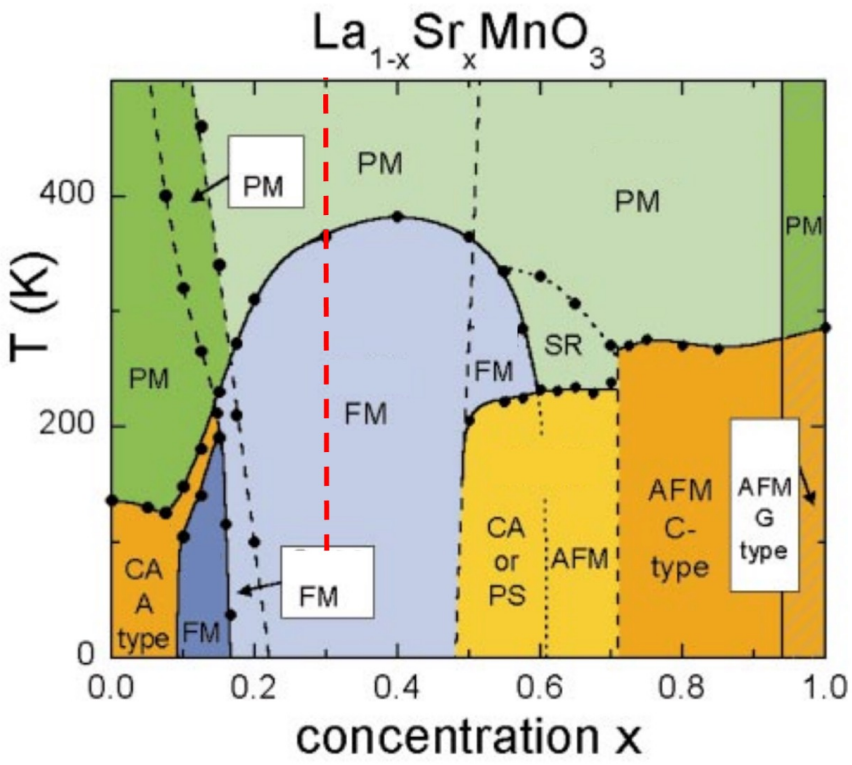

Figure 1.11: $La_{1-x}Sr_xMnO_3$ phase diagram. At the extreme left and right sides of the figure, Sr dopant concentration $x = 0.0$ and $x = 1.0$, respectively, and the compositions reduce to $LaMnO_3$ and $SrMnO_3$, respectively. The resulting magnetic ordering is AFM in both cases because of the superexchange mechanism arising from isovalent Mn at the B-sites in the perovskite. AFM ordering can be further classified as A-type, C-type, or G-type, and can also include canted (CA) spins. Short-range (SR) order and phase-separated (PS) ordering can also be differentiated as the Sr doping level is changed (adapted from Ref. [58]).

Annealing the LCO and LSCO at 900°C recrystallized the thin films and formed a single phase of RP in the LSCO and a mixed phase of RP phase and an unknown phase in the LCO sample.

Functional properties of Dr. Chiu's thin films were studied using a technique known as X-ray magnetic circular dichroism (discussed in Section 2.3.2) which gives the relative strength of

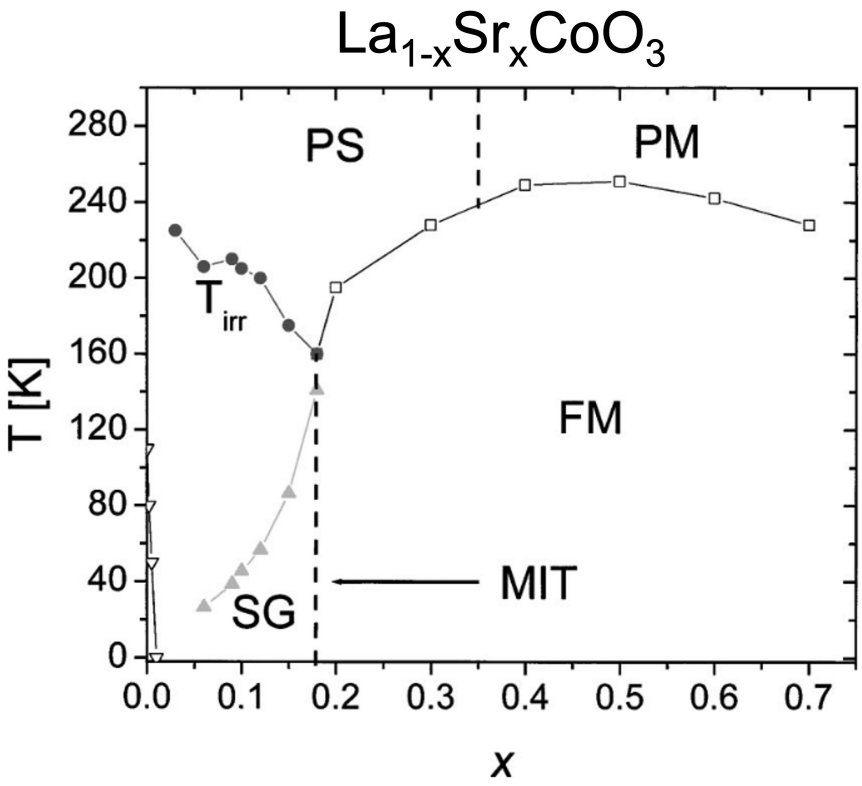

Figure 1.12: $La_{1-x}Sr_xCoO_3$ phase diagram. At the extreme left and right sides of the figure, Sr dopant concentration $x = 0.0$ and $x = 0.75$, respectively, and the compositions reduce to $LaCoO_3$ and $La_{0.25}Sr_{0.75}CoO_3$, respectively. The majority of the phase space is ferromagnetic (FM), and the high-temperature regions labelled "PS" and "PM" denote the paramagnetic semiconductor and paramagnetic metallic phases, respectively, with the transition occurring between $x = 0.3$ and 0.35. Below the MIT doping level of $x = 0.18$, a spin glass (SG) phase exists where the magnetic domains take on local order, but do not show long-range order. The T_{irr} is the irreversibly temperature explained in Ref. [60]. The region marked with open triangles are the estimated spin state transition temperature which is described further in Ref. [61], (figure from Ref. [60]).

the ferromagnetic response in the sample that is placed in a magnetic field. The data from these experiments were collected at 80K and are shown in Figure 1.14. The LCO had no ferromagnetic signal in its as-grown state nor in the samples annealed at 400°C or 900°C,

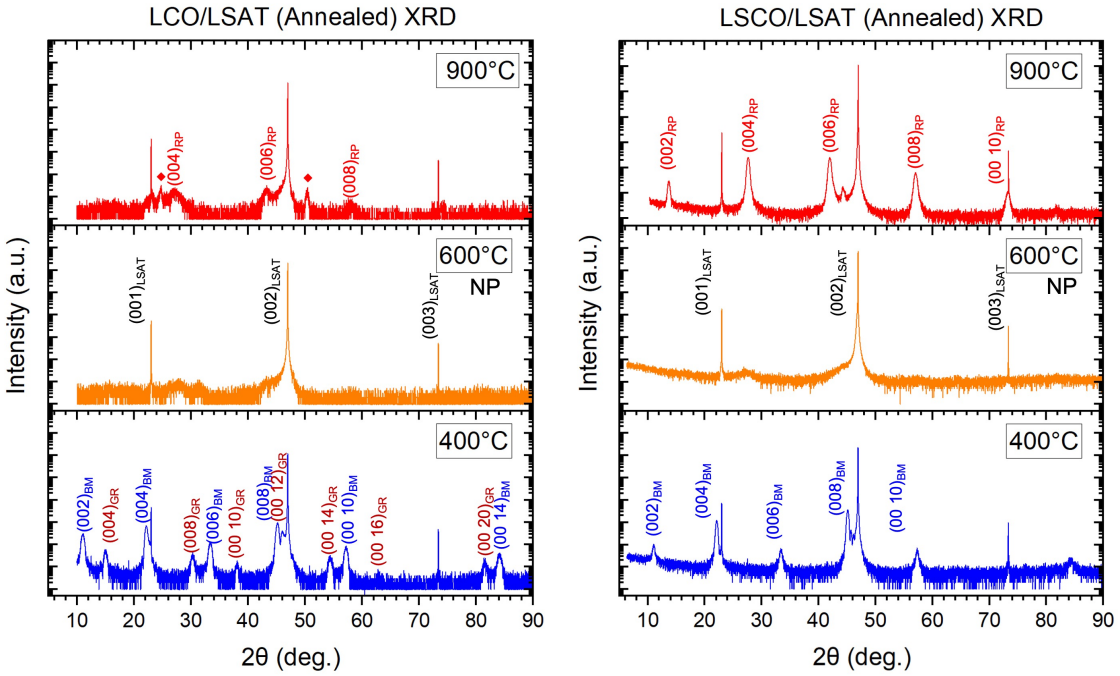

Figure 1.13: The results of past structural studies on topotaxy in cobaltite perovskites which were annealed at varying temperatures and 10^{-12} atm of P_{O_2}. The GR phase is observed at the 400°C anneal in the LCO/LSAT system, but not the LSCO/LSAT system and both systems showed the presence of the BM phase. In both sets of samples, the 600°C samples showed a diminished crystalline quality, which for the LSCO was attributed to a combination of polycrystalline RP phase and cobalt nanoparticles (NP). The structure transformed into the epitaxial RP phase at 900°C in both samples and in the LCO thin film, there was another unidentified phase present, denoted with a ♦.

while the 600°C sample showed a large ferromagnetic signal; evidence that supports the presence of metallic cobalt nanoparticles. The LSCO samples showed a variety of ferromagnetic responses beginning with a ferromagnetic signal in the as-grown condition which gradually decreases in strength as the annealing progresses to more reducing conditions. The polycrystalline RP and nanoparticle mixed phase has a strong ferromagnetic response due to the cobalt nanoparticles. Finally, the RP single phase which arises from the highest temperature anneal shows no observable ferromagnetic signal by XMCD for either the LSCO or LCO

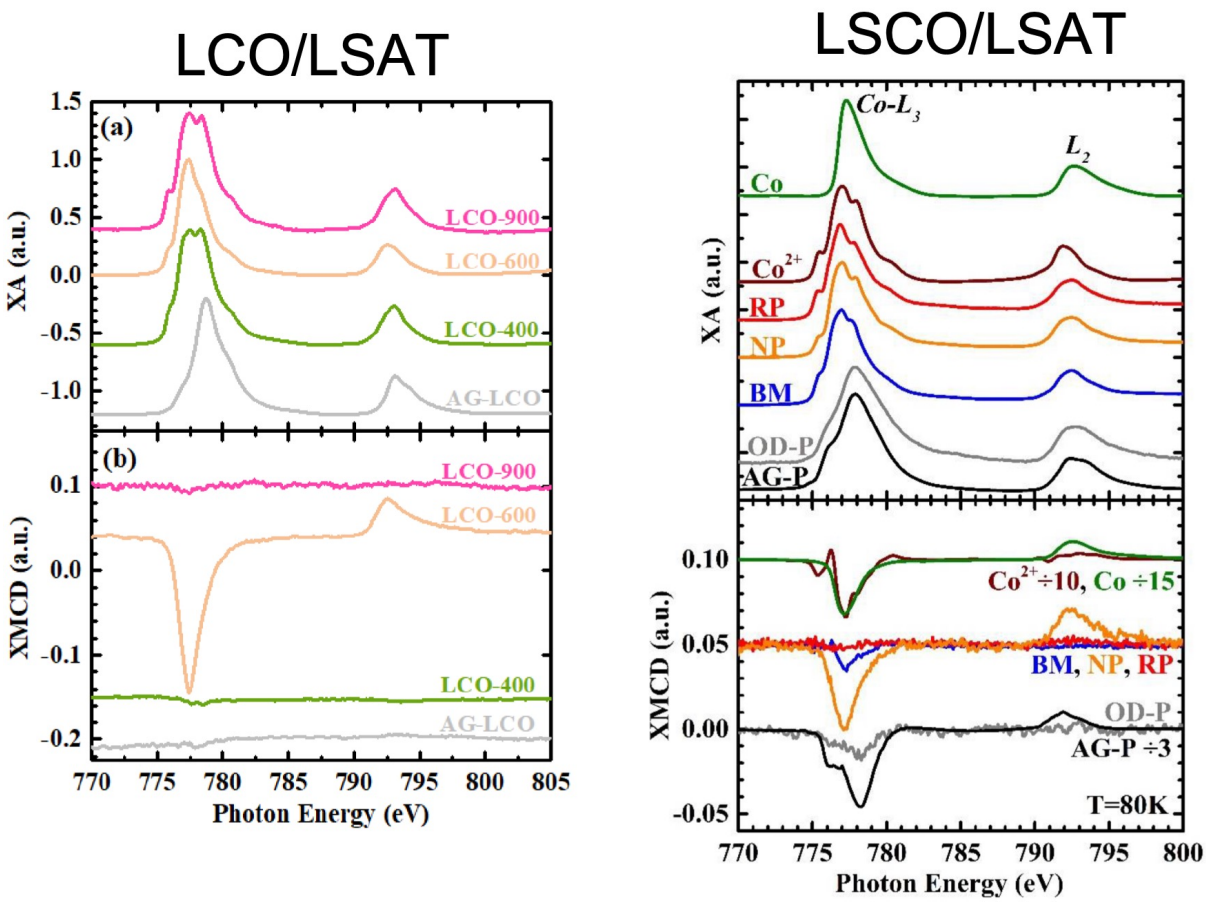

Figure 1.14: The results of past magnetic studies on topotactic phase transformations in cobaltite perovskites [59]. Soft X-ray absorption spectroscopy is discussed in Section 2.3.2.

samples.

1.6 Project Overview

$La_{0.7}Sr_{0.3}MnO_3$ (LSMO) is a perovskite oxide of particular interest because it offers a rich parameter space for experimentation and the functional properties that are accessible by tuning the material parameters consist of ferromagnetism, antiferromagnetism, and colossal magnetoresistance. These properties are desirable in several technological areas of research such as resistive random access memory (RRAM) [62], and spintronics [63]. Numerous

studies have been performed on LSMO and a number of stable phases are made possible by changing the Sr-dopant concentration, epitaxial strain state, interfacial composition, or film thickness. The first aim of this thesis is to study the changes in magnetic properties due to topotactic phase transformations induced in LSMO as a function of annealing temperature and then to compare these results with similar studies performed on other first-row transition metal systems previously studied [6, 59].

The second aim of this thesis is to study the effect of alternating the stacking order of cobaltite bilayers on topotactic phase transformations and to compare the resulting changes in magnetic properties between the two arrangements.

To address these research goals, I first synthesized LSMO thin films on LSAT substrates. Next, the samples were annealed at different temperatures using facilities at the University of California, San Diego (UCSD), then I structurally and magnetically characterized the samples. In my cobaltite studies, I synthesized bilayer systems composed of two individual thin film layers of LCO and LSCO on LSAT substrates and varied the stacking order as LCO/LSCO/LSAT and LSCO/LCO/LSAT so that two sets of samples could be compared and the effect of stacking order could be studied. A diagram of the composition of the samples I grew and studied is shown in Figure 1.15.

1.7 Summary

This chapter discussed the background of crystalline materials and structural and magnetic phenomena observed in complex oxides, namely of the perovskite structure. Perovskite and perovskite-related oxide phases observed in this thesis were introduced and characteristics and possible applications were outlined. Past studies were summarized to set the motivation

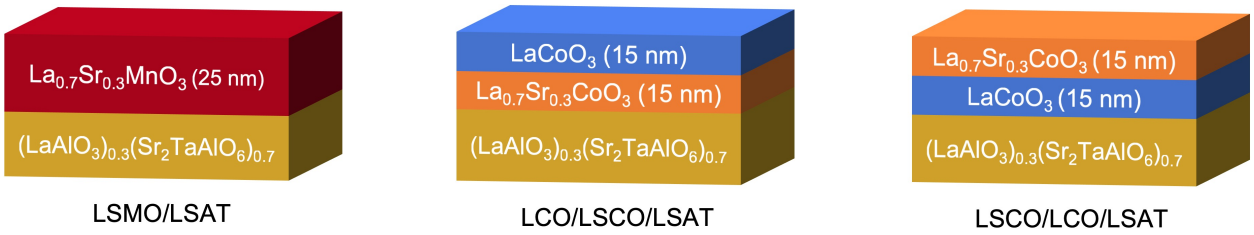

Figure 1.15: Thin films of LSMO were deposited on LSAT substrates to study the structural phases and magnetic properties available by topotactic phase transformation. The two bilayer configurations alternated two layers of LCO and LSCO also deposited on LSAT substrates so that the effect of stacking order on topotactic phase transformations and their magnetic properties could be studied.

for this thesis and the project overview was covered. Because of their strong interconnection between the effects of electrons in the perovskite oxides, they can be tuned for specific, or multiple functionalities by adjusting their composition or strain state, and they are often referred to hold spin, orbital, lattice, and/or charge degrees of freedom.

In Chapter 2, I will discuss the synthesis and characterization methods used in this thesis, as well as other methods that were used in similar studies. Chapter 3 will cover the results of the characterization of the three families of samples (i.e., the manganite thin films, and the two separate stacking orders of cobaltite bilayers). Finally, Chapter 4 will include the outcomes and conclusions drawn from this thesis, as well as opportunities for future studies.

Chapter 2

Methods

The techniques used to synthesize, treat, and characterize the samples in this thesis are described in this chapter. To study the crystal structure of these materials, high quality, single crystal thin films of uniform thickness were fabricated using pulsed laser deposition (PLD). The samples were then characterized using several X-ray techniques and then they were sent to undergo annealing in an oxygen gas evolution system at UCSD where a low partial pressure of oxygen and varying temperature conditions were used to induce topotactic phase transformations in the thin films. The samples were again characterized using X-ray techniques to observe the structural and magnetic changes that the topotactic phase transformations produced in the samples.

2.1 Synthesis Methods

2.1.1 Pulsed Laser Deposition

PLD is a physical vapor deposition technique which allows for the near-stoichiometric transfer of target material to the substrate. In other words, the target material usually must be the same stoichiometry as the desired film material, with some exceptions [64]. There are several growth parameters that must be optimized for high crystallinity and near-stoichiometric transfer of material to occur including laser fluence, laser spot size, laser pulse rate, substrate temperature, target-to-substrate distance, and process gas pressure. The deposition process involves placing a cleaned substrate chip in a vacuum chamber. The vacuum chamber is evacuated using a series of vacuum pumps to ensure a clean and controlled environment during the film deposition. The substrate is then heated to control the crystallinity of the material which can be amorphous near room temperature, or a single crystal at temperatures of 700°C - 900°C for perovskite thin film synthesis using PLD.

A beam of electromagnetic radiation is generated in the laser and emitted through a series of optics before entering the vacuum chamber through a quartz viewport. The beam strikes a selected rotating target, ablating a plume of the target material which deposits a thin layer of material onto the heated rotating substrate. The thermal energy from the substrate heater gives the adhered atoms ("adatoms") of target material sufficient kinetic energy to migrate on the surface and settle into the lowest energy configuration. The shape of the plasma plume is comparable to that of a Christmas tree light bulb: spherical on the bottom near the target and terminating into a conical point a few centimeters above the target, and its shape is dictated by the process gas composition and pressure. The terminus of the plume is where the substrate should be positioned since the relative distance from the substrate to the plume affects the quality film produced.

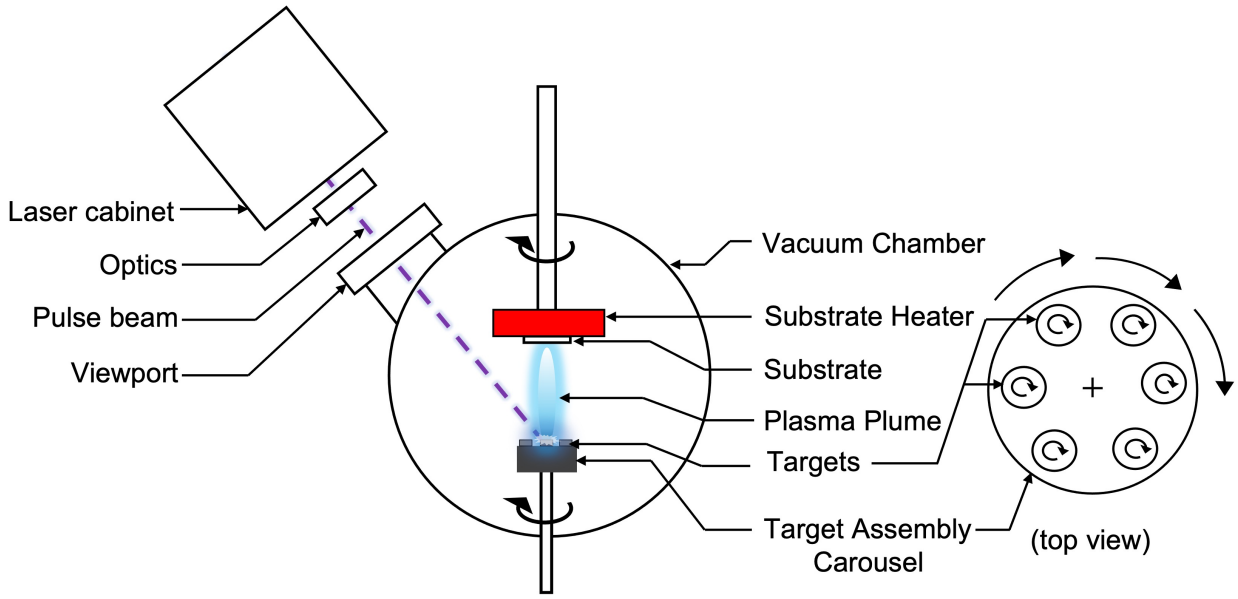

Figure 2.1: Line diagram of the Takamura Research Group PLD chamber. The electromagnetic radiation is generated in the laser cabinet and the beam passes through the optics and viewport into the vacuum chamber. The substrate is adhered to a heated plate which rotates to promote even growth and the targets rotate to ensure even ablation and plume characteristics. The target carousel can rotate to allow for the selection of one or more targets for growth of thin films or heterostructures (diagram adapted from NBM Design, Inc. product brochure) [65].

Many different techniques can be used for the synthesis of thin films such as sputtering, molecular beam epitaxy, electron beam epitaxy, spin coating, solution processing, and atomic layer deposition. Layering of thin films allows for the study of the complex interplay between two or more different films and can be accomplished in PLD by depositing a film onto another film that was deposited onto the substrate. This method is especially useful in heterostructures requiring materials with differing electronic or magnetic properties to coexist. PLD is the choice synthesis method for this thesis because of its near-stoichiometric transfer of material from target to substrate, its relative ease and speed of single-crystal thin film growth, and its ease of growing perovskite heterostructures.

2.1.2 Gas Evolution Annealing Chamber

The annealing was performed by collaborator Junjie Li at UCSD using a gas evolution chamber [66]. The samples were placed in a vacuum chamber that is pumped down and a furnace heats the sample to a specified temperature while oxygen is supplied by a computer-controlled valve. A temperature controller and a gas flow controller maintain the parameters for the annealing treatment and a residual gas analyzer and mass spectrometer monitor the partial pressure of oxygen, (P_{O2}). The samples in this thesis were annealed for a period of one hour in a low P_{O2} (ranging from 10^{-12} to $10^{-7} atm$ P_{O2}) at various temperatures (ranging from 400°C - 900°C) to induce the topotactic phase transformations.

2.2 Structural Characterization Techniques

After the films are grown, their structural characteristics and quality must be measured to ensure they were grown as desired and to quantify physical properties. The qualities of interest are the film's roughness, thickness, density, crystal lattice parameters, and epitaxial strain state including mosaicity. These properties were measured using the Bruker D8 Discover X-ray diffraction system.

2.2.1 X-Ray Diffraction

X-ray diffraction (XRD) experiments make use of X-rays called "characteristic X-rays" which are generated in the anode of the X-ray tube, producing a beam of X-rays consisting of $K_{\alpha 1}$, $K_{\alpha 2}$, and K_{β}. Many choices of anode exist depending on the desired wavelength including iron, cobalt, copper, and molybdenum. These X-ray wavelengths are of similar length scale of the interatomic spacing of the atoms in the crystalline materials which allows for a phenomenon known as diffraction to occur. When a wave scatters off two close objects and the scattered waves interfere, diffraction occurs. If two or more waves of equal wavelength are

perfectly in phase (i.e., their peak amplitudes align), then constructive interference occurs, and the amplitude of the resultant wave is the sum of the constituent waves. Conversely, if the two or more waves are out of phase, destructive interference occurs where the resulting signal is still the sum of the incoming waves, but the amplitude is diminished. Two waves of equal wavelength, λ and amplitude are perfectly out of phase when one of their phases is shifted by $\lambda/2$, and the signal is annihilated. As shown in the XRD schematic in Figure 2.2, the angle of incidence to the sample is swept across some range, and in doing so, there are certain angles that satisfy the condition for perfect constructive interference and these peak intensities are used to determine a crystal's d-spacing. This condition is known as Bragg's Law named after the father-son duo who were both awarded the Nobel Prize in 1915 for their determination of several crystal structures using X-ray crystallography. In XRD experiments, the X-rays are monochromated so that diffraction is occurring from only one wavelength of light, thus producing sharper peaks. Kα_1 characteristic X-rays have a wavelength of 1.5406 Å and it is chosen for thin film XRD because it has the highest intensity.

$$n\lambda = 2dsin\theta \tag{2.1}$$

Equation 2.1 is Bragg's Law, where n is the diffraction order, λ is the wavelength of radiation used, d is the d-spacing which is the distance between certain parallel planes in the crystal structure, and θ is the incidence/exit angle of the radiation. Rearranging the equation, d-spacing can be found and used to convert to out-of-plane lattice parameter, c. Figure 2.3 shows three of the seven crystal systems and their symmetries as well as the equations used to find the lattice parameters.

High-resolution XRD (HRXRD) refers to a technique used for characterizing epitaxial films by using highly monochromatic X-rays and finer angular scan resolution over a smaller range

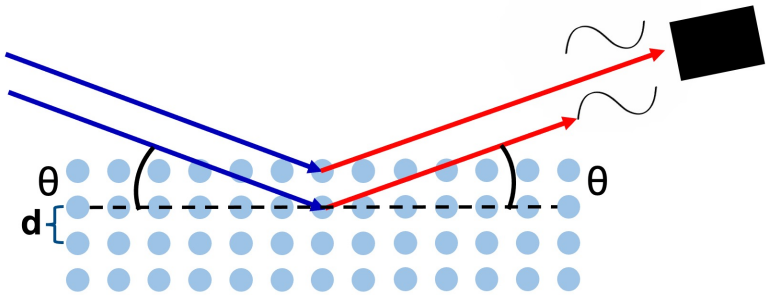

Figure 2.2: As incoming X-rays interact with the atoms in the crystal lattice, some of them penetrate deeper into the material and are scattered by the next lower plane of atoms. There exists a certain angle, θ, the Bragg angle, where the scattered X-ray path length will be an integer number of wavelength apart, generating constructive interference. This results in a peak in diffracted intensity that is measured by the detector depicted as a black box on the right side of the diagram.

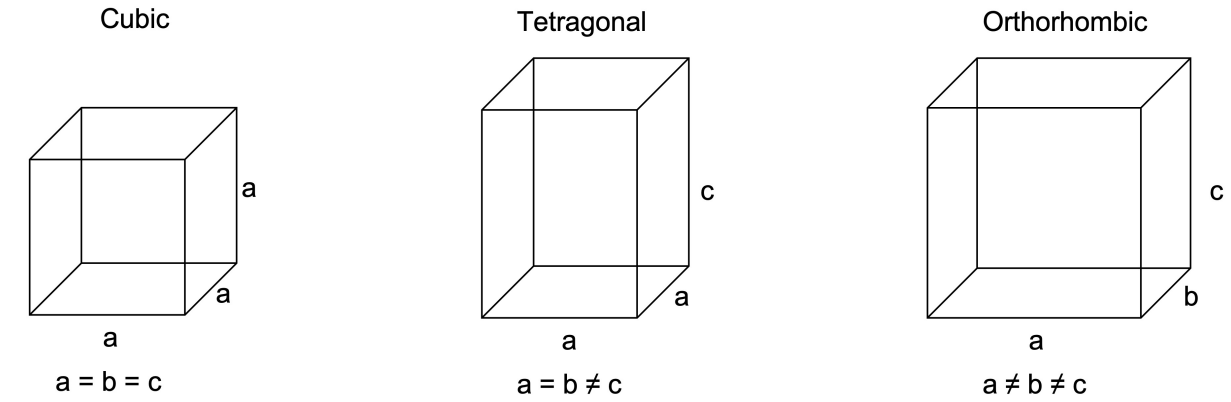

Figure 2.3: Three of the seven crystal systems, their geometry, and their d-spacing formulas. Notice for the {00L} family of planes, that each of the formulas reduce to $a = ld$ or $c = ld$.

of 2θ to help determine the structural properties of the samples. The features of the HRXRD scan shown in Figure 2.4 help elucidate the film's thickness. These calculations are made with the use of computer analysis tools such as DIFFRAC.LEPTOS [67].

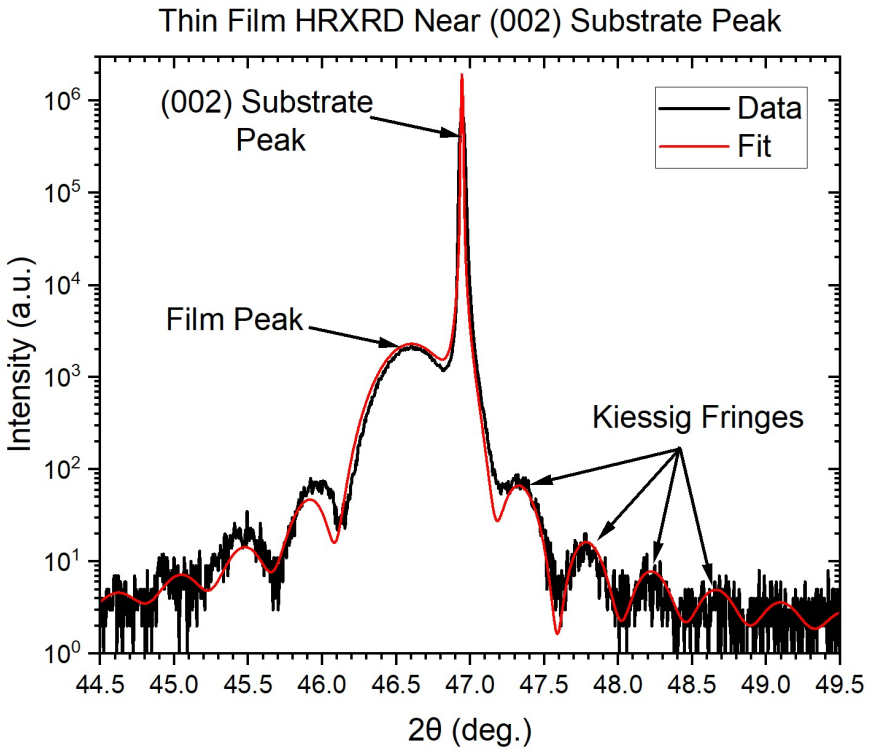

Figure 2.4: Example HRXRD diffractogram of an LSMO thin film near the (002) LSAT substrate peak. The high-intensity peak is from the substrate and the peak of lower intensity is from the film. Oscillations called Kiessig fringes appear on either side of the peaks and the periodicity and intensity of these fringes give insight to the film's thickness. This data can be also used to determine the substrate and film out-of-plane lattice parameter, as well as film and substrate roughness and density, along with film thickness.

2.2.2 X-Ray Reflectivity

Using the same X-ray source, sample, and detector geometry can be arranged so that the X-rays are at grazing angle of incidence to the sample, allowing the X-rays to reflect off the

sample. This arrangement is the premise for X-ray reflectivity (XRR) experiments and it can be used to determine the film thickness as well as the film and substrate roughness and density. Figure 2.5 shows a diagram of the XRR experimental configuration.

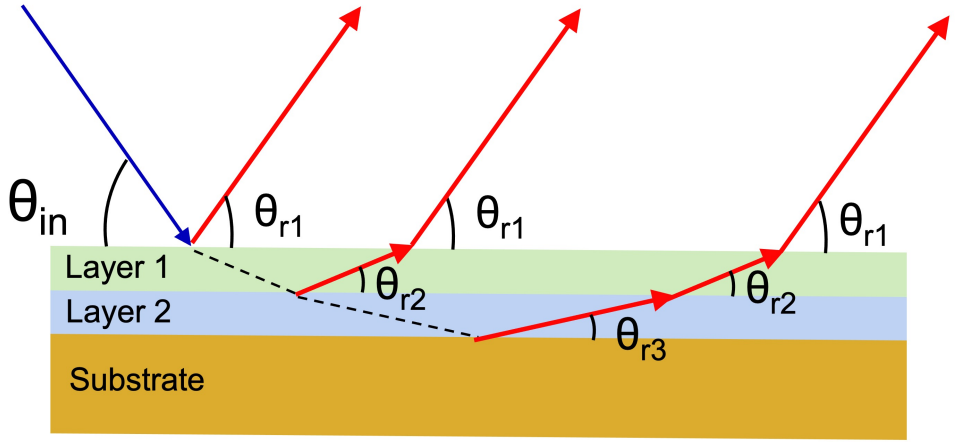

Figure 2.5: XRR experiment setup with angles shown exaggerated. Incident X-rays are shone onto the sample at some grazing angle θ_{in} and penetrate each interface by refraction. The refracted beams deflect by some amount depending on the (electron) density of the material and the reflected beams exit with the same angle as the incident beam. The roughness of the film surfaces and interfaces impacts the intensity of the reflected X-ray. The incident X-ray is swept across an angular range and the reflected intensity can be plotted and analyzed to obtain values for the film and substrate properties.

The critical angle (θ_c) is the angle below which the X-rays undergo total external reflection. This angle can be related to the electron density of the sample (and thus the material's physical density) through Snell's Law:

$$\sin\theta_{in} = n\sin\theta_{ex} \tag{2.2}$$

θ_{in} is the angle of incidence, n is the index of refraction, and θ_{ex} is the exit angle of the

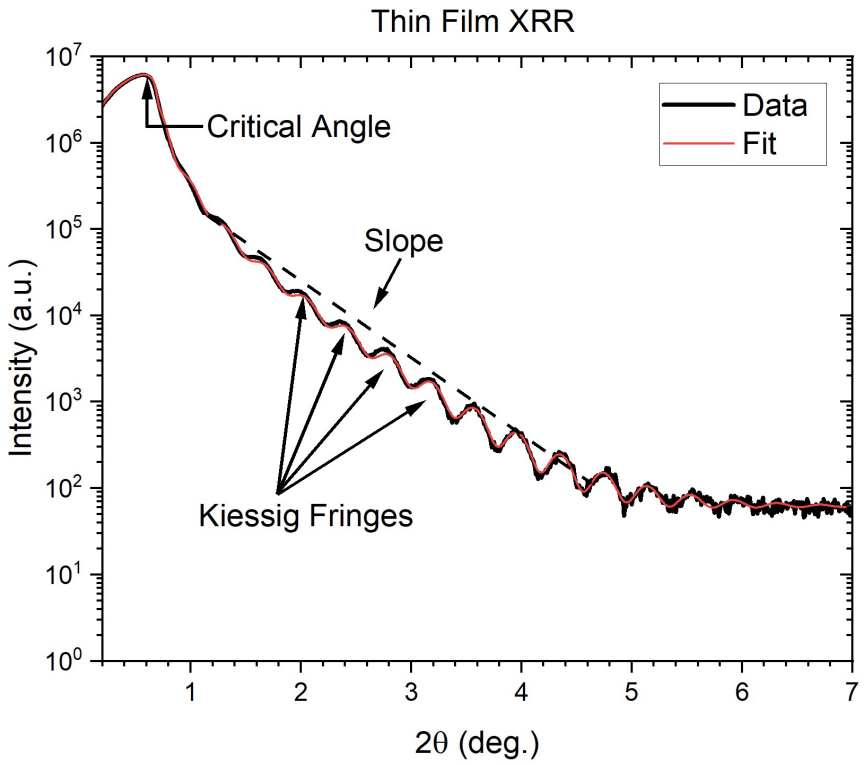

Figure 2.6: Example XRR data. The large drop in intensity at low 2θ is the critical angle below which is the region of complete reflection and its value is determined by the film's density. The slope gives information about the roughness of the film and substrate as reflected intensity decays quicker with higher roughness values. Lastly, the periodicity of the oscillations can be used to determine the thickness of the film. The fit is a simulation from GenX, an XRR fitting software used to obtain values for the film properties.

beam. For total external reflection to occur, $\theta_{ex} = 0$ and Equation 2.2 reduces to:

$$\sin\theta_c = n \tag{2.3}$$

Here, θ_c is the critical angle. The index of refraction can also be written as follows:

$$n = 1 - \delta \tag{2.4}$$

where,

$$\delta = \frac{r_e \rho_e \lambda^2}{2\pi} \tag{2.5}$$

r_e is the classical radius of the electron, and λ is the X-ray wavelength. The material's electron density is represented by ρ_e which can be written as:

$$\rho_e = \sum_k \frac{Z_k}{V_m} \tag{2.6}$$

Z_k is the number of electrons of atom k in the unit cell of the material, and V_m is the volume of the unit cell.

Using the small angle approximation for $\sin\theta_c$, Snell's Law reduces to:

$$\theta_c = \sqrt{2\delta} \tag{2.7}$$

therefore, $\theta_c \propto \rho_e$.

The relationship between thickness and the Kiessig fringes is as follows:

$$d = \frac{m\lambda}{2\sqrt{\theta_i^2 - \theta_c^2}} \tag{2.8}$$

where, θ_{im} is the angle at which the mth Kiessig fringe is found, θ_c is the critical angle, λ is the X-ray wavelength, and d is the film thickness.

In practice, these calculations are performed with the aid of computer simulation and curve

fitting tools such as GenX to give insight to the structural characteristics of the sample such as film thickness, and film or substrate roughness and density [68].

2.3 Magnetic and Electronic Characterization

2.3.1 X-Ray Photoemission Spectroscopy

A surface sensitive composition analysis technique called X-ray photoemission spectroscopy (XPS) was used to confirm the surface composition of the bilayers. It also highlighted the difference in electronic structure of the elements in the bilayers and the single layer thin films.

In XPS experiments, samples are placed in a vacuum chamber that is pumped down to ensure minimal gases are present which would interact with the X-rays. Aluminum K_α characteristic X-rays with a specific photon energy ($h\nu$) of 1486.7 eV are shone onto the sample and the X-rays interact with the core electrons in the sample, exciting some to the ionization continuum in a process called "photoemission". The intensity of the photoelectron decays exponentially with thickness of the sample, so only the top 10 nm of the material can be probed in XPS, following Equation 2.3.1. Because this technique detects the excited core level electrons, it cannot be used for detecting hydrogen or helium because these are the only elements without core level electrons. The kinetic energy (KE) of the photoelectrons is then measured and the binding energy (BE) can be calculated by Equation 2.9 and by also considering the work function, ϕ of the detector. The photoelectrons will have specific values of KE and thus BE depending on the elemental origin of the electron. A spectrum can be obtained which shows the energies of photoelectrons present in the sample and from this, the surface composition can be determined. An example XPS spectrum is shown in Figure 2.7.

$$BE = h\nu - KE - \phi \tag{2.9}$$

The intensity of the photoelectron $I(d)$ after it travels a distance d is given by:

$$I(d) = I_0 \exp\left(-\frac{d}{\lambda(E)}\right)$$

where I_0 is the initial intensity of the photoelectron and $\lambda(E)$ is the photoelectron's inelastic mean free path, which is defined as the distance the photoelectron can travel before decaying to $1/e$ of its initial intensity.

In addition to photoelectrons, another type of electron in XPS experiments known as Auger electrons. These electrons occur when a higher-level electron fills the vacancy left by the core shell electron, and their energy is transferred to excite a third electron from the atom. For example, a KLL Auger electron is emitted if a K-shell electron is excited by the incident X-ray, then an L-shell electron falls into the K-shell vacancy and the energy released is used to excite a neighboring L-shell electron to the continuum.

2.3.2 Soft X-ray Absorption Spectroscopy

To access information about the valence states of the B-site cations, soft X-ray absorption spectroscopy (XAS) was used at the Advanced Light Source (ALS) at Lawrence Berkeley National Laboratory (LBNL) in Berkeley, California. The distinction between "hard" and "soft" X-rays is not discrete, but hard X-rays refer to higher energy radiation (typically > 2 keV) than soft X-rays (typically < 2 keV) [69]. In XAS experiments, the X-ray energy is swept across an absorption edge where certain energy X-rays are absorbed by the electrons of certain elements in the material. This ability to tune the X-ray can give element-specific

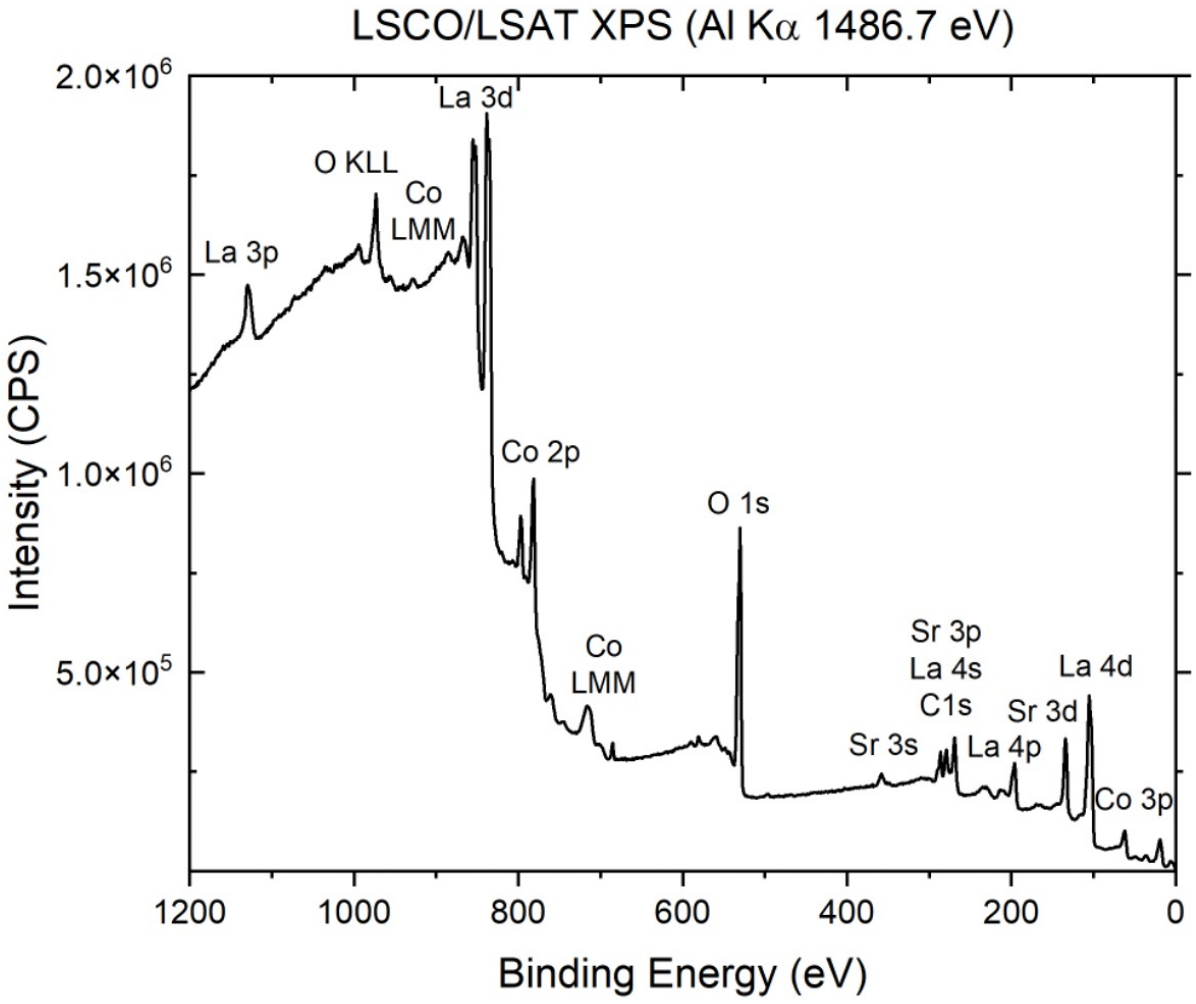

Figure 2.7: Example XPS spectrum of an LSCO/LCO/LSAT bilayer sample. The intensity corresponds to electron populations in the sample (e.g., La $3d$, co $2p$, O $1s$, etc.). This technique can be used to identify the composition and electronic states present in the surface of samples. "LMM" and "KLL" labels refer to Auger electrons.

characterization of a sample. Transition metal L-edge experiments involve the excitation of a principal quantum number $n = 2$ shell electron (i.e., $2s$ or $2p$) absorbing an X-ray of specific wavelength and being promoted to unfilled d-orbital holes, giving insight into the valence of the elemental species in the material. The excitation of a $2s$ electron corresponds to the L_1 absorption edge and the s-orbitals have an orbital angular momentum, $l = 0$.

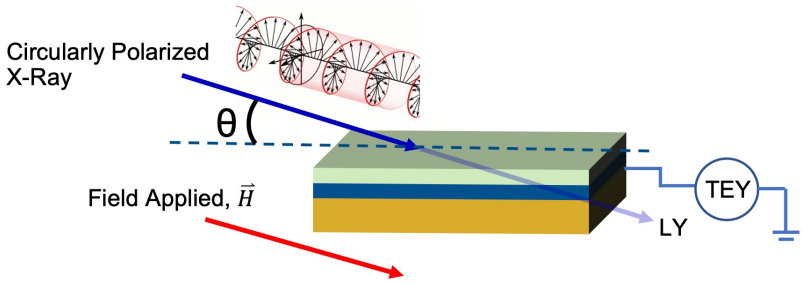

Figure 2.8: The experimental setup for XAS and XMCD. The circularly polarized X-ray is incident to the sample at some angle, θ and the magnetic field at ALS Beamline 6.3.1 is applied at the same angle using an electromagnet. LY and TEY modes are available, which probe the bulk and surface of the sample, respectively.

2.3.3 X-ray Magnetic Circular Dichroism

When an electron from the p-orbital absorbs an X-ray, its total angular momentum, j is equal to the sum of its orbital angular momentum, l, which, for the p-orbital $l = 1$, and its electron spin angular momentum, s, which can be equal to $+\frac{1}{2}$ for spin up electrons, or $-\frac{1}{2}$ for spin down electron giving rise to two possible values for j. This connection is referred to as "spin-orbit coupling" and gives rise to splitting of the L-absorption edges when an electron is excited from the $2p$ shell. The $2p_{1/2}$ (L_2-edge) transition is where the spin and orbital angular momenta are antiparallel $s = -\frac{1}{2}$ (so $j = 1 - \frac{1}{2}$) and the $2p_{3/2}$ (L_3-edge) transition where the spin and orbital angular momenta are parallel $s = +\frac{1}{2}$ (so $j = 1 + \frac{1}{2}$) [28]. An example L-edge XAS spectra is shown in the top panel of Figure 2.9b. When X-rays are circularly polarized, the electric field vector ($\overrightarrow{E}$) and magnetic field vector ($\overrightarrow{B}$ rotate in a helical pattern around the direction of propagation. This gives the X-rays a helical wavefront, which carries angular momentum. The X-rays can then impart this angular momentum to the orbital. If the X-ray helicity is parallel to the direction of X-ray propagation, it is said to be "right circularly polarized" (RCP), and conversely if the X-ray helicity is antiparallel to the direction of X-ray propagation, it is said to be "left circularly polarized" (LCP). As the

polarized X-ray interacts with the electrons, the photons impart their angular momentum to the electron which absorbs the photon, thus exciting the electron to an unoccupied d-shell orbital. In ferromagnetic materials, the population of spin-up electrons differs from the population of spin-down electrons in the valence d-shell, which gives rise to the preferred orientation of the magnetic dipoles in the material. Spin conservation prohibits spin flipping when the electron is excited into a higher state, meaning spin up electrons can only be excited into a spin up vacant orbitals. The difference in absorption spectra of LCP and RCP X-rays, is called X-ray magnetic circular dichroism (XMCD) and can be used for element-specific characterization of magnetic properties, such as magnetic ordering and magnetic moment.

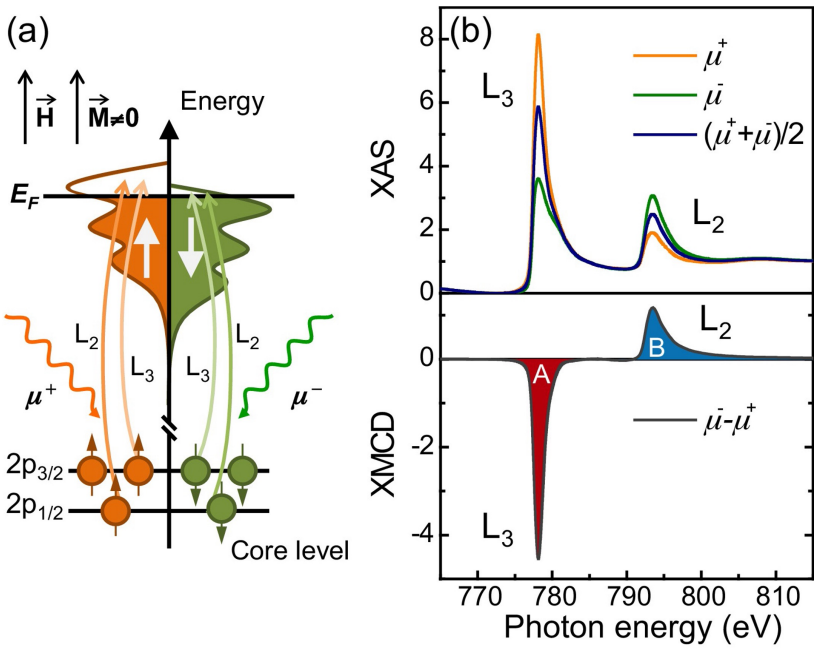

Figure 2.9: XMCD principle. (a) The vertical axis is the energy and the width is the density of states (DOS) or the probability that an electron will occupy a given state. Applying a field to a ferromagnetic material below its T_C will align the spins parallel to the field, and there will be a difference in X-ray absorption between LCP and RCP X-rays. (b) The top panel shows the XAS for RCP (μ^+), LCP (μ^-), and their average. The bottom panel shows the difference between $\mu^- - \mu^+$ which is the resulting XMCD effect [70].

When an XMCD signal is present, the X-ray can be tuned to the photon energy with the highest absolute value of intensity (usually the L_3-edge) and then monitor the magnetic signal while the applied magnetic field is swept from the two extreme values. In this manner, element-specific hysteresis loops can be generated which can give insight into the specific contribution of magnetic response from a given element.

2.4 Summary

This chapter described the synthesis and characterization methods of the thin films and bilayer samples that were studied in this thesis. The LSMO thin films and cobaltite bilayers that were grown using PLD and then annealed using the gas evolution chamber were characterized using X-ray techniques to determine their physical, electronic, and magnetic properties. Using these methods, a comparison can be made between the characterization results of the samples of this thesis and those of the samples grown and annealed using the same techniques in past studies.

Chapter 3

Results and Discussion

Using the methods described in Chapter 2, experiments were performed to answer the questions posed in Chapter 1. By growing and annealing manganite thin films, the results can be compared to the LCO and LSCO thin films grown and studied in past experiments. The cobaltite bilayer studies allowed for understanding how stacking order influences properties. This chapter describes the experiments in further detail and summarizes the results.

3.1 $La_{0.7}Sr_{0.3}MnO_{3-\delta}$ Thin Films

Four LSMO thin films were epitaxially grown on (001)-oriented LSAT substrates by PLD using a 248nm KrF excimer laser, a laser fluence of 0.8 J/cm^2, a substrate temperature of 700°C, 1 Hz repetition rate, and 300 mTorr of O_2. The samples were structurally characterized using XRR and XRD, and then annealed at the following temperatures and pressures for one hour:

900°C, 10^{-12} atm P_{O2}

600°C, 10^{-12} atm P_{O2}

400°C, 10^{-12} atm P_{O2}

400°C, 10^{-7} atm P_{O2}

The samples were again structurally characterized using XRR and XRD and then studied using XAS/XMCD spectroscopy to obtain and compare their magnetic characteristics. The of the structural characterization results are shown in Figures 3.1, and 3.2, the results of a study on phase-reversion behavior is shown in Figures 3.3 and 3.4 and the XAS/XMCD results are shown in Figure 3.5.

3.1.1 Structural Characterization Results

The structural properties were obtained using XRR and XRD performed on a Bruker D8 Discover diffractometer, and the data was analyzed using GenX (XRR) [68] and LEPTOS (XRD) [67] software. The top four diffractograms in Figure 3.1 were taken after annealing the samples and show the topotactic phase transformations compared to the as-grown (AG) sample. Note that the (002) peak position is zoomed in because the (002) peak is the most intense in perovskite single-crystal XRD. The change in peak positions and the number of peaks indicates that the samples have undergone topotactic phase transformation. In Figure 3.1 (a), for the as-grown (AG) sample at the bottom, three distinct peaks are observed that correspond to the perovskite phase. The film that was annealed at 400°C and 10^{-7} atm P_{O2} also showed the perovskite phase. Under closer observation near the (002) peak however, the film peak is observed to have shifted to lower 2θ, meaning that its out-of-plane lattice parameter has increased. A similar result is observed in the film that was annealed at 400°C, and 10^{-12} atm P_{O2}, but the film peak has shifted to an even lower value of 2θ values, indicating that the out-of-plane lattice parameter has increased more so. In

these two films the primary crystal structure is perovskite, however the formation of oxygen vacancies increased the lattice parameter and thus these two films are considered oxygen-deficient perovskite (OD-P). The film annealed at 600°C, and 10^{-12} atm P_{O2} begins to show additional "half-order" peaks which are indexed as the (002), (006), and (00 10) peaks of the BM phase. Finally, the film annealed at 900°C, and 10^{-12} atm P_{O2} shows a profile similar to the previous film, but with more pronounced half-order peaks, indicating that this film has also transformed into the BM phase.

In Figure 3.2, annealing also has the effect of increasing the roughness of the films seen as the steeper slope of the XRR curves after annealing, as well as a decrease in film density, seen in the increasing amplitude of the fringes and in the decrease in θ_c, and an increase in the thickness in the film observed by the increase in periodicity of the Kiessig fringes.

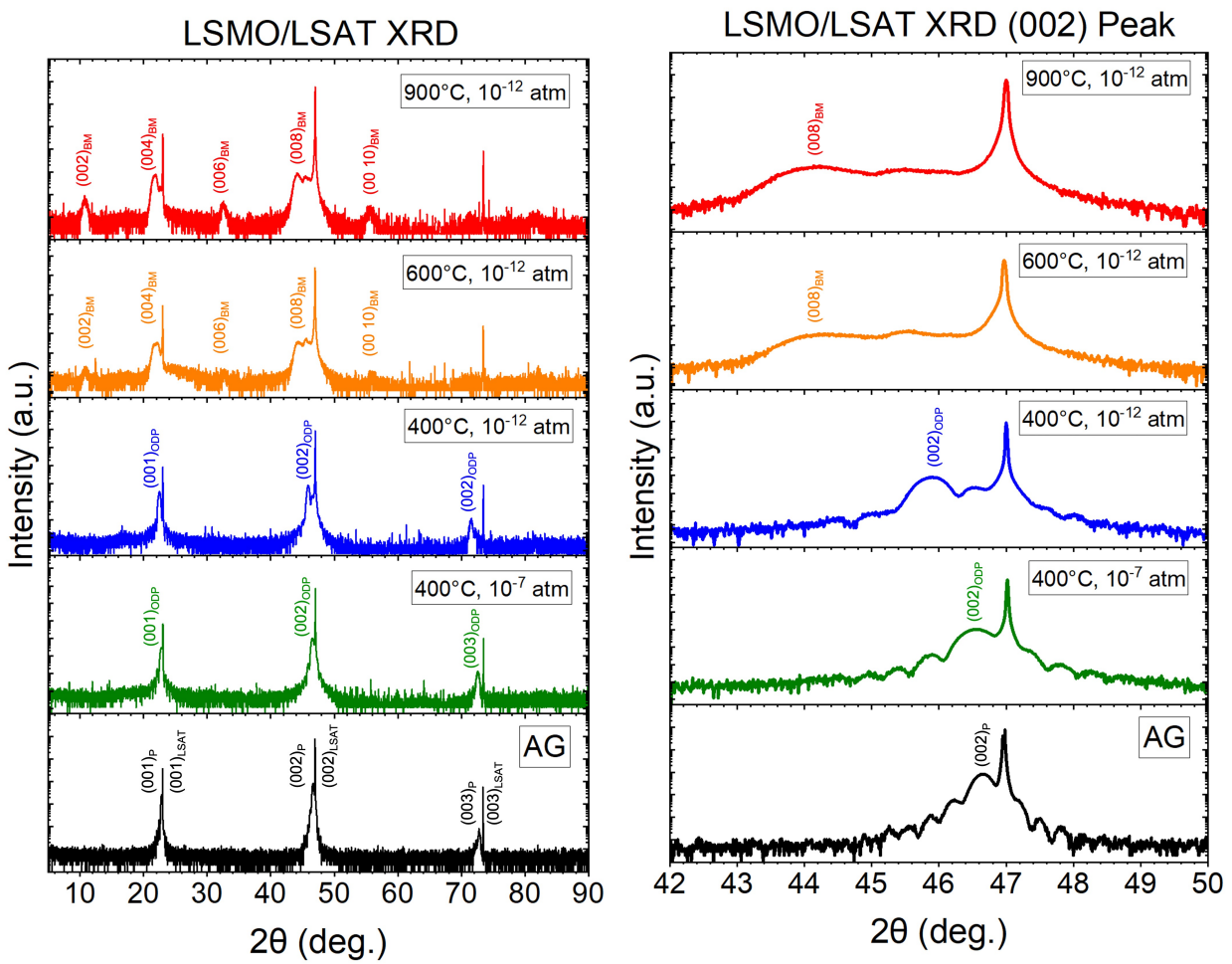

(a) (b)

Figure 3.1: (a) Full range XRD and (b) XRD close to the (002) film and substrate peaks of LSMO thin films exposed to various annealing conditions. The progression from the perovskite phase to ODP, to BM can be observed by the changes in peak position and by the appearance of the half-order peaks in between the main (perovskite) peaks in the BM samples.

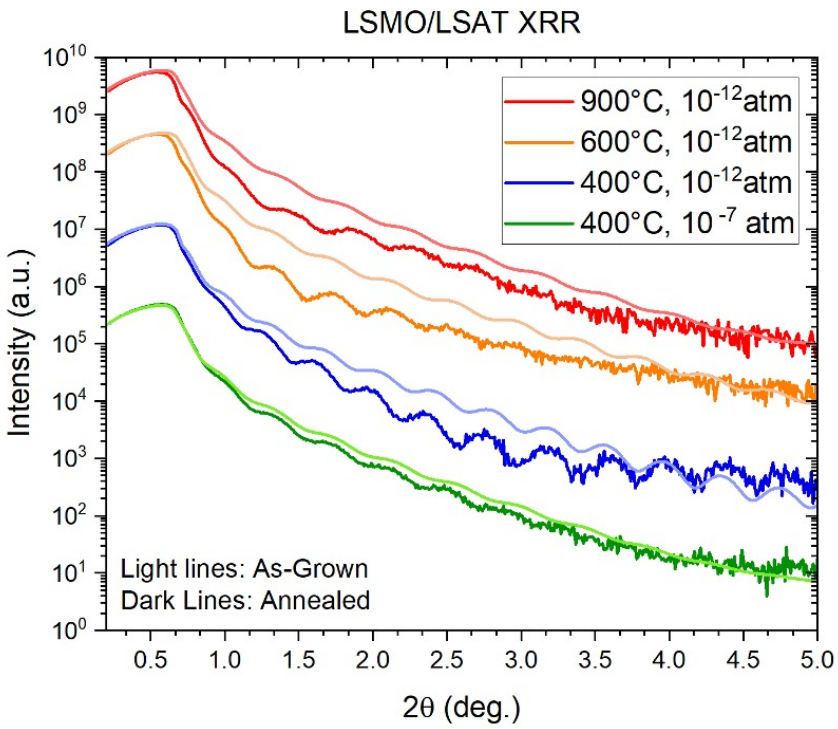

Figure 3.2: LSMO XRR curves showing both as-grown and annealed samples. The reduction in critical angle and slope indicates an increase in the surface roughness of the 600°C and 900°C annealed films.

The structural properties obtained from XRR and XRD are listed in Table 3.1. The films went an increase in out-of-plane lattice parameter and film thickness upon annealing. The column titled $n * c_P$ is obtained by equation 3.1 and corresponds to the factor by which the out-of-plane lattice parameter increases after annealing. This information can then be used with the values of expected increase in lattice parameter from Section 1.2 to determine the annealed phase(s) present. The film thickness also increases for each film where the largest increase is observed for the sample annealed at 900°C, and the smallest film thickness increase is observed for the sample annealed at the least reducing conditions, 400°C, and $10^{-7} atm$ P_{O2}. The critical angle is used as an indicator of the density of the films, where a higher

critical angle indicates a more dense film and a lower critical angle indicates a less dense film. These results are in agreement with past studies showing that perovskite thin films that are transformed by topotaxy to the BM phase generally increase in film thickness and decrease in density [59]. The %Δ values are obtained from Equation 3.2.

$$n * c_P = \frac{c_{annealed}}{c_{as-grown}} \tag{3.1}$$

$$\%\Delta = \frac{a_2 - a_1}{a_1} * 100\% \tag{3.2}$$

where, a_2 is the annealed value for film thickness or critical angle and a_1 is the as-grown value for film thickness or critical angle.

Table 3.1: LSMO structural property table showing both as-grown and annealed samples.

Annealing Cond. (°C)	Lattice Parameter, c (Å)		Annealed Phase	n*c_P	%Δ	Film Thickness (nm)		%Δ	Critical Angle (deg.)		%Δ
	As-grown	Annealed				As-grown	Annealed		As-grown	Annealed	
900	3.90	16.51	BM	4.2	323.8	20.00	21.48	7.4	0.58	0.54	-6.9
600	3.89	16.51	BM	4.2	323.9	21.60	22.79	5.5	0.59	0.54	-8.5
400	3.89	3.95	ODP	1.0	1.46	20.17	21.30	5.60	0.58	0.58	0.00
400*	3.89	3.90	ODP	1.0	0.03	19.06	19.67	3.20	0.58	0.58	0.00

* 10^{-7}atm P_{O2}

3.1.2 Phase Reversion

After the samples were annealed, they began to revert back to the perovskite phase by absorbing oxygen back into the crystal structure while being stored at room temperature which is observed by a shift in the XRD peaks back toward their as-grown value. Figures

3.3 and 3.4 show the diffraction patterns taken at the time of annealing and periodically afterwards in the following weeks and months. In all the samples, the peaks shift toward the as-grown state, but do not return completely over the duration of this study. The extent to which X-ray irradiation can cause phase reversion is not well-investigated in this thesis, although it is not likely that lab-based XRD has energy that is high enough to cause this change. There are several examples in the literature that showed X-ray irradiation affecting the oxygen vacancies in TiO_2 [71], as well as $LaAlO_3/SrTiO_3$ systems [72]. Further experiments with X-ray dose as a variable can be conducted to determine the effects of X-rays on the observed phase reversion.

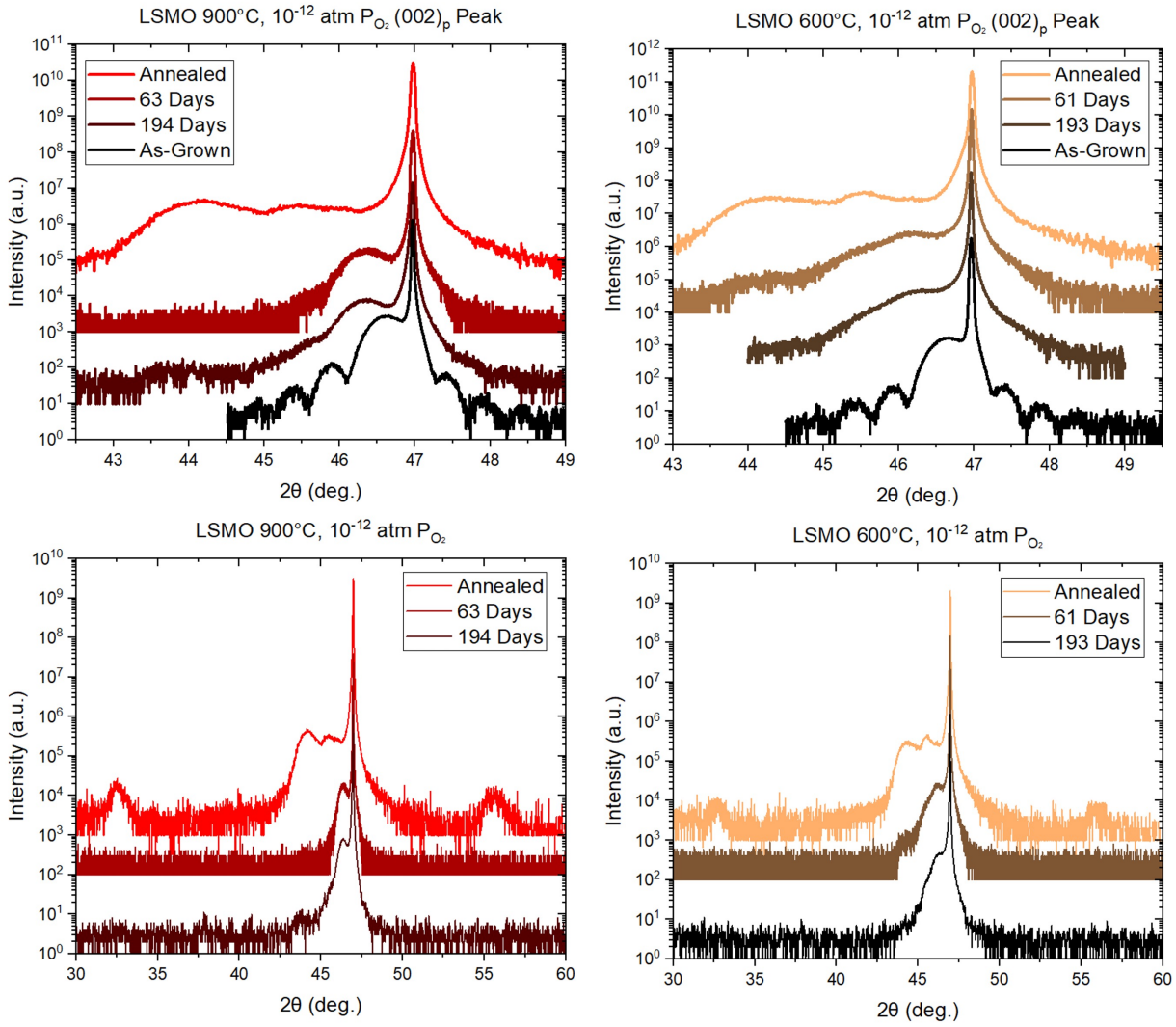

Figure 3.3: LSMO XRD curves showing the partial phase reversion after the samples were annealed and stored in a dry box. This figure shows two of the four samples, with the remaining samples shown on the next figure (Figure 3.4).

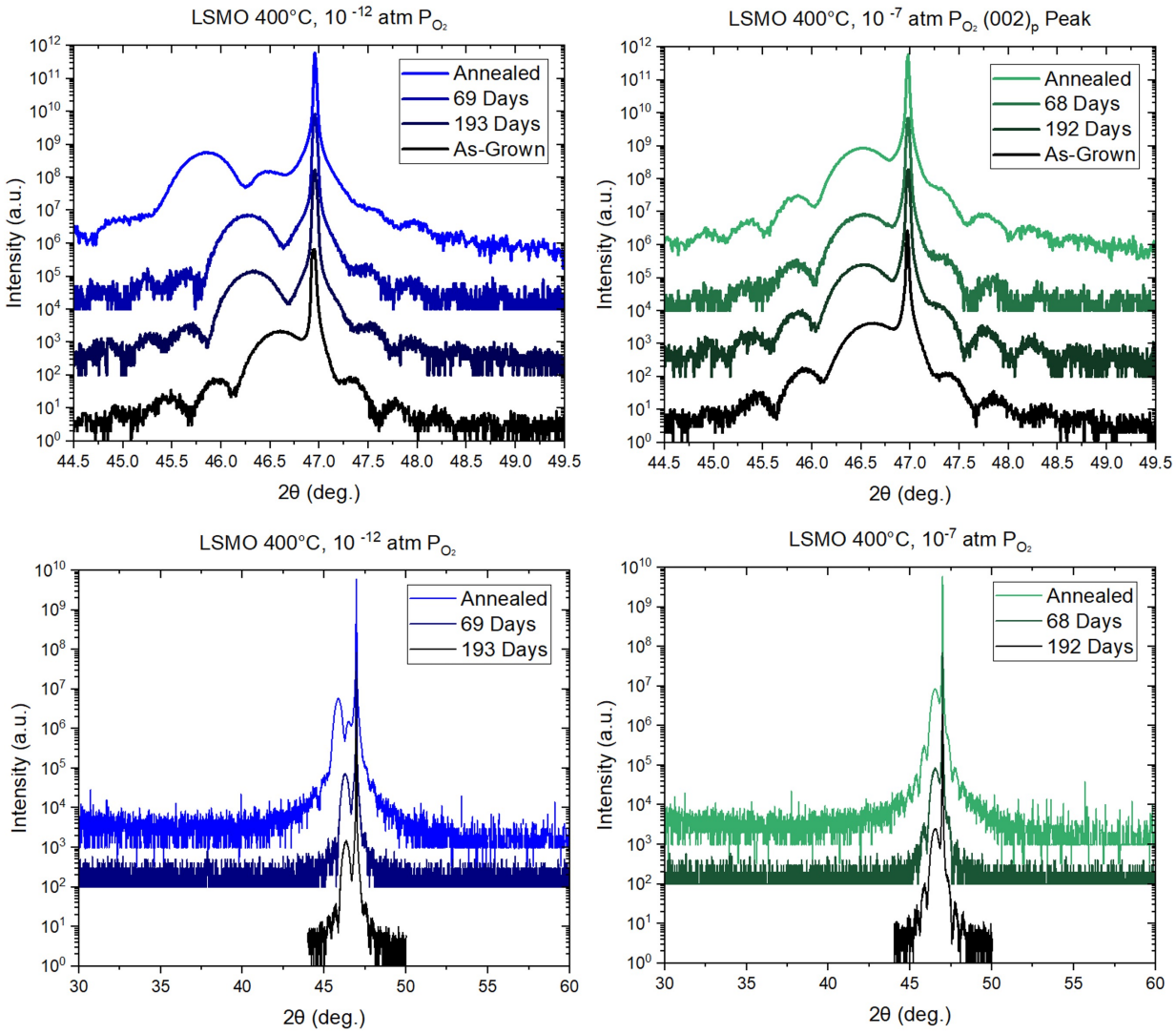

Figure 3.4: (continued from Figure 3.3) LSMO XRD curves showing the phase reversion after the samples were annealed and stored in a dry box.

3.1.3 Magnetic and Electronic Characterization Results

The XAS and XMCD data were collected at Beamline 6.3.1 at the Advanced Light Source, Lawrence Berkeley National Laboratory 11 to 17 days after annealing. The X-rays and magnetic field were at an angle of incidence of 30°, the sample temperature was 80K, and

the field strength selected was ±0.5T based on past studies [73] to ensure that the magnetic moments were fully saturated. In this experimental setup, rather than using RCP and LCP X-rays, only one polarization of X-ray was used and the magnetic field direction was flipped to collect the different spectra which were then subtracted from one another to obtain the XMCD signal.

Figure 3.5 plots the XA/XMCD spectra for the as-grown and annealed samples. The average manganese valence can be obtained by stoichiometric charge balance. The perovskite $La_{0.7}Sr_{0.3}MnO_3$ has an average Mn valence of $Mn^{3.3+}$, and the brownmillerite $La_{0.7}Sr_{0.3}MnO_{2.5}$ has an average valence of $Mn^{2.3+}$. The changes are very subtle in this system as a function of the annealing condition potentially because of the selection of the 600 line grating which gives higher flux instead of the 1200 line grating that would have given better energy resolution. Beginning with the as-grown state, a minor shoulder feature can be seen on the lower-energy sides at both the L_3- and L_2-edges following the vertical dashed line. As the samples are annealed under more reducing conditions, the shoulder becomes slightly more pronounced. The Mn-L_3 peak also shifted toward lower energy as the annealing temperature increased. As the oxidation state of Mn decreases at increasing annealing temperature, the effective charge on the Mn ion decreases, leading to a lower energy for the Mn-L_3 absorption peak.

The magnetic signal inferred from the XMCD spectra also does not change appreciably in shape, magnitude, or energy of the peaks. One possible explanation for this observation could be the competing magnetic sublattices on the octahedral and tetrahedral sites [74]. It should be noted that the reference data for the Mn^{2+}, Mn^{3+}, and Mn^{4+} spectra were collected at Beamline 4.0.2, which has better energy resolution than Beamline 6.3.1, where the XA/XMCD was collected for the films in this thesis. The XMCD hysteresis loop shown

in Figure 3.6 was collected at the Mn-L_3 edge and a similar conclusion can be drawn. The magnetization as a function of the field strength is very similar for all of the samples.

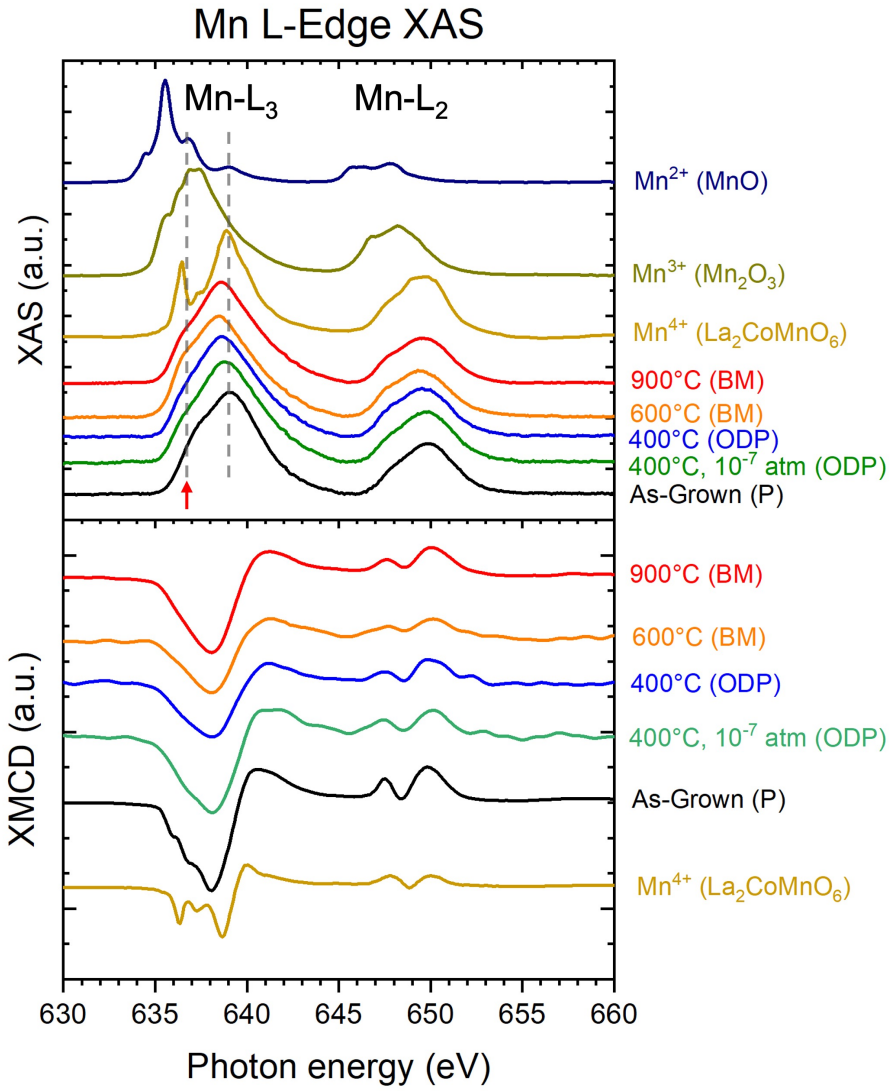

Figure 3.5: XA and XMCD spectra for LSMO thin films and reference spectra. The top panel shows the XA spectra near the Mn L-edge for the annealed and as-grown samples, as well as reference spectra for Mn^{2+}, Mn^{3+}, and Mn^{4+} (used with permission from Ref. [75]). The lower panel shows the XMCD spectra for the same samples and reference spectra for Mn^{4+} The vertical dashed lines in the top panel highlights the peak intensity features of the Mn^{4+} peaks. The broadening in the films' XA spectra is caused by the mixed valence states of Mn^{3+} and Mn^{4+}.

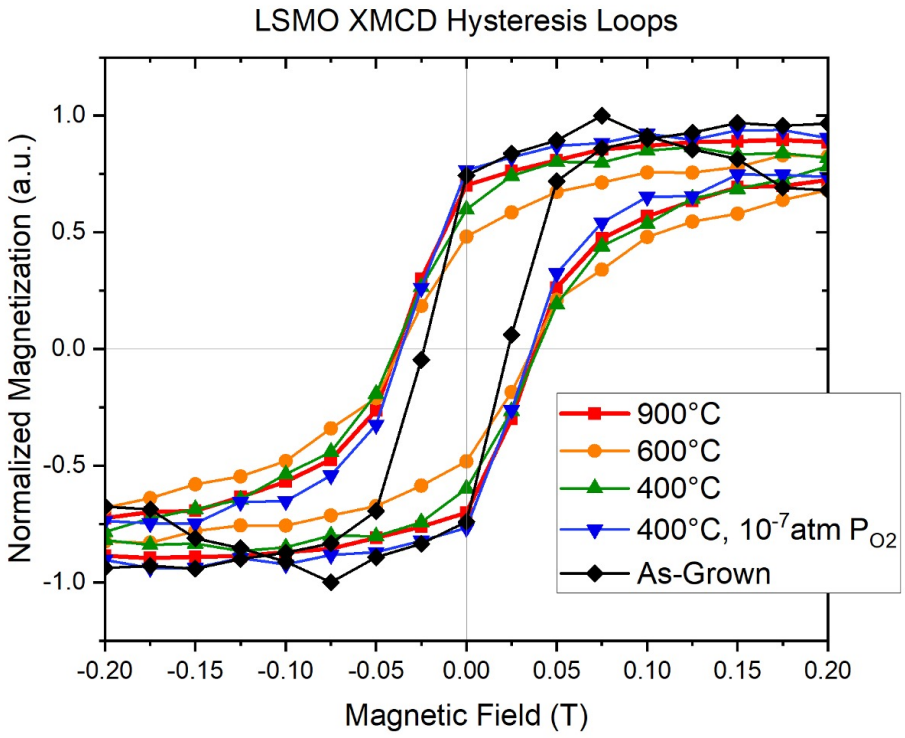

Figure 3.6: XMCD hysteresis loop taken at the Mn-L_3 edge for the as-grown, 400°C/10^{-7} atm P_{O2}, 400°C, 600°C, and 900°C LSMO thin films.

Oxygen K-edge spectra were also taken on the LSMO samples and these spectra are shown in Figure 3.7. It has been shown [76] that the peaks observed in O K-edge spectra can be assigned to the oxygen bonding to either B-site or A-site cations. The reduction in signal strength in the lowest energy peak as a function of the more reducing annealing condition indicates a reduction in valence of the manganese cation [77], which is consistent with expectations. The low-energy peak shows a minimum for the 600°C sample which may imply that the 900°C sample had begun to transform to a more reduced phase or that it had already began to revert back to the OD-P phase when the XAS measurements were performed.

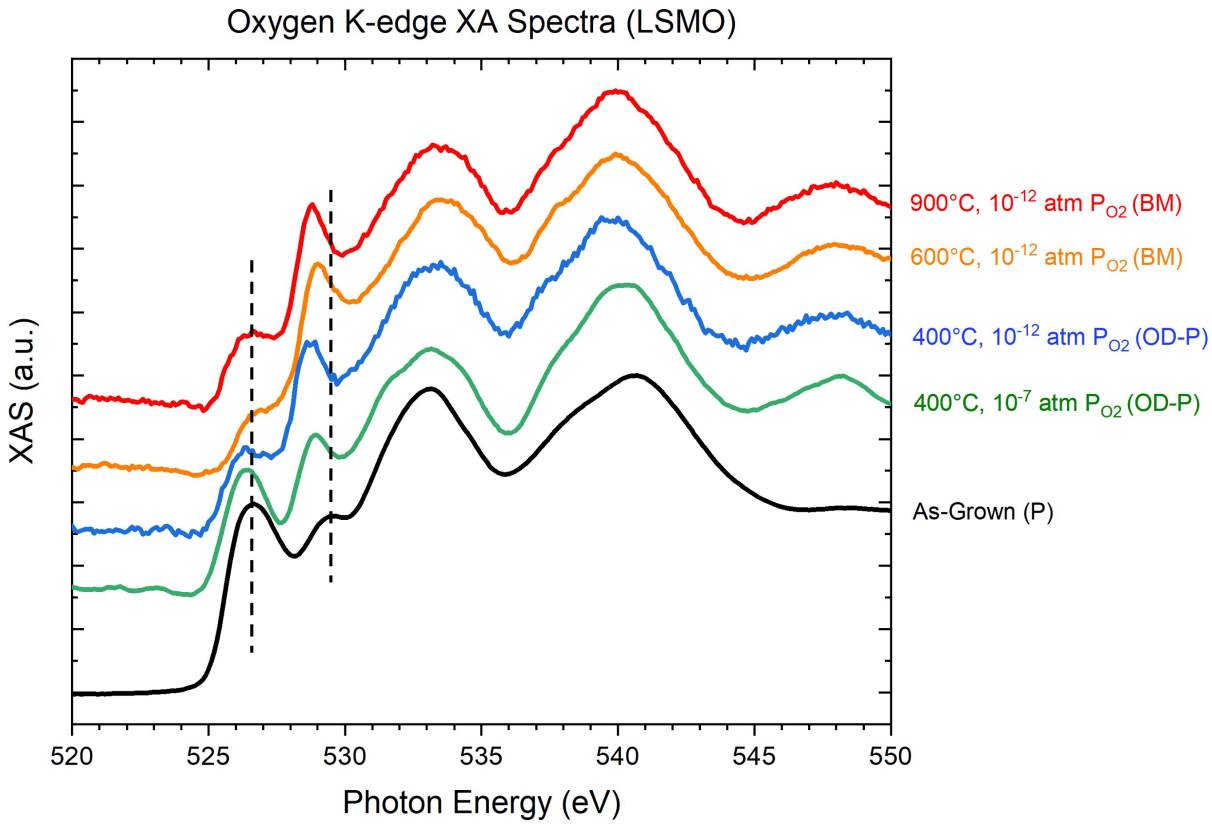

Figure 3.7: Oxygen K-edge XA spectra in TEY mode for the annealed LSMO thin films. The difference in the spectral shape arises, in part, from the oxidation state of the manganese cation in the structure. As described in the text, the reduction in signal strength in the low-energy peak marked by a dashed line as the annealing condition becomes more reducing is an indication that the valence of the manganese cation is decreasing.

3.1.4 Discussion

Beginning with perovskite LSMO thin films, the samples underwent topotactic phase transformation as confirmed by XRD, XRR, and XAS/XMCD studies. The only phases observed in this study were the ODP and BM phases. Although the Grenier phase of LSMO is rarely reported in the literature, it has been postulated and studied using density functional theory (DFT) [74], which suggests that Grenier phase LSMO may be stabilized (or metastabilized)

under certain synthesis or treatment conditions.

The O K-edge study shows that Mn L-edge XAS is not always adequate as a standalone measurement when investigating the change of valence that occurs with phase transitions. As seen in the comparison between the 600°C and 900°C O K-edge spectra, the high energy feature is less pronounced in the 600°C annealed sample. This could indicate that the 900°C annealed sample could have began to revert back to the OD-P phase, or that it had began to transform into a more reduced phase. Further investigation could determine whether another phase is accessible beyond brownmillerite by either increasing the annealing temperature, reducing the P_{O2}, or increasing the annealing duration.

Although the samples were stored in a room-temperature humidity-controlled dry box, they began to revert back to the perovskite phase over the course of weeks and months after annealing, as confirmed with XRD analysis. Future studies could involve finding a way to stabilize these materials to improve their shelf-life, such as using the application of an oxygen getter layer coating like Au and Gd similar to the technique used in Ref. [59].

Table 3.2: Summary of phases accessible by topotaxy in manganite thin films. All samples were deposited on (001)-oriented LSAT substrates using PLD and annealed for one hour at the conditions in the first column.

Annealing Condition (°C, atm P_{O2})	**Post-Annealing Phase**
900, 10^{-12}	BM
600, 10^{-12}	BM
400, 10^{-12}	ODP
400, 10^{-7}	ODP

3.2 $LaCoO_{3-\delta}/La_{0.7}Sr_{0.3}CoO_{3-\delta}$ Bilayers

For this stacking order of the cobaltites, a 15 nm layer of LSCO was deposited on (001)-oriented LSAT first, followed by a 15 nm layer of LCO on top, using the same deposition parameters as in the LSMO (see Section 3.1), and the samples were all structurally characterized using XRR and XRD. The samples were all annealed for one hour at the following conditions:

$$900°C,\ 10^{-12}\ \text{atm}\ P_{O2}$$
$$600°C,\ 10^{-12}\ \text{atm}\ P_{O2}$$
$$400°C,\ 10^{-12}\ \text{atm}\ P_{O2}$$

The samples were then structurally characterized again using XRD and XRR to observe their topotactic phase transformations in Figures 3.8 and 3.9. Using XAS and XMCD mea-

surements, the samples were magnetically characterized to observe the changes in magnetic properties that accompany the structural changes. The XAS and XMCD data are shown in Figure 3.11, and Figures 3.3 and 3.4 show the phase reversion behavior of the annealed LSMO films.

3.2.1 Structural Characterization Results

XRR and XRD data are shown in Figures 3.8 and 3.9 and values are listed in Table 3.5. The diffractogram of the 400°C sample shows a mixed phase of BM and GR. The GR phase has consistently wider peaks which indicates either it is a thinner film of the BM phase, or that the GR phase has more structural defects than the BM phase. The past study from Dr. Chiu showed that at these conditions, LCO thin films undergo topotactic phase transitions to produce a BM/GR mixed phase, and LSCO thin films with the same annealing conditions produce single phase BM films. Chapter 4 discusses future studies that could address these uncertainties. The difference in XRR data shows that after annealing, the sample roughness and the layer thickness increased, and the film density decreased. These observations are in agreement with Dr. Chiu's experiments on LCO and LSCO thin films [59].

The 600°C sample was another mixed phase, this time consisting of both BM and RP phases. Comparing the standalone thin films studied before, both the LCO and LSCO thin film systems showed an absence of diffraction peaks for the samples annealed at 600°C. Further experiments showed the presence of a polycrystalline RP phase with an additional Co nanoparticle precipitate. This result shows that the bilayer arrangement stabilizes the BM and RP mixed phase at 600°C for the LCO/LSCO bilayer system. The XRR shows an increase in surface roughness and layer thickness, and a decrease in layer density.

Lastly, the LCO/LSCO bilayer annealed at 900°C shows a single RP phase present after

annealing which is congruent with the past studies of the single layer thin films. However, LCO and LSCO in the RP phase are not expected to have the same out-of-plane lattice parameter. The wide film peaks indicate that the sample has an imperfect structural quality in comparison to the narrow as-grown sample film peaks. The XRR shows a substantial increase in roughness, an increase in the layer thickness, and a decrease in the layer density.

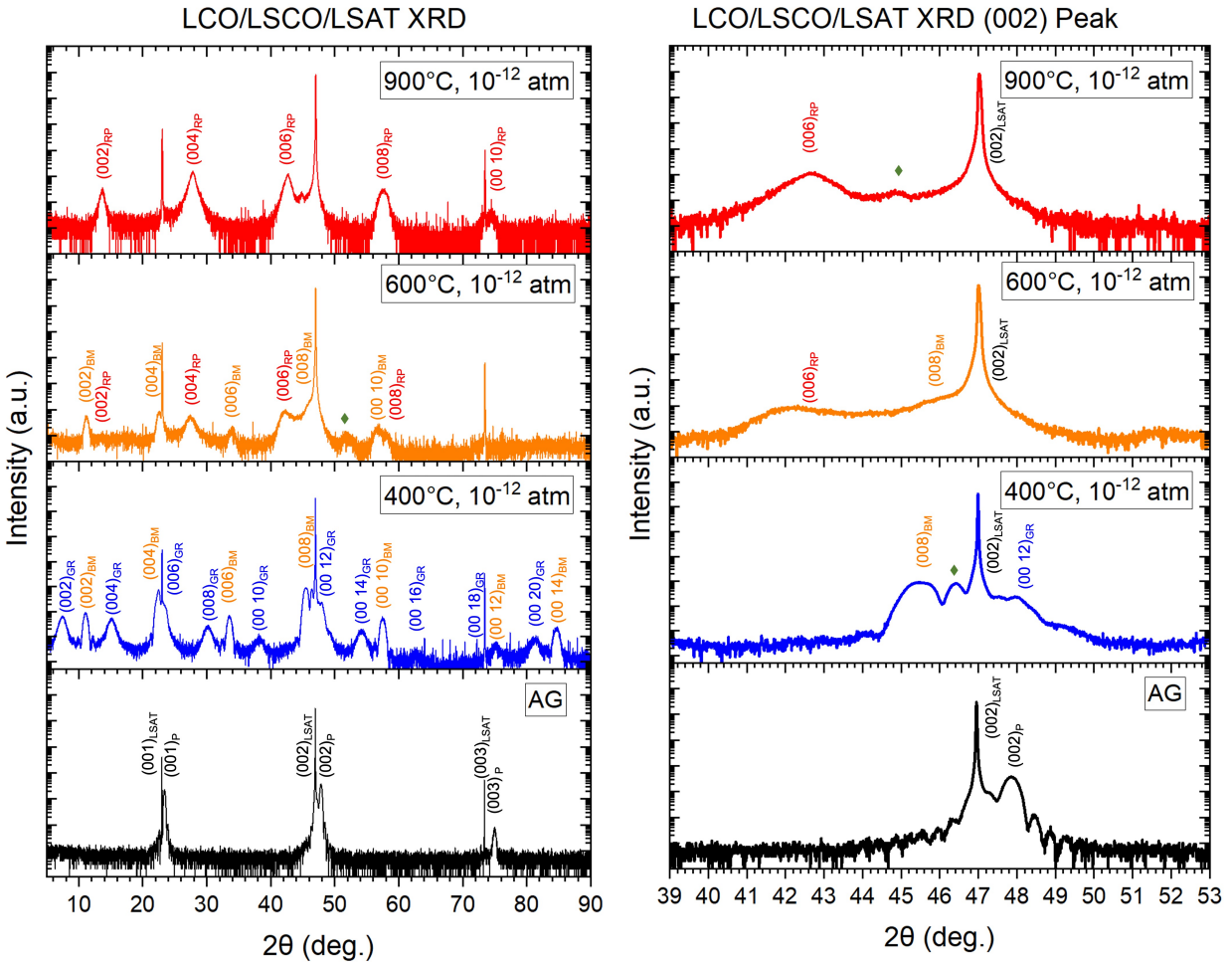

(a) (b)

Figure 3.8: (a) Full range XRD and (b) XRD of the (002) film and substrate peaks of the LCO/LSCO bilayers exposed to various annealing conditions. The diffractograms in (a) show the topotactic phase transitions that took place under the annealing conditions noted in the panels. The 900°C sample shows a strong signal for a single phase of RP. The 600°C sample shows a slightly weaker RP signal and an additional BM signal. The 400°C sample shows the presence of the GR and BM phases. In (b), the change in lattice parameter and peak shape indicates that the bilayers underwent topotactic phase transformations. The green ♦ symbols mark diffraction peaks from an unidentified phase that could not be indexed with the rest of the phases in the materials.

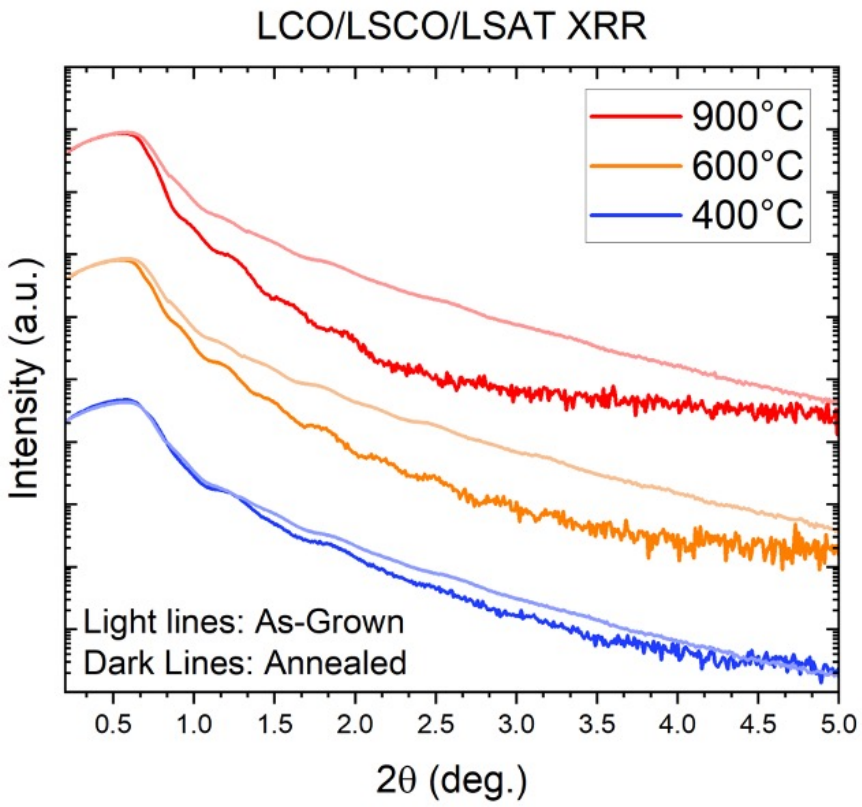

Figure 3.9: LCO/LSCO XRR curves showing both as-grown and annealed samples.

The structural properties in Table 3.5 were obtained from XRR and XRD. The increase in out-of-plane lattice parameter can be used to identify the phases present by determining the amount by which the lattice parameter increases. For example, $c_{RP} = 3 * c_P$, $c_{BM} = 4 * c_P$, and $c_{GR} = 6 * c_P$. Because the bilayers cannot be distinguished after the samples are annealed, $n * c_P$ and $\%\Delta$ values are given for both layers and for both phases present in the 600°C and 400°C samples. Similarly, the GenX fitting software was unable to resolve the two distinct layers in the data and still produce a fit using values for density, thickness and roughness that made physical sense. The bilayers are therefore tabulated as the "Total Film Thickness" which is the sum of both individual layers. The 900°C annealed sample underwent a decrease in film thickness and a decrease in film density, whereas the 600°C

and the 400°C samples underwent a film thickness increase accompanied with a film density decrease. These changes in total film thickness and a decrease in film density for each of the bilayer samples is in agreement with observations made in previous studies where RP phase films produced by topotaxy become thinner and decrease in density [59]. A comparison of the lattice parameters from the LCO/LSCO bilayer arrangement and the single layer films from Dr. Chiu's study are shown in Table 3.6.

Table 3.3: LCO/LSCO structural property table showing structural data of as-grown and annealed samples.

Annealing Cond. (°C)	Lattice Parameter, c (Å)			Phase	$n*c_P$		%Δ c	
	As-grown (LCO)	As-grown (LSCO)	Annealed		(LCO)	(LSCO)	(LCO)	(LSCO)
900	3.80	3.88	12.93	RP	3.4	3.3	240.1	233.5
600	3.80	3.88	12.91	RP	3.4	3.3	239.7	233.1
			15.50	BM	4.1	4.0	308.0	300.1
400	3.80	3.88	16.07	BM	4.2	4.1	323.0	314.8
			23.63	GR	6.2	6.1	521.7	509.7

Annealing Cond. (°C)	Total Film Thickness (nm)		%Δ	Critical Angle (deg.)		%Δ
	As-grown	Annealed		As-grown	Annealed	
900	23.88	23.11	-3.224	0.58	0.55	-5.17
600	24.52	25.08	2.284	0.58	0.54	-6.90
400	23.62	25.31	7.155	0.59	0.58	-1.69

3.2.2 Phase Reversion

Similar to the LSMO phase reversion study, after the LCO/LSCO samples were annealed, the oxygen-deficient structures began to revert back to the perovskite phase by reabsorbing oxygen back into the crystal structure. None of the samples show a complete phase reversion

back to the perovskite phase on the timescale of this study. Figure 3.10 show the diffraction patterns taken at the time of annealing and periodically afterwards in the following weeks and months. In all the samples, the peaks shift toward the as-grown state, but do not return completely over the duration of this study.

In the 400°C annealed sample, the GR peaks diminish completely, meaning that phase reverts to either BM or OD-P phase. It could also mean that the GR phase was in the layer that was more exposed to oxygen, i.e., the top layer (LCO) which is where the GR phase was observed in the single film studies [59].

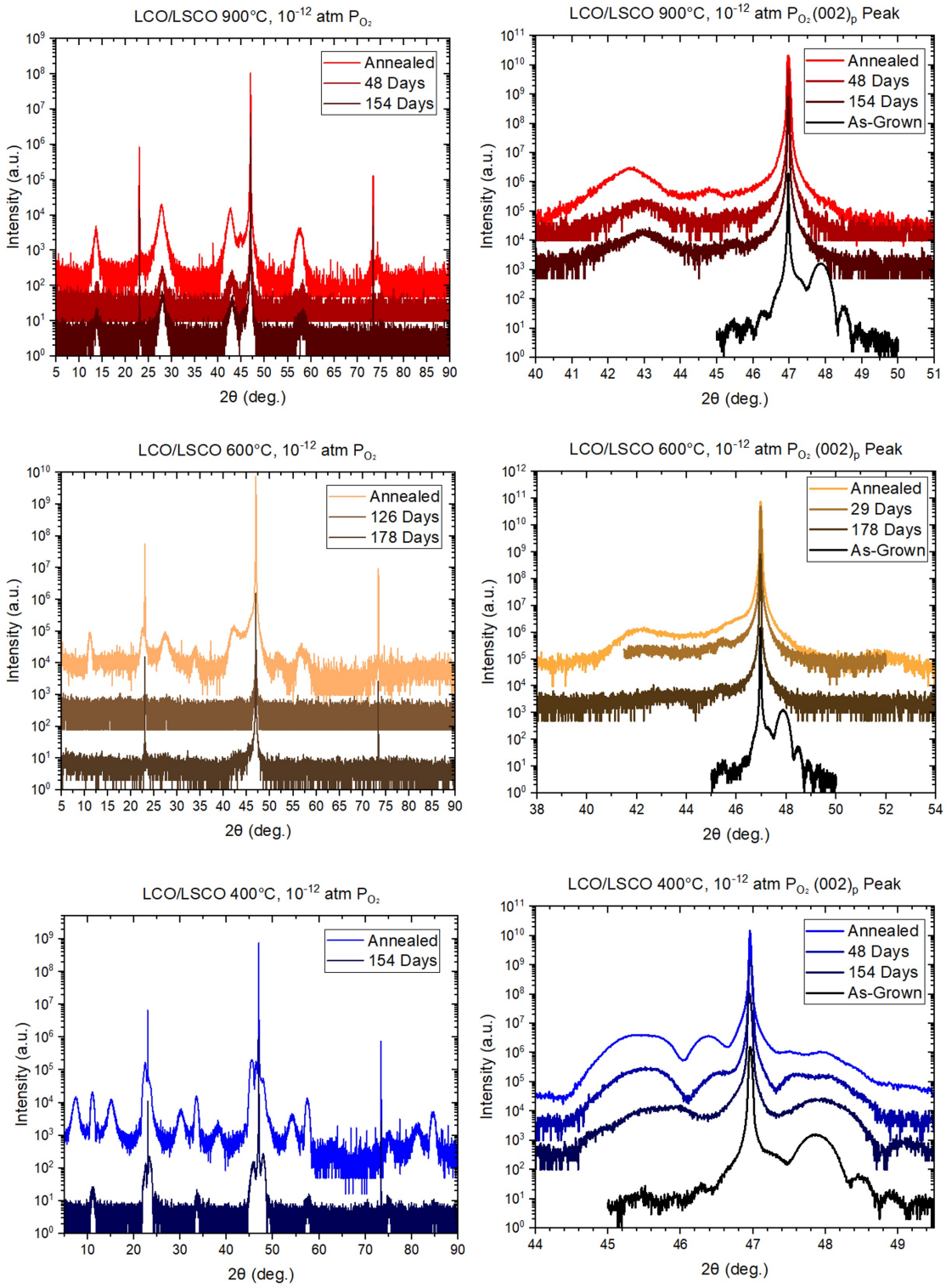

Figure 3.10: LCO/LSCO XRD curves showing the phase reversion after the samples were annealed and stored in a dry box.

3.2.3 LCO/LSCO Magnetic and Electronic Characterization Results

The XAS and XMCD spectra for the LCO/LSCO bilayer study were also collected at ALS with 30°grazing incidence, 80K sample temperature, and a magnetic field strength of ±1.93T was chosen based on past studies [27, 59] to fully saturate the magnetic moments in the material since LSCO is known to be a hard FM material [78]. The XA and XMCD spectra are shown in Figure 3.11, along with reference spectra for Co^{2+} ions (La_2CoMnO_6), Co^{3+} ions ($LaCoO_3$), mixed Co^{3+}/Co^{4+} ions (LSCO), and metallic cobalt.

The XA spectra are similar for the annealed samples in this sequence, with the most noticeable difference occurring between the 400°C and 600°C samples, where it begins to take on a spectral shape resembling the Co metal reference spectra. This observation could be interpreted as cobalt nanoparticles precipitating out of the crystal structure, which occurred in past studies of high-temperature anneals of LCO and LSCO [59]. This behavior is further predicted by the cation-deficiency that occurs with the transition to the RP phase. Lanthanum is most stable in the 3+ valence state, strontium is most stable in the 2+ valence state, and oxygen is most stable in the 2- valence state. By stoichiometric charge balance, cobalt in the perovskite phase of LCO and LSCO has average valence states of Co^{3+} and $Co^{3.3+}$, respectively and likewise, $Co^{2.34+}$ and $Co^{2.64+}$ in the Grenier phase, Co^{2+} and $Co^{2.3+}$ in the brownmillerite phase, and Co^{2+} and $Co^{2.6+}$ in the Ruddlesden-Popper phase. Additionally, cobalt is known to take on different spin states in complex oxides such as high-spin, low-spin, and intermediate-spin, however the spin-state of Co ions in LCO is still under debate [79]. The shift in the main peak position towards lower energies occurs as the bilayers are exposed to more reducing conditions, lowering the average valence of the cobalt.

The XMCD spectra that was calculated was all rather noisy and the cause for this obscuration

is unknown. The as-grown sample matches closely in signal peak position to both the LCO and LSCO reference spectra. Annealing at 400°C completely diminished the XMCD signal where the BM and GR phases were both observed by XRD, neither of which is ferromagnetic in the $LaCoO_x$ system [80], but no evidence was found in the literature for $La_{0.7}Sr_{0.3}CoO_x$ compositions. Annealing at 600°C and 900°C resulted in a clearer XMCD signal that again resembled the metallic cobalt reference spectra, though the signal is still small compared to the reference spectra.

The XMCD hysteresis loop shown in Figure 3.12 shows a dramatic difference in magnetization between the as-grown sample and the 600°C and 900°C samples. The 600°C and 900°C anealed samples have a much softer magnetic response compared to the as-grown sample which is consistent with the magnetic response of Co nanoparticles [81]. The as-grown bilayer has a hard magnetic signal compared to the two annealed samples, meaning it requires a stronger magnetic field to completely demagnetize the material. This property is known as coercivity. Also, when the magnetic field is removed, the material retains much of the magnetization which is a magnetic material property known as remanence. In the LCO/LSCO samples, the as grown bilayer has a higher coercivity, but a similar remanence.

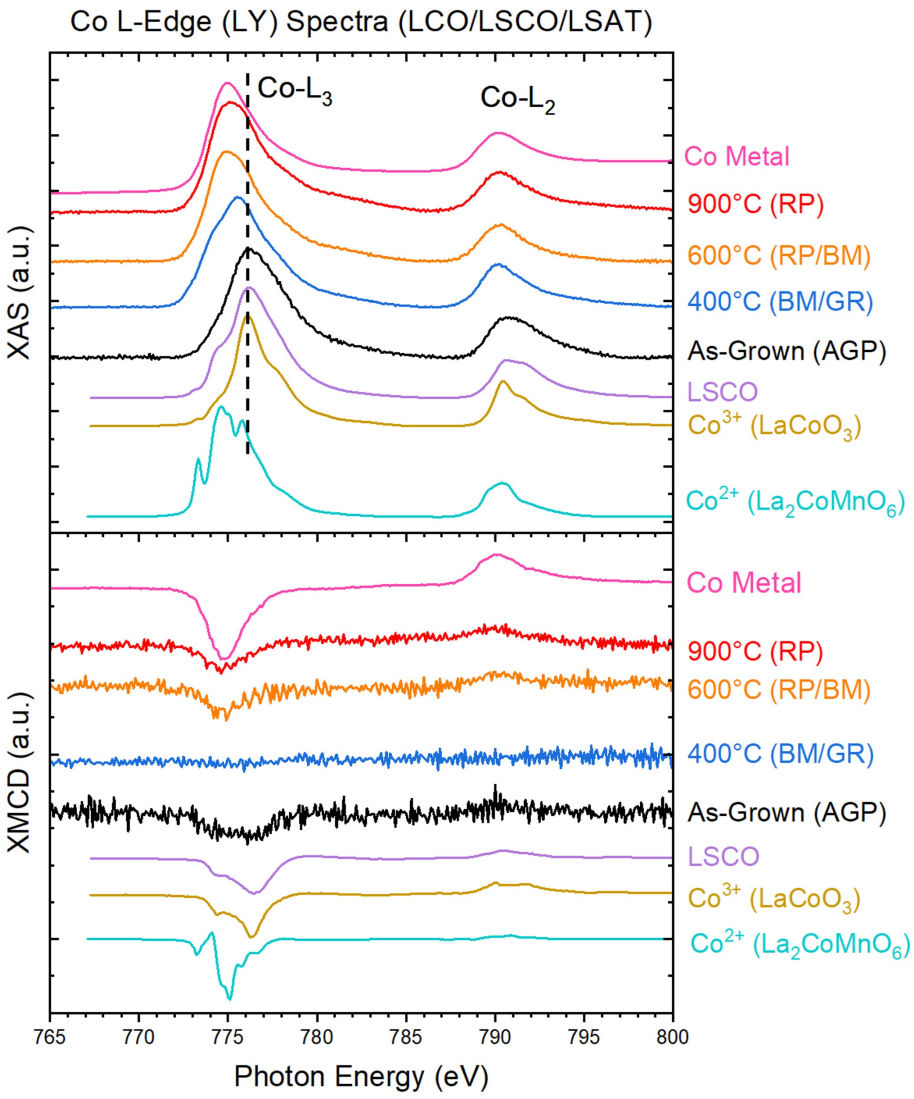

Figure 3.11: XAS and XMCD spectra for LCO/LSCO bilayer samples and reference spectra. The as-grown sample shows agreement with the LCO and LSCO reference spectra in both the XAS and XMCD signals. Annealing the bilayer system transforms the structure into a BM/GR mixed phase at 400°C, followed by RP/BM mixed phase at 600°C, and finally, RP single phase at 900°C. The XMCD signals show a slight ferromagnetic nature for the as-grown, 600°C, and 900°C samples, and no magnetic signal for the 400°C sample.

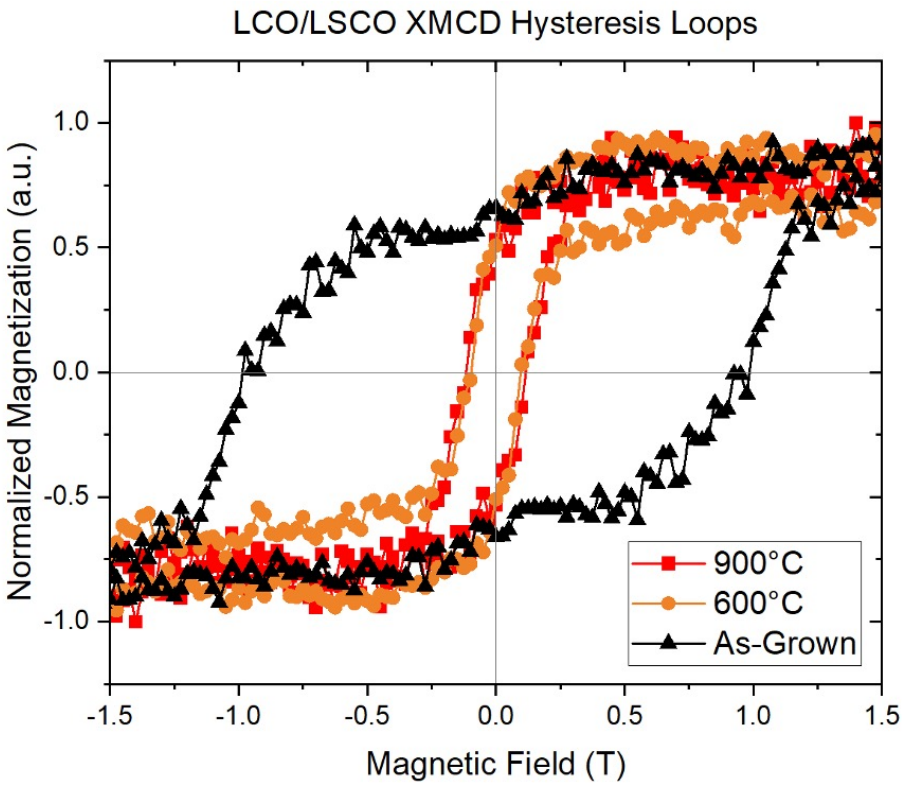

Figure 3.12: XMCD hysteresis loop taken at the Co-L_3 edge for the as-grown, 600°C, and 900°C LCO/LSCO bilayer samples.

3.2.4 Discussion

From the as-grown perovskite phase, the LCO/LSCO bilayer system underwent topotactic phase transformations under varying annealing conditions as confirmed by structural characterization via XRD. From the perovskite phase, the 400°C annealed bilayer showed a mixed phase of BM and GR phases. In the single layer studies, LCO also formed a mixed phase of BM/GR for the 600°C annealed sample, while LSCO single layer in past studies only formed BM phase. It is unable to be determined from the collected data which layer is mixed phase or if the layers are both single phase, one BM, one GR. However, the intensities and sharpness of the BM peaks in Figure 3.8a indicate that there is either more BM phase

present than GR phase, the GR film is thinner, or that the GR phase has more structural defects present than the BM phase. Further studies could extract this information using phase contrast TEM and/or electron diffraction.

The LCO/LSCO sample that was annealed at 600°C showed a notable difference from the single-layer cobaltite thin films annealed under the same conditions. In the previous study where individual films of LCO and LSCO were annealed and underwent topotactic phase transformations, Dr. Chiu had found that the samples were polycrystalline RP and cobalt nanoparticles. In the LCO/LSCO bilayer configuration, the crystallinity is maintained through the 600°C anneal, and clear peaks are identified as the BM and RP phase [59].

In the LCO/LSCO sample annealed at 900°C, the perovskite structure of both layers transformed into the RP phase. This result is in accord with expectations because in the past studies [59] involving the single layer films of LCO and LSCO individually, the RP phase was observed in both samples that were annealed at 900°C.

The electronic characterization showed that the bilayer system was in mixed valence states, as to be expected. The magnetic characterization results showed weak ferromagnetic signals for the as-grown, the 600°C, and the 900°C bilayers, and no magnetic signal for the 400°C sample. Comparing these findings with the past studies, the LCO showed a weak ferromagnetic signal for the as-grown, the 400°C, and the 900°C samples, and a large ferromagnetic signal for the 600°C sample, attributed to the cobalt nanoparticles that precipitated. For the LSCO study, a weak ferromagnetic signal was observed for the 400°C sample which had transformed into the BM phase, and no observable ferromagnetic signal in the 900°C sample which transformed into the RP phase. Similar to the LCO study, the 600°C LSCO thin film sample precipitated cobalt nanoparticles and which gave a large ferromagnetic signal. The

bilayer arrangement has shown to have the effect of stabilizing the BM/RP mixed phase at 600°C, and preserving the crystallinity of the sample.

As observed in the LSMO samples, the LCO/LSCO bilayer system was metastable for a period of weeks and months, however, the samples began to revert to a more oxidized state over time.

3.3 $La_{0.7}Sr_{0.3}CoO_{3-\delta}/LaCoO_{3-\delta}$ Bilayers

As mentioned in Section 3.2, the growth parameters of the bilayers was the same as for the LSMO thin films, and the only difference with this bilayer system was the stacking order. In the LSCO/LCO sample family, the LCO layer was deposited first, and then the LSCO layer was deposited on top of the LCO layer. The LSCO/LCO bilayers were annealed using identical annealing conditions as in the LCO/LSCO bilayer system. The structural characterization results using XRR and XRD are shown in Figures 3.13 and 3.14, data for the phase reversion study are shown in Figure 3.15 and the XAS and XMCD data are shown in Figure 3.16.

3.3.1 Structural Characterization Results

Beginning with the as-grown perovskite phase, the samples underwent annealing and subsequent topotactic phase transformations. At 400°C, the LSCO/LCO bilayer transformed to a mixed phase consisting of BM/GR phases. However in the LSCO/LCO stacking order, the peak intensity for both phases is more equal, indicating that there is a similar volume of BM to GR phase present in the LSCO/LCO bilayer compared to the more BM-rich 600°C annealed LCO/LSCO bilayer. Like the past mixed phase results, it is not possible to determine from these results which layer contributed to which phase(s). At 600°C, the sample

showed single BM phase. Finally, the 900°C sample transformed into the RP phase, again showing only one film peak even though both LCO and LSCO are present and their out-of-plane lattice parameters in the RP phase are not predicted to be equal. The film peak in the 900°C annealed sample has a much narrower film peak compared to the reverse stacking order which indicates that the 900°C annealed LSCO/LCO sample is of higher structural quality than that of the LCO/LSCO sample. The XRR data showed a decrease in density, and an increase in both film thickness and roughness, all to an apparent larger extent than seen in the LCO/LSCO bilayer system.

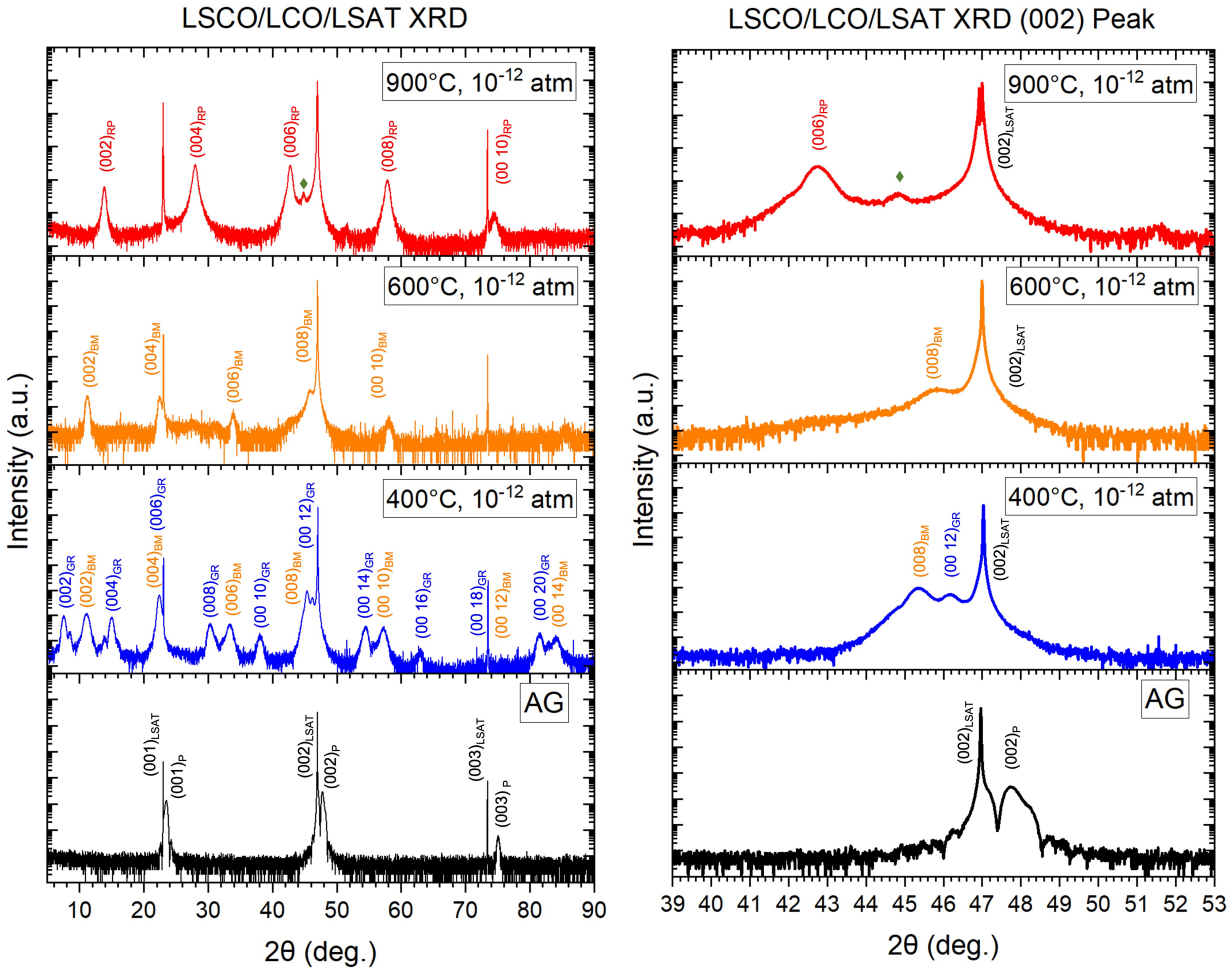

(a) (b)

Figure 3.13: (a) XRD and (b) XRR curves of LSCO/LCO bilayers under various annealing conditions. As the annealing temperature increases, the bilayers undergo topotactic phase transformations confirmed by XRD measurements. The 400°C sample takes on a mixed phase of BM/GR, the 600°C sample takes on a single BM phase, and the 900°C sample takes on the RP phase. As seen in the LCO/LSCO bilayer system, an unknown phase is present in the 900°C annealed sample and is marked with a green diamond symbol

.

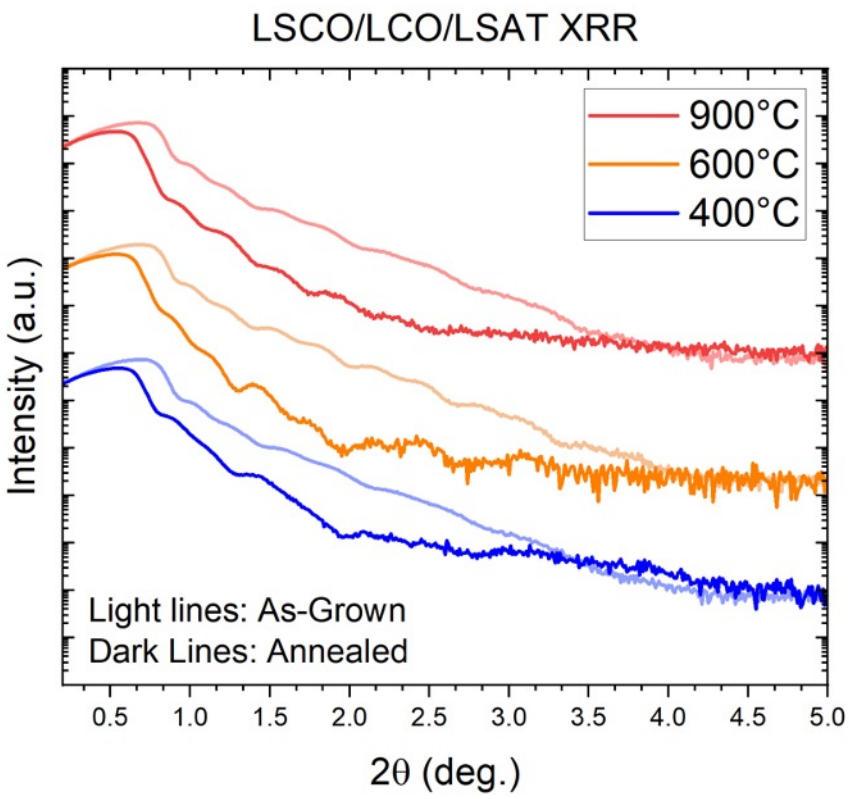

Figure 3.14: LSCO/LCO XRR curves showing both as-grown and annealed samples. As the samples are annealed, they generally become thicker, rougher, and less dense.

The structural properties in Table 3.4 were obtained from XRR and XRD. Like with the previous studies in this thesis, the increase in out-of-plane lattice parameter can be used to identify the phases present by determining the amount by which the lattice parameter increases. The bilayers in this stacking order also cannot be distinguished after the samples are annealed, so $n * c_P$ and $\%\Delta$ values are given for both layers and for both phases present in the 400°C sample using Equations 3.1 and 3.2, respectively. Again, the fitting software was unable to resolve the two distinct layers in the data and still produce a fit that made physical sense so the bilayers are tabulated as the "Total Film Thickness" which is the sum of both individual layers. The film thickness decrease observed was again observed in the

900°C sample, along with a decrease in the film density. Like in the previous bilayer stacking arrangement, the 600°C and the 400°C samples both increase in film thickness and decrease in density. A comparison of the lattice parameters from both bilayer arrangements and the single layer films from Dr. Chiu's study are shown in Table 3.6.

Table 3.4: LSCO/LCO structural property table showing both as-grown and annealed samples.

Annealing Cond. (°C)	Lattice Parameter, c (Å)			Phase	n*c_P		%Δ c	
	As-grown (LSCO)	As-grown (LCO)	Annealed		(LSCO)	(LCO)	(LSCO)	(LCO)
900	3.88	3.81	12.77	RP	3.3	3.4	229.5	235.2
600	3.88	3.81	15.81	BM	4.1	4.2	308.0	315.5
400	3.88	3.81	15.97	BM	4.1	4.2	312.2	319.6
			23.50	GR	6.1	6.2	506.5	517.3

Annealing Cond. (°C)	Total Film Thickness (nm)		%Δ	Critical Angle (deg.)		%Δ
	As-grown	Annealed		As-grown	Annealed	
900	24.94	23.54	-5.61	0.58	0.53	-8.62
600	24.55	27.31	11.24	0.57	0.55	-3.51
400	24.17	26.3	8.81	0.58	0.55	-5.17

3.3.2 Phase Reversion

Like the LSMO and LCO/LSCO samples, after the LSCO/LCO samples were annealed, the samples began to revert back to the perovskite phase as observed by their peaks shifting back toward their as-grown values. None of the samples show a complete phase reversion back to the perovskite phase on the timescale of this study. Figure 3.15 show the diffraction patterns taken at the time of annealing and periodically afterwards in the following weeks and months. In all the samples, the peaks shift toward the as-grown state, but do not return

completely over the duration of this study.

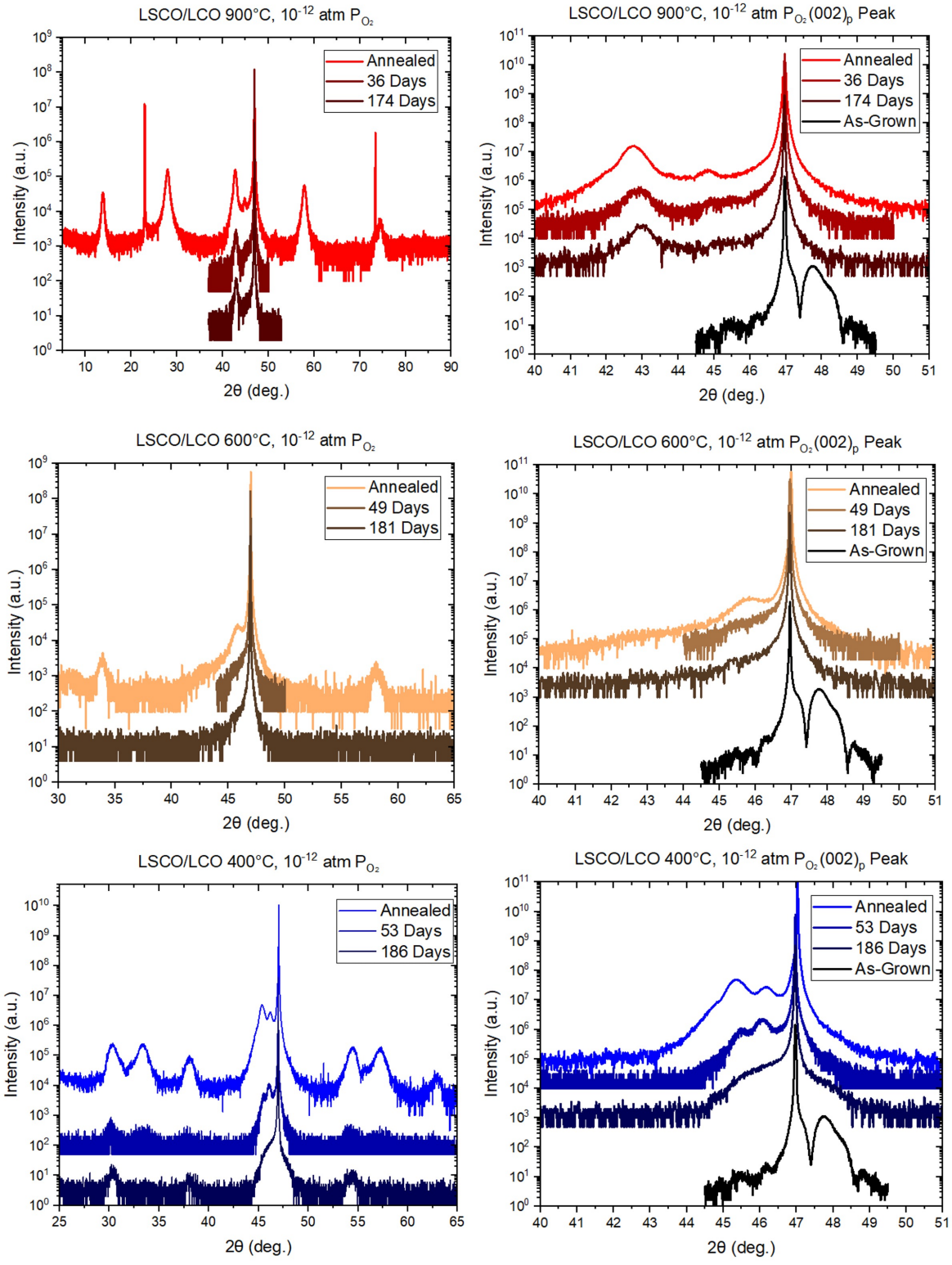

Figure 3.15: LSCO/LCO XRD curves showing the phase reversion after the samples were annealed and stored in a dry box.

3.3.3 LCO/LSCO Magnetic and Electronic Characterization Results

As with the LCO/LSCO bilayer system, the XAS and XMCD spectra for the LSCO/LCO bilayer study were also collected at ALS with 30°grazing incidence, 80K sample temperature, and a magnetic field of ±1.93T to ensure the magnetic moments were fully saturated [27, 59]. The spectra are shown in Figure 3.16, along with reference spectra.

The XAS shows similar spectral shapes for all the samples, with the shift in peaks toward lower energies arising from the decrease in valence. The 400°C sample shows a shoulder on the L_3-edge peak, possibly a contribution from the Co^{2+} ion spectral characteristic. This data aligns with the valence state by stoichiometric charge balance of $Co^{3.3+}$ and Co^{3+} for LSCO and LCO respectively in the perovskite phase, and $Co^{2.3+}$ and Co^{2+} for LSCO and LCO in the brownmillerite phase. That is to say, the population of Co^{2+} ions increases from the perovskite to BM topotactic phase transformation. Again, the 600°C and 900°C bilayers show a spectral shape that is similar to the metallic cobalt reference spectra which is as expected because of the cation precipitation from the RP phase.

The XMCD signals are again noisy here, possibly for the same reasons as proposed in Section 3.2.3. The as-grown bilayer shows a slightly ferromagnetic signal with a roughly similar shape as the LCO and LSCO reference spectra. As seen in the LCO/LSCO system, the 400°C annealed sample shows no XMCD signal. The ferromagnetic signal returns with the 600°C and 900°C samples, which roughly match the energy of the metallic cobalt XMCD signal, likely because of the presence of cobalt nanoparticles. This hypothesis could be confirmed with the use of electron energy loss spectroscopy (EELS) or transmission electron microscope (TEM) energy dispersive spectroscopy (EDS).

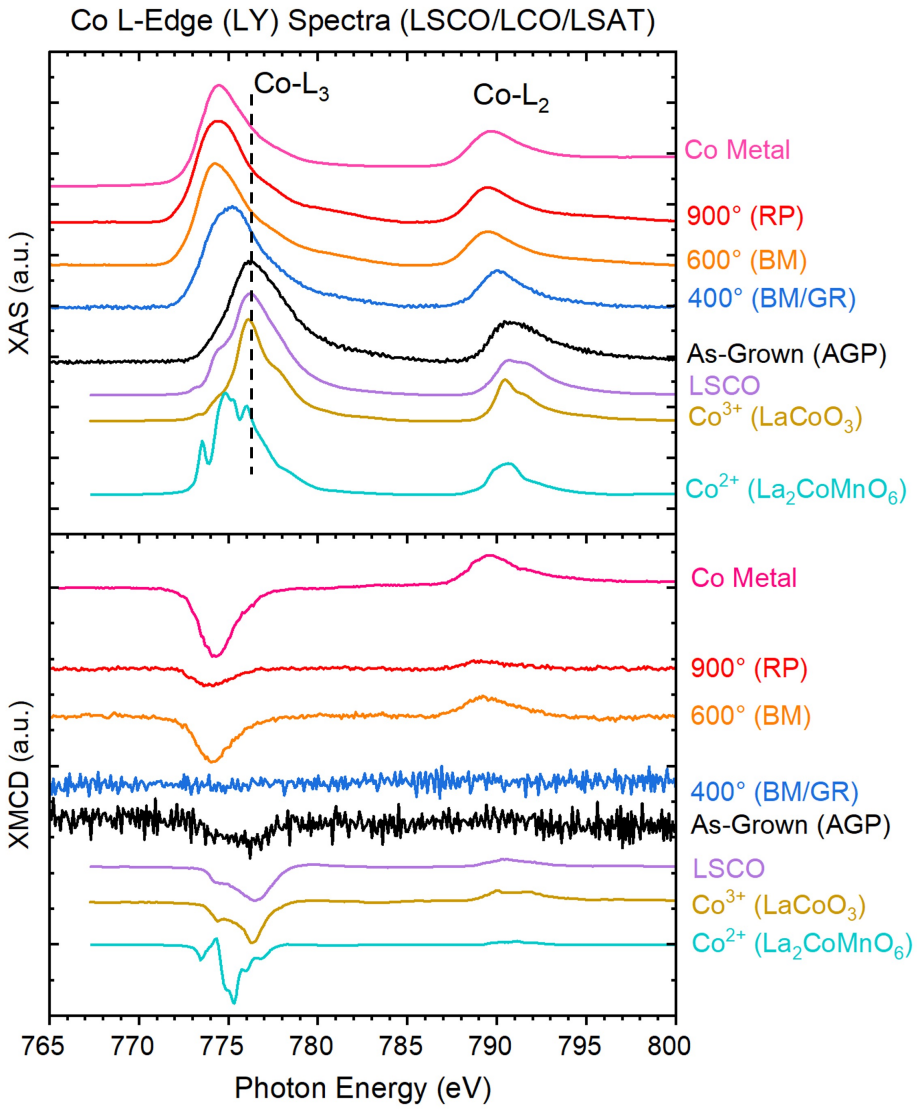

Figure 3.16: XAS and XMCD spectra for LSCO/LCO bilayer samples and reference spectra. The progression from as-grown to 900°C anneal shows a reduction in valence as seen by the peak shift to lower energies. The 400°C sample shows a slight shoulder at the lower energy side, possibly indicating an increase in Co^{2+} ion population. The 600°C and 900°C samples show a similar characteristic as the metallic cobalt reference spectra, pointing to the cobalt nanoparticles that could have precipitated out in the cation-deficient RP phase. The XMCD spectra show a ferromagnetic quality in the as-grown sample that disappears when annealed at 400°C, but returns under the 600°C and 900°C anneals. The reason for the return could also be because of the cobalt nanoparticle precipitate.

In the XMCD hysteresis loops shown in Figure 3.17, the three loops were taken at the Co-L_3 edge. The as-grown sample has a harder magnetic characteristic than the annealed samples due to its larger coercivity and the 600°C and 900°C annealed bilayers have a smaller coercivity.

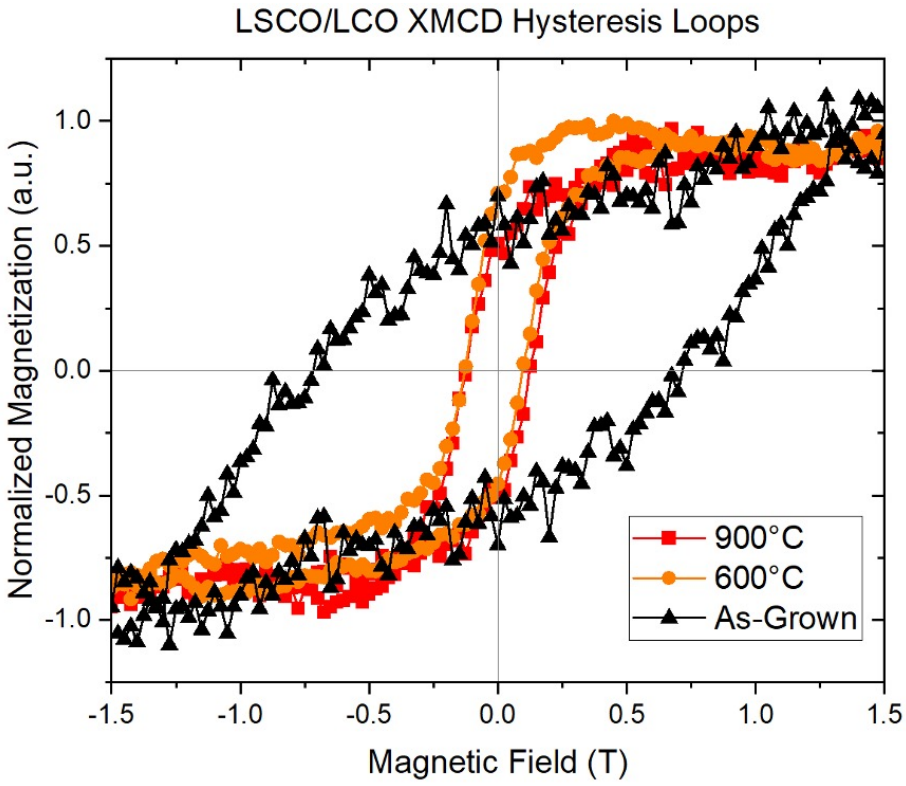

Figure 3.17: XMCD hysteresis loop taken at the Co-L_3 edge for the as-grown, 600°C, and 900°C LSCO/LCO bilayers.

3.4 Graded Layer Investigation

In the cobaltite bilayer samples, one of the constituent layers contains an amount of Sr (LSCO) where the other layer is Sr-free (LCO). Because of this difference in concentration, Fick's First Law suggests that the Sr *could* diffuse from the region of higher concentration

to the region of lower Sr concentration. To assess whether or not the inter-layer diffusion is occurring through the bilayer, XPS was used to determine the strontium concentration of the top layer of the following four samples all grown under the same growth parameters on LSAT substrates. Results from this investigation also showed that there were differences in the other electronic species present in the samples by comparing signals given by each sample in the individual scans for La 3d, Co 2p, Sr 3d, O 1s, and C 1s electron species.

LCO thin film

LSCO thin film

LCO/LSCO bilayer

LSCO/LCO bilayer

The expectation was that the LCO thin film and LCO/LSCO bilayer would not have a Sr signal in their XPS spectra, where the LSCO thin film and LSCO/LCO bilayer would have Sr present in the sampling depth of the XPS.

$$J = -D\frac{dC}{dz} \tag{3.3}$$

Equation 3.3 is Fick's First Law for one-dimensional diffusion where J is the diffusion flux, D is the diffusivity of the diffusing species, and $\frac{dC}{dz}$ is the z-direction concentration gradient of the diffusing species.

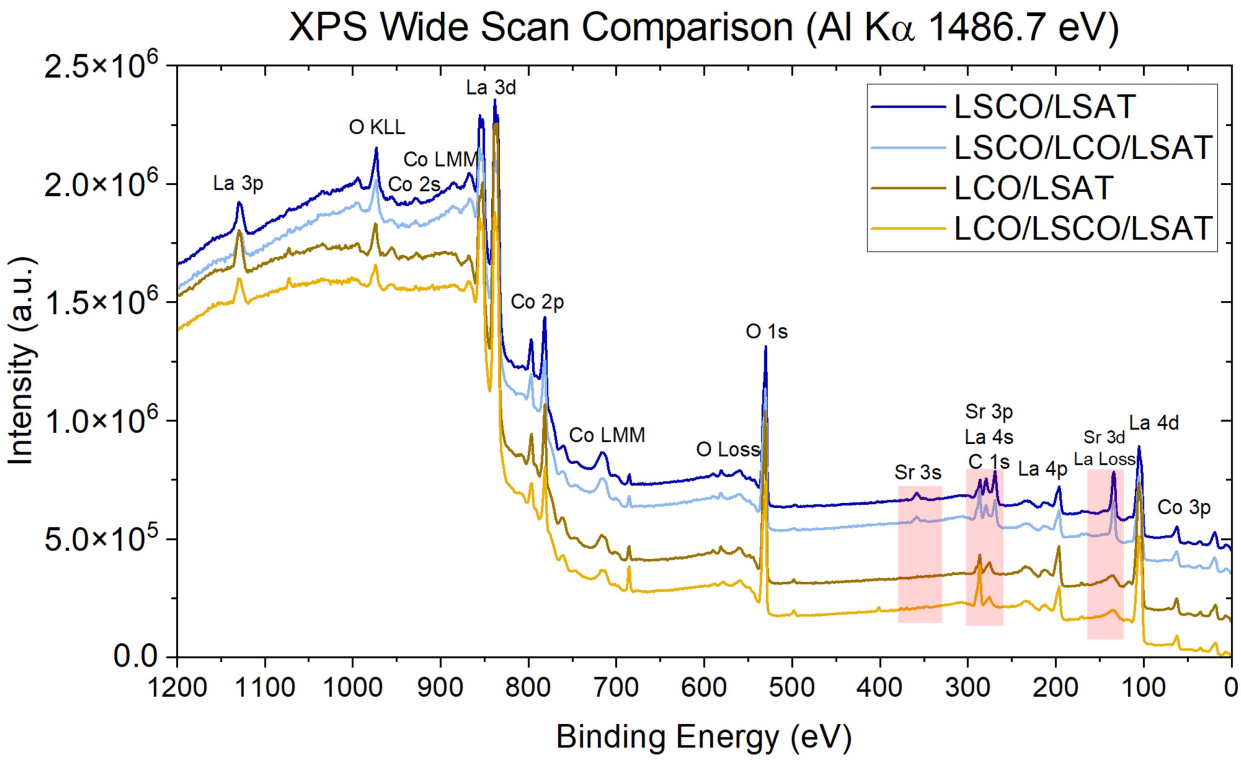

Figure 3.18: XPS wide spectra for cobaltite bilayers and single layers. The pink boxes highlight the absence of the strontium signal in the LCO thin film and LCO/LSCO bilayer system.

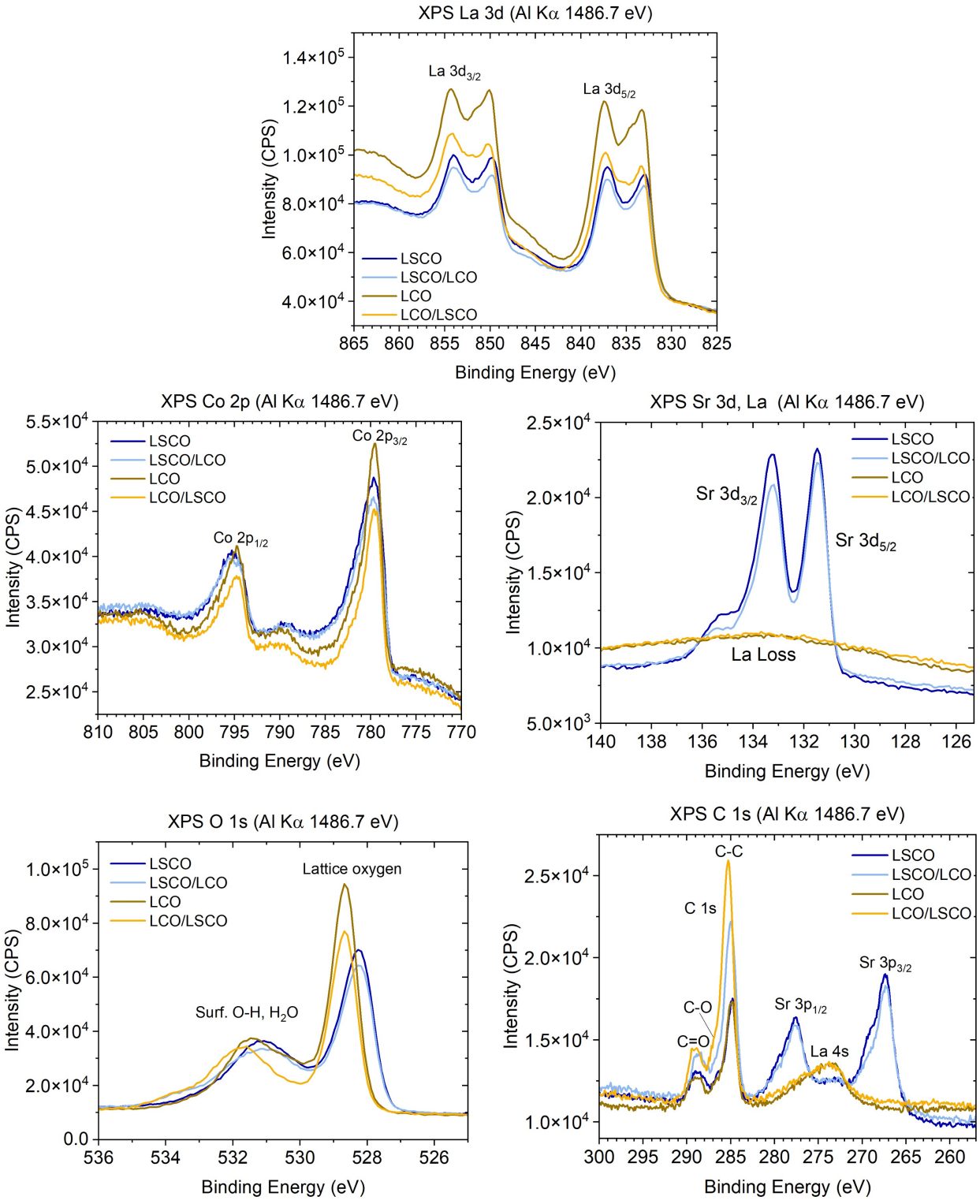

Figure 3.19: XPS spectra for selected electron species in cobaltite bilayers and single layers. No background correction or peak smoothing was performed.

Since XPS is a surface-sensitive technique, the presence of a strontium signal in the LCO thin film or LCO/LSCO bilayer would indicate that the strontium was diffusing from a lower layer or from the substrate. The wide scan XPS spectra are shown in Figure 3.18 and individual elemental species are shown in Figure 3.19. In the wide spectra, the pink highlighted boxes show the absence of strontium in the LCO thin film and LCO/LSCO bilayer. This is further illustrated in the individual elemental species scans, specifically the Sr 3d scan and the Sr 3p peaks within the C 1s scan. Cobalt, lanthanum, and oxygen electron systems are included to show that this technique is also sensitive to changes that may not be observable using the other instruments in this chapter. For example, a higher intensity in La 3d, Co 2p, and O 1s signals was observed in the LCO thin film sample and could have arisen from contamination existing on the three other samples even though all samples in this experiment were stored and cleaned with identical conditions. The Co 2p shows that the LCO and LCO/LSCO have a sharper peak, meaning that the cobalt valence is more homogeneous in the LCO and LCO/LSCO samples (only having Co^{3+} in the LCO) compared to the broadened signal seen in the LSCO and LSCO/LCO samples from the mixed valence of $Co^{3.3+}$ in the LSCO layers. The O 1s peaks are broader for the LSCO and LSCO/LCO samples, indicating a larger variety of oxygen species present in the lattice. Lastly, the C 1s peaks show the presence of contaminants on the sample surface. Sample handling was the same for all these samples, however, the bilayer samples were used in Beamline measurements, so the carbon tape used in those experiments potentially contributed to this difference in contamination levels.

The results of the XPS analysis revealed a distinction between the two bilayer configurations. In the case of LCO/LSCO/LSAT configuration, the absence of any detectable Sr signal in the XPS spectra indicated that the Sr did not migrate into the LCO from the LSCO layer during the deposition process. This observation suggests that the Sr cations remained confined within the LSCO layer. This study could be further reinforced by using angle resolved XPS

or by using XPS equipped with an ion mill for depth profiling to ablate the top surface and measure deeper into the sample.

3.5 Thin Film & Bilayer Comparison

In the single layer films studies performed by Dr. Chiu, the RP phase was observed in both LCO and LSCO films annealed at 900°C, with an additional unidentified phase in the LCO system. Similarly, both the LCO/LSCO and LSCO/LCO bilayer arrangements formed the RP phase when annealed at 900°C.

The single layer films annealed at 600°C both produced Co nanoparticles as well as a polycrystalline RP (pRP) phase in the LSCO film, however, in the bilayer samples, there was obvious crystal structure peaks that were indexed a mixed RP/BM phase in the LCO/LSCO system and a single phase BM phase in the LSCO/LCO system.

The 400°C annealing condition produced a mixed phase of BM/GR in the LCO film, and a single phase BM structure in the LSCO film. Both stacking orders of the bilayer system produced a BM/GR mixed phase.

Table 3.5 shows a comparison of the phases achieved by annealing the single layer thin films and the bilayers formed by stacking those single in the two different orders. The bilayer arrangements not only stabilize phases that are not accessible in either of the constituent single layer thin films, but also add a degree of freedom for tuning the behavior of the bilayer systems because the annealing conditions can lead to the formation of different phases depending on the stacking order. This detail can be used to design and fabricate bilayers with specifically tuned properties that arise in the phases produced by topotaxy.

Table 3.5: Summary of phases accessible by topotaxy in cobaltite bilayers compared to single layer thin films. The ♦ symbol represents the unidentified phase observed in Dr. Chiu's XRD experiments [59]. All samples were deposited on (001)-oriented LSAT substrates using PLD and annealed for one hour at the conditions in the first column.

Annealing Condition (°C, atm P_{O2})	**LCO** [59]	**LSCO** [59]	**LCO/LSCO**	**LSCO/LCO**
900, 10^{-12}	RP ♦	RP	RP	RP
600, 10^{-12}	NP	NP/pRP	RP/BM	BM
400, 10^{-12}	BM/GR	BM	BM/GR	BM/GR

Table 3.6 shows a comparison of the lattice parameters of the annealed bilayers in the two stacking orders, as well as the lattice parameters from the past annealed thin film studies using individual LCO and LSCO components. The values of the bilayer studies agree very well with those of the thin film study [59]. The LCO thin film in the RP phase had an out-of-plane lattice parameter of 12.78 Å, whereas the RP phase in the LSCO/LCO bilayer system had a value of 12.77 Å. The LSCO in RP phase had an out-of-plane lattice parameter of 12.89 Å, whereas the RP phase in the LCO/LSCO bilayer system appeared in both the 900°C and 600°C samples, and had values of 12.93 Å and 12.91 Å, respectively, which corresponds to a standard deviation of 0.07 Å.

The out-of-plane lattice values for in the other bilayer and thin films had lattice parameters with a standard deviation of 0.07 and 0.22 Å, for the GR and BM phases, respectively.

Comparing the lattice parameters of the 600°C bilayers to the BM phase in the 400°C bilayers and thin films, those from the 600°C bilayers are lower.

Table 3.6: Lattice parameter comparison of the two different stacking orders of the bilayer systems, as well as the constituent thin films annealed under the same conditions from Ref. [59].

Annealing Cond. (°C)	Annealed Lattice Parameter, c (Å) and Phase(s) Present							
	LCO		LSCO		LCO/LSCO		LSCO/LCO	
900	12.78	RP	12.89	RP	12.93	RP	12.77	RP
600	N/A	NP	N/A	NP/pRP	12.91	RP	15.81	BM
					15.50	BM		
400	16.06	BM	16.05	BM	16.07	BM	15.97	BM
	23.60	GR			23.63	GR	23.50	GR

3.6 Summary

This chapter showed and discussed the results of experimentation using the instruments described in Chapter 2. The LSCO/LCO bilayer system behaved similar to the LCO/LSCO bilayer system with a few key differences. In all annealing conditions the bilayers underwent topotactic phase transformations which was observed by XRD. Beginning with the 400°C sample, the perovskite bilayer transformed into a mixed BM/GR phase. One difference between the two bilayer systems was that the LSCO/LCO bilayer system showed a single BM phase at 600°C, where the LCO/LSCO bilayer system showed a mixed phase. Finally, the 900°C sample showed a single RP phase.

The electronic characterization showed that as the annealing condition increased, the valence state of the cobalt ions in the bilayers decreased, which also supports the topotactic phase

transformations observed by XRD. The magnetic study showed that the as-grown bilayer had a weak ferromagnetic signal, which diminished completely upon annealing at 400°C, then returned with the 600°C and 900°C anneals. Comparing this data to the prior study conducted on the single films, the 400°C LCO sample showed a near nonexistent ferromagnetic signal by XMCD, the 600°C sample showed a strong ferromagnetic signal which diminished with the 900°C sample. In the LSCO study, the as-grown sample showed a ferromagnetic signal that decreased under the 400°C BM phase, became strong again under the 600°C polycrystalline RP/cobalt nanoparticle mixed phase, then diminished again in the 900°C RP phase.

The graded layer investigation showed that the top layer (probe depth of XPS) of the LCO/LSCO bilayer system did not contain any strontium. This study is not appropriate to conclude whether or not the strontium from LSCO is diffusing down into the LCO in the LSCO/LCO bilayer system. Further studies could involve resonant X-ray reflectivity to determine the depth profile of the strontium in these bilayers. Alternatively, using the ion mill equipped on the XPS would be a destructive technique that could show the depth profiles of all ions in the film.

Chapter 4

Conclusions

This thesis showed that the LSMO perovskite system behaves differently from the past studies of similar thin films consisting of first row transition metal cations including the LCO and LSCO single layer thin films [59]. This results comes at no surprise since the B-site cation has already been observed to affect the stability and kinetics of different phases leading to different topotactic phase transformations being present for the same annealing condition [59]. The bilayer cobaltite system study illustrated two key findings: 1) growing two films on top of one another changes the chemistry and mechanics of the crystal structure in such a way that annealing them produces results that are different from their equivalent single layer thin film arrangements, and 2) the stacking order plays a role in changing the chemistry and mechanical properties of the system and changes the resulting phase after annealing at a given temperature. Changing the order of a bilayer stack essentially produces a distinct material with different topotactic behaviors from another stack arrangement.

The temperature, pressure, composition, and stacking order are factors that impact the

topotactic phase transformations observed in perovskite thin films and bilayers in this thesis. Other factors could include film thickness, degree and state of epitaxial strain, and the A-site cation and dopant selection and concentration. All of these experimental variables can be used to study their effect on topotactic phase transformation in epitaxial perovskite oxides.

4.1 Future Work

There are several limitations of the work in this thesis that should be addressed in future related studies. Since there was only one instance of a particular sample that was annealed at a certain condition, a big question of the repeatability of these experiments still exists. Future studies should include duplicate samples to ensure that the topotactic phase transformations can be reproduced in another occurrence to eliminate factors of chance from the resulting conclusions. The metastability of the consequent phases produced can also be systematically studied by performing analyses at timed intervals similar to another study by Dr. Chiu [59]. By determining the "shelf-life" of the post-annealed samples, future studies on similar materials can have a more defined experimental timeline where results will be the most accurate to a particular structure that was produced by topotaxy. This study could also involve researching the conditions that drive the oxygen-deficient phases back to the perovskite phase most completely so that a switching profile can be quantified. Lastly, the homogeneity of the phases produced in both the thin film study and the bilayer studies was left unquantified. The question remains whether or not the thin films and individual layers were all one phase or not and this could be addressed in future studies.

To help determine the extent of concentration gradient in future bilayer studies, Rutherford backscattering spectrometry (RBS) is a quantitative analysis technique that could be used to determine the depth profile of elements present in the sample [26]. With the use of a

heating stage or temperature controlled chamber, this experiment could also be done *in situ* to more closely observe the B-site cation and oxygen anion migration kinetics during topotactic phase transformations.

The XRD experiments performed in this thesis were all done *ex situ*, however a more complete insight into the topotactic phase transformation would be possible with *in situ* XRD and XPS [82] to observe any intermediate phases [26]. Using this tool in addition to differential scanning calorimetry (DSC) [83] could show more exact conditions leading to the topotactic phase transformations observed which could allow for a closer study of the kinetics involved and it could inform the role of annealing duration on topotactic phase transformations, which was not well-explored in this thesis. *In situ* high-resolution TEM experiments [84] have allowed for the direct observation of topotactic phase transformations in perovskite oxides and could also be used for precisely measuring the atomic positions as the structure changes [15].

To help determine the role of epitaxial strain in the topotactic phase transformations observed, the selection of different substrates could be used as an experimental variable. By choosing a substrate with a larger lattice parameter than LSAT, such as $SrTiO_3$ (STO), the LCO/LSCO bilayer system will be in even more tensile strain, and the LSMO will be in tensile strain rather than compressive strain when using LSAT as the substrate. As shown in Figure 4.1, a number of perovskite-compatible substrates exist which allows for a systematic study of how strain influences the topotactic phase transformations.

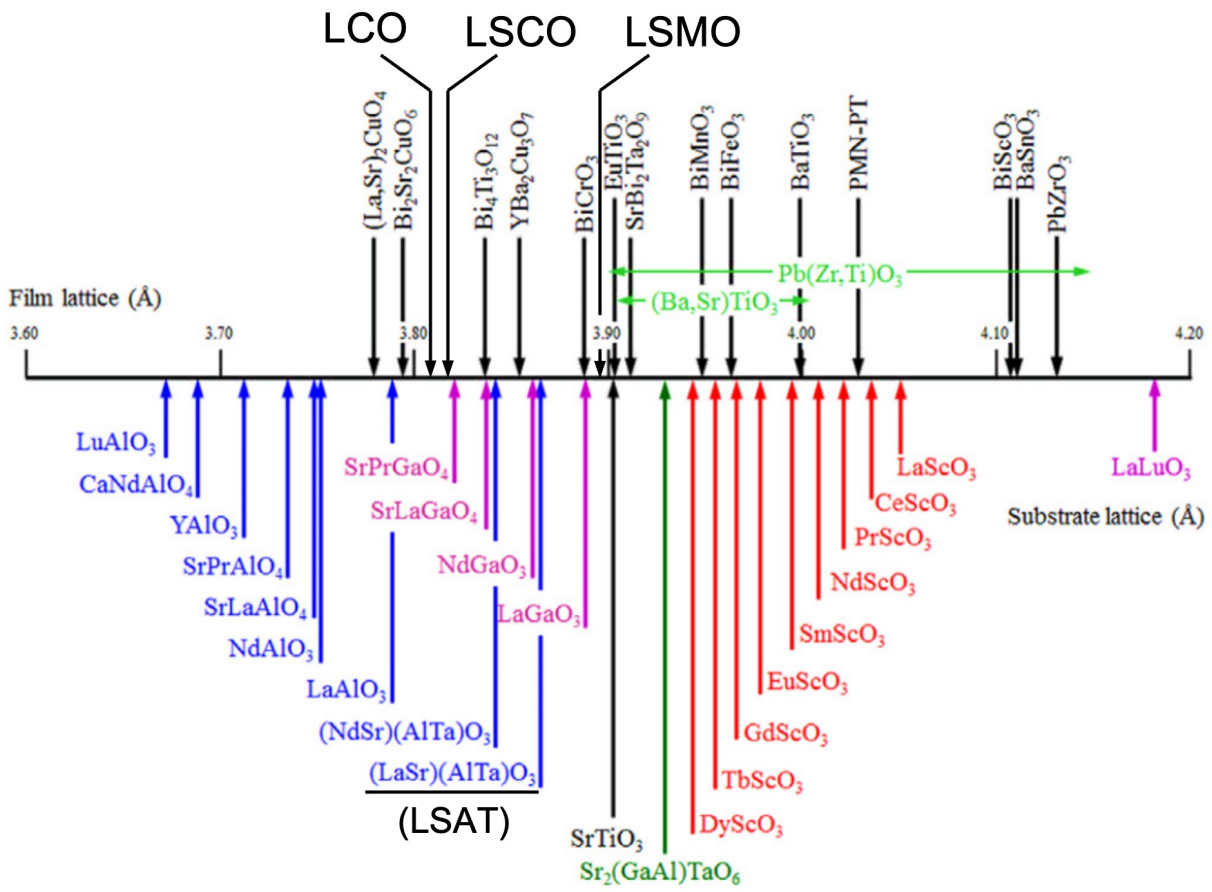

Figure 4.1: Perovskite and perovskite-related substrates plotted with their associated pseudocubic lattice parameters. The number of substrates to choose from could facilitate a study of the effect of epitaxial strain on topotactic phase transformations (adapted from Ref. [85]).

The dopant content in LSMO and LSCO could also provide an experimental variable for future work. By systematically changing the A-site doping element and concentration in the perovskite, the valence and crystal lattice distortions will change and thus change the condition to cause a topotactic phase transformation or possibly what stable structures can be formed.

Density functional theory is a well-developed and complementary technique that has been

used to support the observations and model the compositional and electronic structure of perovskite thin films [26, 59] and could be used in future studies to gain a more complete understanding of the kinetics and changes that occur in topotactic phase transformations. Machine learning is another computational tool that has been gaining momentum in materials science [86], [87] and has been used to aid in the discovery of new and stable perovskites with a variety of functional properties such as high oxygen or proton conductivity for the discovery of new fuel cell materials [88]. By analyzing large datasets, machine learning can enable researchers to reduce the parameter space of experimentation by identifying patterns and correlations between perovskite composition and material properties to predict and inform suitable combinations for experimentation. Further development of machine learning algorithms could be useful in predicting other structural phases accessible via topotaxy for a given composition and condition and their corresponding functional properties such as magnetic phases, transition temperatures, and high-T_c superconductivity.

The topotactic phase transformations observed in this thesis have given insight into the deeper mechanics responsible for the compositional and structural evolutions that take place under different annealing conditions. The results highlight the relevance of these materials for different applications and devices, but it also calls attention to the necessity for further studies to be conducted in order gain a better understanding of all of the factors that contribute to topotaxy in perovskite oxides. This thesis adds to a growing body of knowledge of topotactic phase transformations and can inform new avenues of research in this developing field for researching new and improved perovskite materials.

Bibliography

[1] Noman Bashir et al. *Sustainable Computing – Without the Hot Air*. 2022. DOI: 10.48550/ARXIV.2207.00081. URL: https://arxiv.org/abs/2207.00081.

[2] A. Mehonic and A. J. Kenyon. "Brain-inspired computing needs a master plan." In: *Nature* 604.7905 (Apr. 2022), pp. 255–260. DOI: 10.1038/s41586-021-04362-w. URL: https://doi.org/10.1038/s41586-021-04362-w.

[3] Xingqi Zou et al. "Breaking the von neumann bottleneck: Architecture-level processing-in-memory technology." In: *Science China Information Sciences* 64.6 (2021). DOI: 10.1007/s11432-020-3227-1.

[4] Steve Furber. "Large-scale neuromorphic computing systems." In: *Journal of Neural Engineering* 13.5 (Aug. 2016), p. 051001. DOI: 10.1088/1741-2560/13/5/051001. URL: https://doi.org/10.1088/1741-2560/13/5/051001.

[5] Guiming Cao et al. "2D Material Based Synaptic Devices for Neuromorphic Computing." In: *Advanced Functional Materials* 31.4 (2021), p. 2005443. DOI: https://doi.org/10.1002/adfm.202005443. eprint: https://onlinelibrary.wiley.com/doi/pdf/10.1002/adfm.202005443. URL: https://onlinelibrary.wiley.com/doi/abs/10.1002/adfm.202005443.

[6] I-Ting Chiu et al. "Cation and anion topotactic transformations in cobaltite thin films leading to Ruddlesden-Popper phases." In: *Phys. Rev. Materials* 5 (6 June 2021),

p. 064416. DOI: 10.1103/PhysRevMaterials.5.064416. URL: https://link.aps.org/doi/10.1103/PhysRevMaterials.5.064416.

[7] Andreja Žužić, Antonia Ressler, and Jelena Macan. "Perovskite oxides as active materials in novel alternatives to well-known technologies: A review." In: *Ceramics International* 48.19, Part A (2022), pp. 27240–27261. ISSN: 0272-8842. DOI: https://doi.org/10.1016/j.ceramint.2022.06.152. URL: https://www.sciencedirect.com/science/article/pii/S0272884222021551.

[8] F.K. Lotgering. "Topotactical reactions with ferrimagnetic oxides having hexagonal crystal structures—I." In: *Journal of Inorganic and Nuclear Chemistry* 9.2 (1959), pp. 113–123. ISSN: 0022-1902. DOI: https://doi.org/10.1016/0022-1902(59)80070-1. URL: https://www.sciencedirect.com/science/article/pii/0022190259800701.

[9] Alessandro R. Mazza et al. "Reversible Hydrogen-Induced Phase Transformations in La0.7Sr0.3MnO3 Thin Films Characterized by In Situ Neutron Reflectometry." In: *ACS Applied Materials & Interfaces* 14.8 (2022). PMID: 35170955, pp. 10898–10906. DOI: 10.1021/acsami.1c20590. URL: https://doi.org/10.1021/acsami.1c20590.

[10] Sourav Chowdhury, Ram J. Choudhary, and Deodatta M. Phase. "Time Evolution of the Structural, Electronic, and Magnetic Phases in Relaxed SrCoO3 Thin Films." In: *ACS Applied Electronic Materials* 3.11 (2021), pp. 5095–5101. DOI: 10.1021/acsaelm.1c00831. URL: https://doi.org/10.1021/acsaelm.1c00831.

[11] Peyton D. Murray et al. "Interfacial-Redox-Induced Tuning of Superconductivity in YBa2Cu3O7-d." In: *ACS Applied Materials & Interfaces* 12.4 (2020). PMID: 31880904, pp. 4741–4748. DOI: 10.1021/acsami.9b18820. URL: https://doi.org/10.1021/acsami.9b18820.

[12] A. J. Grutter et al. "Reversible control of magnetism in $La_0 \cdot 67\,Sr_0 \cdot 33\,MnO_3$ through chemically-induced oxygen migration." In: *Applied Physics Letters* 108.8 (Feb. 2016), p. 082405. DOI: 10.1063/1.4942645. URL: https://doi.org/10.1063/1.4942645.

[13] Geoffery Rippy et al. "X-ray nanodiffraction studies of ionically controlled nanoscale phase separation in cobaltites." In: *Phys. Rev. Materials* 3 (8 Aug. 2019), p. 082001. DOI: 10.1103/PhysRevMaterials.3.082001. URL: https://link.aps.org/doi/10.1103/PhysRevMaterials.3.082001.

[14] Dustin A. Gilbert et al. "Ionic tuning of cobaltites at the nanoscale." In: *Phys. Rev. Materials* 2 (10 Oct. 2018), p. 104402. DOI: 10.1103/PhysRevMaterials.2.104402. URL: https://link.aps.org/doi/10.1103/PhysRevMaterials.2.104402.

[15] Yaolong Xing et al. "Atomic-scale operando observation of oxygen diffusion during topotactic phase transition of a perovskite oxide." In: *Matter* 5.9 (Sept. 2022), pp. 3009–3022. DOI: 10.1016/j.matt.2022.06.013. URL: https://doi.org/10.1016/j.matt.2022.06.013.

[16] Lei Cao et al. "Reversible Control of Physical Properties via an Oxygen-Vacancy-Driven Topotactic Transition in Epitaxial La0.7Sr0.3MnO3d Thin Films." In: *Advanced Materials* 31.7 (2019), p. 1806183. DOI: https://doi.org/10.1002/adma.201806183. eprint: https://onlinelibrary.wiley.com/doi/pdf/10.1002/adma.201806183. URL: https://onlinelibrary.wiley.com/doi/abs/10.1002/adma.201806183.

[17] Hyeon Han et al. "Control of Oxygen Vacancy Ordering in Brownmillerite Thin Films via Ionic Liquid Gating." In: *ACS Nano* 16.4 (Apr. 2022), pp. 6206–6214. DOI: 10.1021/acsnano.2c00012. URL: https://doi.org/10.1021/acsnano.2c00012.

[18] Oliver Tschauner et al. "Discovery of bridgmanite, the most abundant mineral in Earth, in a shocked meteorite." In: *Science* 346.6213 (2014), pp. 1100–1102.

[19] Darrell G Schlom et al. "A thin film approach to engineering functionality into oxides." In: *Journal of the American Ceramic Society* 91.8 (2008), pp. 2429–2454.

[20] V. M. Goldschmidt. "Die Gesetze der Krystallochemie." In: *Die Naturwissenschaften* 14.21 (May 1926), pp. 477–485. DOI: 10.1007/bf01507527. URL: https://doi.org/10.1007/bf01507527.

[21] Gibin George, Sivasankara Rao Ede, and Zhiping Luo. *Fundamentals of perovskite oxides*. London, England: CRC Press, Oct. 2020.

[22] Marina R Filip and Feliciano Giustino. "The geometric blueprint of perovskites." In: *Proceedings of the National Academy of Sciences* 115.21 (2018), pp. 5397–5402.

[23] Steven C Tidrow. "Mapping comparison of Goldschmidt's tolerance factor with Perovskite structural conditions." In: *Ferroelectrics* 470.1 (2014), pp. 13–27.

[24] Shenli Zhang and Giulia Galli. "Understanding the metal-to-insulator transition in La1-xSrxCoO3-d and its applications for neuromorphic computing." In: *npj Computational Materials* 6.1 (Nov. 2020). DOI: 10.1038/s41524-020-00437-w. URL: https://doi.org/10.1038/s41524-020-00437-w.

[25] Jin Suntivich et al. "Estimating Hybridization of Transition Metal and Oxygen States in Perovskites from O K-edge X-ray Absorption Spectroscopy." In: *The Journal of Physical Chemistry C* 118.4 (Jan. 2014), pp. 1856–1863. DOI: 10.1021/jp410644j. URL: https://doi.org/10.1021/jp410644j.

[26] Lei Cao et al. "Migration Kinetics of Surface Ions in Oxygen-Deficient Perovskite During Topotactic Transitions." In: *Small* 17.51 (Nov. 2021), p. 2104356. DOI: 10.1002/smll.202104356. URL: https://doi.org/10.1002/smll.202104356.

[27] Shenli Zhang et al. "Determining the Oxygen Stoichiometry of Cobaltite Thin Films." In: *Chemistry of Materials* 34.5 (Feb. 2022), pp. 2076–2084. DOI: 10.1021/acs.chemmater.1c03338. URL: https://doi.org/10.1021/acs.chemmater.1c03338.

[28] Federica Frati, Myrtille O. J. Y. Hunault, and Frank M. F. de Groot. "Oxygen K-edge X-ray Absorption Spectra." In: *Chemical Reviews* 120.9 (2020). PMID: 32275144, pp. 4056–4110. DOI: 10.1021/acs.chemrev.9b00439. URL: https://doi.org/10.1021/acs.chemrev.9b00439.

[29] Mark T. Anderson, John T. Vaughey, and Kenneth R. Poeppelmeier. "Structural similarities among oxygen-deficient perovskites." In: *Chemistry of Materials* 5.2 (1993), pp. 151–165. DOI: 10.1021/cm00026a003. URL: https://doi.org/10.1021/cm00026a003.

[30] Jean-Claude Grenier et al. "Mise en evidence d'une nouvelle famille de phases de type perovskite lacunaire ordonnee de formule A3M3O8 (AMO2, 67)." In: *Materials Research Bulletin* 11.10 (1976), pp. 1219–1225.

[31] A. A. Colville and S. Geller. "The crystal structure of brownmillerite, Ca2FeAlO5." In: *Acta Crystallographica Section B* 27.12 (Dec. 1971), pp. 2311–2315. DOI: 10.1107/S056774087100579X. URL: https://doi.org/10.1107/S056774087100579X.

[32] Hyeon Han et al. "Control of Oxygen Vacancy Ordering in Brownmillerite Thin Films via Ionic Liquid Gating." In: *ACS Nano* 16.4 (Apr. 2022), pp. 6206–6214. DOI: 10.1021/acsnano.2c00012. URL: https://doi.org/10.1021/acsnano.2c00012.

[33] Ai Ikeda et al. "Direct observation of infinite NiO2 planes in LaNiO2 films." In: *Applied Physics Express* 9.6 (May 2016), p. 061101. DOI: 10.7567/apex.9.061101. URL: https://doi.org/10.7567/apex.9.061101.

[34] Zhe Li et al. "Infinite-layer/perovskite oxide heterostructure-induced high-spin states in SrCuO2/SrRuO3 bilayer films." In: *Materials Horizons* 8.12 (2021), pp. 3468–3476. DOI: 10.1039/d1mh01385h. URL: https://doi.org/10.1039/d1mh01385h.

[35] Satoru Inoue et al. "Single-crystal epitaxial thin films of SrFeO2 with FeO2 infinite layers." In: *Applied Physics Letters* 92.16 (Apr. 2008), p. 161911. DOI: 10.1063/1.2913164. URL: https://doi.org/10.1063/1.2913164.

[36] Masayoshi Kikuchi et al. "Electrical resistance of SrFeO2 at ultra high pressure." In: *Journal of Physics: Conference Series* 592 (Mar. 2015), p. 012041. DOI: 10.1088/1742-6596/592/1/012041. URL: https://doi.org/10.1088/1742-6596/592/1/012041.

[37] Shuang Chen et al. “Strain-mediated insulator-metal transition in topotactically hydro-reduced SrFeO2.” In: *Science China Physics, Mechanics Astronomy* 64.8 (June 2021). DOI: 10.1007/s11433-021-1713-4. URL: https://doi.org/10.1007/s11433-021-1713-4.

[38] S. N. Ruddlesden and P. Popper. “New compounds of the K2NiF4 type.” In: *Acta Crystallographica* 10.8 (Aug. 1957), pp. 538–539. DOI: 10.1107/s0365110x57001929. URL: https://doi.org/10.1107/s0365110x57001929.

[39] S. N. Ruddlesden and P. Popper. “The compound Sr3Ti2O7 and its structure.” In: *Acta Crystallographica* 11.1 (Jan. 1958), pp. 54–55. DOI: 10.1107/s0365110x58000128. URL: https://doi.org/10.1107/s0365110x58000128.

[40] Ainara Aguadero, José Antonio Alonso, and Loreto Daza. In: *Zeitschrift für Naturforschung B* 63.6 (2008), pp. 615–622. DOI: doi:10.1515/znb-2008-0604. URL: https://doi.org/10.1515/znb-2008-0604.

[41] Jinkwon Kim et al. “Superconducting Sr2RuO4 Thin Films without Out-of-Phase Boundaries by Higher-Order Ruddlesden-Popper Intergrowth.” In: *Nano Letters* 21.10 (May 2021), pp. 4185–4192. DOI: 10.1021/acs.nanolett.0c04963. URL: https://doi.org/10.1021/acs.nanolett.0c04963.

[42] Alessandro R. Mazza et al. “Searching for superconductivity in high entropy oxide Ruddlesden–Popper cuprate films.” In: *Journal of Vacuum Science Technology A* 40.1 (2022), p. 013404. DOI: 10.1116/6.0001441. URL: https://doi.org/10.1116/6.0001441.

[43] A. Kostopoulou, E. Kymakis, and E. Stratakis. “Perovskite nanostructures for photovoltaic and energy storage devices.” In: *J. Mater. Chem. A* 6 (21 2018), pp. 9765–9798. DOI: 10.1039/C8TA01964A. URL: http://dx.doi.org/10.1039/C8TA01964A.

[44] Hung-Chia Wang et al. “Perovskite Quantum Dots and Their Application in Light-Emitting Diodes.” In: *Small* 14.1 (2018), p. 1702433. DOI: https://doi.org/10.1002/smll.201702433. eprint: https://onlinelibrary.wiley.com/doi/pdf/10.1002/smll.201702433. URL: https://onlinelibrary.wiley.com/doi/abs/10.1002/smll.201702433.

[45] Di Lu et al. "Synthesis of freestanding single-crystal perovskite films and heterostructures by etching of sacrificial water-soluble layers." In: *Nature Materials* 15.12 (Sept. 2016), pp. 1255–1260. DOI: 10.1038/nmat4749. URL: https://doi.org/10.1038/nmat4749.

[46] Yue Jia et al. "Thickness dependence of exchange coupling in (111)-oriented perovskite oxide superlattices." In: *Phys. Rev. B* 93 (10 Mar. 2016), p. 104403. DOI: 10.1103/PhysRevB.93.104403. URL: https://link.aps.org/doi/10.1103/PhysRevB.93.104403.

[47] Milton Ohring. "A Review of Materials Science." In: *Materials Science of Thin Films*. Elsevier, 2002, pp. 1–56.

[48] K. Hayashi, E. Ohta, and H. Wada. "Effect of substrate-film lattice mismatch in La[sub 0.7]Ba[sub 0.3]MnO[sub 3-] thin films for transport properties." In: *Journal of Vacuum Science Technology A: Vacuum, Surfaces, and Films* 19.6 (2001), p. 2905. DOI: 10.1116/1.1414124. URL: https://doi.org/10.1116/1.1414124.

[49] Sangmoon Yoon et al. "Strain-Induced Atomic-Scale Building Blocks for Ferromagnetism in Epitaxial LaCoO3." In: *Nano Letters* 21.9 (Apr. 2021), pp. 4006–4012. DOI: 10.1021/acs.nanolett.1c00756. URL: https://doi.org/10.1021/acs.nanolett.1c00756.

[50] Angus Rockett. *The materials science of semiconductors*. en. New York, NY: Springer, Oct. 2010.

[51] T. Heeg et al. "Epitaxially stabilized growth of orthorhombic LuScO3 thin films." In: *Applied Physics Letters - APPL PHYS LETT* 90 (May 2007), pp. 2901–192901. DOI: 10.1063/1.2737136.

[52] Asadullah Awan, Hong Truong, and Robert Lancashire. *Crystal Field Theory*. 2022. URL: https://chem.libretexts.org/Bookshelves/Inorganic_Chemistry/Supplemental_Modules_and_Websites_(Inorganic_Chemistry)/Crystal_Field_Theory/Crystal_Field_Theory.

[53] Erin K. Byrne, Darrin S. Richeson, and Klaus H. Theopold. "Tetrakis(1-norbornyl)cobalt, a low spin tetrahedral complex of a first row transition metal." In: *Journal of the Chem-*

ical Society, Chemical Communications 19 (1986), p. 1491. DOI: 10.1039/c39860001491. URL: https://doi.org/10.1039/c39860001491.

[54] M. E. Pascualini et al. "A high-spin square-planar Fe complex stabilized by a trianionic pincer-type ligand and conclusive evidence for retention of geometry and spin state in solution." In: *Chemical Science* 6.1 (2015), pp. 608–612. DOI: 10.1039/c4sc02634a. URL: https://doi.org/10.1039/c4sc02634a.

[55] "Stability of polyatomic molecules in degenerate electronic states - I-Orbital degeneracy." In: *Proceedings of the Royal Society of London. Series A - Mathematical and Physical Sciences* 161.905 (July 1937), pp. 220–235. DOI: 10.1098/rspa.1937.0142. URL: https://doi.org/10.1098/rspa.1937.0142.

[56] Clarence Zener. "Interaction between the *d*-Shells in the Transition Metals. II. Ferromagnetic Compounds of Manganese with Perovskite Structure." In: *Phys. Rev.* 82 (3 May 1951), pp. 403–405. DOI: 10.1103/PhysRev.82.403. URL: https://link.aps.org/doi/10.1103/PhysRev.82.403.

[57] H.A Kramers. "L'interaction Entre les Atomes Magnétogènes dans un Cristal Paramagnétique." In: *Physica* 1.1 (1934), pp. 182–192. ISSN: 0031-8914. DOI: https://doi.org/10.1016/S0031-8914(34)90023-9. URL: https://www.sciencedirect.com/science/article/pii/S0031891434900239.

[58] J. Hemberger et al. "Structural, magnetic, and electrical properties of single-crystalline La1-xSrxMnO3, x=0.4–0.85." In: *Physical Review B* 66.9 (Sept. 2002). DOI: 10.1103/physrevb.66.094410. URL: https://doi.org/10.1103/physrevb.66.094410.

[59] I-Ting Chiu. "Growth and Characterization of Magnetic Perovskite and Perovskite-related Phases." PhD dissertation. University of California, Davis, 2021.

[60] J. Wu and C. Leighton. "Glassy ferromagnetism and magnetic phase separation in La1-xSrxCoO3." In: *Physical Review B* 67.17 (May 2003). DOI: 10.1103/physrevb.67.174408. URL: https://doi.org/10.1103/physrevb.67.174408.

[61] S. Yamaguchi, Y. Okimoto, and Y. Tokura. "Local lattice distortion during the spin-state transition in LaCoO3." In: *Physical Review B* 55.14 (Apr. 1997), R8666–R8669. DOI: 10.1103/physrevb.55.r8666. URL: https://doi.org/10.1103/physrevb.55.r8666.

[62] Rajashree Nori et al. "Conducting Oxide Electrode to Mitigate Mechanical Instability (Bubble Formation) during Operation of La1-xSrxMnO3 (LSMO) based RRAM." In: *MRS Proceedings* 1507 (2013). DOI: 10.1557/opl.2013.381. URL: https://doi.org/10.1557/opl.2013.381.

[63] Sayani Majumdar and Sebastiaan van Dijken. "Pulsed laser deposition of La1-xSrxMnO3: thin-film properties and spintronic applications." In: *Journal of Physics D: Applied Physics* 47.3 (Dec. 2013), p. 034010. DOI: 10.1088/0022-3727/47/3/034010. URL: https://doi.org/10.1088/0022-3727/47/3/034010.

[64] Robert Eason. *Pulsed laser deposition of thin films*. en. Ed. by Robert Eason. Nashville, TN: John Wiley & Sons, Nov. 2006.

[65] *Pulsed Laser Deposition System: NBM design: United States*. URL: https://www.nbmdesign.com/.

[66] Min-Han Lee et al. "Controlling Metal–Insulator Transitions in Vanadium Oxide Thin Films by Modifying Oxygen Stoichiometry." In: *ACS Applied Materials & Interfaces* 13.1 (2021). PMID: 33351594, pp. 887–896. DOI: 10.1021/acsami.0c18327. URL: https://doi.org/10.1021/acsami.0c18327.

[67] Alex Ulyanenkov. "LEPTOS: a universal software for x-ray reflectivity and diffraction." In: *SPIE Proceedings*. Ed. by Manuel Sanchez del Rio. SPIE, Oct. 2004. DOI: 10.1117/12.563302. URL: https://doi.org/10.1117/12.563302.

[68] Artur Glavic and Matts Björck. "GenX 3: the latest generation of an established tool." In: *Journal of Applied Crystallography* 55.4 (July 2022), pp. 1063–1071. DOI: 10.1107/s1600576722006653. URL: https://doi.org/10.1107/s1600576722006653.

[69] John Evans. *X-ray absorption spectroscopy for the chemical and materials sciences*. en. Nashville, TN: John Wiley & Sons, Jan. 2018.

[70] Gerrit van der Laan and Adriana I. Figueroa. "X-ray magnetic circular dichroism–A versatile tool to study magnetism." In: *Coordination Chemistry Reviews* 277-278 (Oct. 2014), pp. 95–129. DOI: 10.1016/j.ccr.2014.03.018. URL: https://doi.org/10.1016/j.ccr.2014.03.018.

[71] Maria C. Molina Higgins, Hailey Hall, and Jessika V. Rojas. "The effect of X-ray induced oxygen defects on the photocatalytic properties of titanium dioxide nanoparticles." In: *Journal of Photochemistry and Photobiology A: Chemistry* 409 (Mar. 2021), p. 113138. DOI: 10.1016/j.jphotochem.2021.113138. URL: https://doi.org/10.1016/j.jphotochem.2021.113138.

[72] V N Strocov et al. "Dimensionality of mobile electrons at x-ray-irradiated LaAlOsub3/sub/SrTiOsub3 interfaces." In: *Electronic Structure* 4.1 (Feb. 2022), p. 015003. DOI: 10.1088/2516-1075/ac4e74. URL: https://doi.org/10.1088/2516-1075/ac4e74.

[73] Yayoi Takamura et al. "Spin-Flop Coupling and Exchange Bias in Embedded Complex Oxide Micromagnets." In: *Physical Review Letters* 111.10 (Sept. 2013). DOI: 10.1103/physrevlett.111.107201. URL: https://doi.org/10.1103/physrevlett.111.107201.

[74] Magnus Moreau, Sverre M. Selbach, and Thomas Tybell. "Spatially Confined Spin Polarization and magnetic sublattice control in (La, Sr)MnO3-d Thin Films by Oxygen Vacancy Ordering." In: *Scientific Reports* 7.1 (June 2017). DOI: 10.1038/s41598-017-04103-y. URL: https://doi.org/10.1038/s41598-017-04103-y.

[75] Michael S. Lee et al. "Modification of magnetocrystalline anisotropy via ion-implantation." In: *AIP Advances* 10.4 (Apr. 2020), p. 045306. DOI: 10.1063/1.5134867. URL: https://doi.org/10.1063/1.5134867.

[76] Subhayan Roychoudhury et al. "Deciphering the Oxygen Absorption Pre-edge: A Caveat on its Application for Probing Oxygen Redox Reactions in Batteries." In:

ENERGY ENVIRONMENTAL MATERIALS 4.2 (Dec. 2020), pp. 246–254. DOI: 10.1002/eem2.12119. URL: https://doi.org/10.1002/eem2.12119.

[77] Federica Frati, Myrtille O. J. Y. Hunault, and Frank M. F. de Groot. "Oxygen K-edge X-ray Absorption Spectra." In: *Chemical Reviews* 120.9 (Apr. 2020), pp. 4056–4110. DOI: 10.1021/acs.chemrev.9b00439. URL: https://doi.org/10.1021/acs.chemrev.9b00439.

[78] Vivek K. Malik et al. "Magnetic correlation between La0.7Sr0.3MnO3 and La0.7Sr0.3CoO3 layers in artificial superlattices." In: *Journal of Applied Physics* 113.15 (Apr. 2013). ISSN: 1089-7550. DOI: 10.1063/1.4802670. URL: http://dx.doi.org/10.1063/1.4802670.

[79] M. Merz et al. "X-ray absorption and magnetic circular dichroism of LaCoO3, La0.7Ce0.3CoO3 and La0.7Sr0.3CoO3 films: Evidence for cobalt-valence-dependent magnetism." In: *Physical Review B* 82.17 (Nov. 2010). DOI: 10.1103/physrevb.82.174416. URL: https://doi.org/10.1103/physrevb.82.174416.

[80] Qichang An et al. "Realization of Monophased LaCoO Films with Ordered Oxygen Vacancies." In: *physica status solidi (a)* 217.1 (Dec. 2019), p. 1900848. DOI: 10.1002/pssa.201900848. URL: https://doi.org/10.1002/pssa.201900848.

[81] K.J. Dempsey et al. "Tuning the coercive field of Ni and CuNi thin films with the embedding of Co nanoparticles: An element-specific study." In: *Journal of Magnetism and Magnetic Materials* 322.23 (Dec. 2010), pp. 3817–3821. ISSN: 0304-8853. DOI: 10.1016/j.jmmm.2010.08.019. URL: http://dx.doi.org/10.1016/j.jmmm.2010.08.019.

[82] Wei-Chun Lin et al. "In situ XPS investigation of the X-ray-triggered decomposition of perovskites in ultrahigh vacuum condition." In: *npj Materials Degradation* 5.1 (Apr. 2021). DOI: 10.1038/s41529-021-00162-9. URL: https://doi.org/10.1038/s41529-021-00162-9.

[83] T. Labii et al. "Dilatometric study of CaFeO2.5 single crystal." In: *Journal of Thermal Analysis and Calorimetry* 112.2 (Sept. 2012), pp. 865–870. DOI: 10.1007/s10973-012-2690-y. URL: https://doi.org/10.1007/s10973-012-2690-y.

[84] Kejun Hu et al. "Atomic-scale observation of strain-dependent reversible topotactic transition in La0.7Sr0.3MnOx films under an ultra-high vacuum environment." In: *Materials Today Physics* 29 (Dec. 2022), p. 100922. DOI: 10.1016/j.mtphys.2022.100922. URL: https://doi.org/10.1016/j.mtphys.2022.100922.

[85] Reinhard Uecker et al. "Large-lattice-parameter perovskite single-crystal substrates." In: *Journal of Crystal Growth* 457 (Jan. 2017), pp. 137–142. DOI: 10.1016/j.jcrysgro.2016.03.014. URL: https://doi.org/10.1016/j.jcrysgro.2016.03.014.

[86] Mark Peplow. "Google AI and robots join forces to build new materials." In: *Nature* (Nov. 2023). ISSN: 1476-4687. DOI: 10.1038/d41586-023-03745-5. URL: http://dx.doi.org/10.1038/d41586-023-03745-5.

[87] Nathan J. Szymanski et al. "An autonomous laboratory for the accelerated synthesis of novel materials." In: *Nature* (Nov. 2023). ISSN: 1476-4687. DOI: 10.1038/s41586-023-06734-w. URL: http://dx.doi.org/10.1038/s41586-023-06734-w.

[88] Pikee Priya and N. R. Aluru. "Accelerated design and discovery of perovskites with high conductivity for energy applications through machine learning." In: *npj Computational Materials* 7.1 (June 2021). DOI: 10.1038/s41524-021-00551-3. URL: https://doi.org/10.1038/s41524-021-00551-3.